

1  
2  
3  
4  
5  
6  
7  
8  
9  
10  
11  
12  
13  
14  
15  
16  
17  
18  
19  
20  
21  
22  
23  
24  
25  
26  
27  
28  
29  
30  
31  
32  
33  
34  
  
1

[Our answers to reviewers are written in blue](#)

**Anonymous Referee #3**

Received and published: 30 December 2018

This paper presents a new estimate of the shortwave direct radiative effect attributable to aerosols above clouds. The paper builds on the previous literature by advancing a technique that applies globally and utilizes the depolarization ratio method applied to global CALIOP observations. Use of the depolarization ratio method improves upon a widespread underestimate of aerosol optical thicknesses in the standard CALIOP retrieval products, but seems to struggle to capture cases of dust over clouds. The paper does a nice job of summarizing the studies that have come before, the variety of methods that have been applied to this problem, and the problems that hinder the precise quantification of the global radiative effect. The paper also does a nice job of placing their quantitative results in the context of other estimates. I have only some minor comments. After addressing these, the paper should be suitable for publication in ACP.

[We thank the referee for their kind remarks and their very thorough reading of our lengthy manuscript.](#)

1.a. *AR#3*: The analysis is restricted to clouds that are determined to be opaque, but the method by which opaque clouds are distinguished from clouds that are not opaque is not clear. In the appendix it is noted that the “CALIOP opacity flag” is used. There should be a brief mention in the body of the paper of the physical basis for the “opacity flag”.

[Our answer](#): We now include this short description of the physical basis for the CALIOP opacity flag at the beginning of section 2.1:

*“Because the CALIOP backscatter signal is totally attenuated below the lowest “feature” detected within any profile [Vaughan et al., 2009], this lowest feature is defined as being opaque. Approximately 69% of the time, the opaque feature detected in a profile is the Earth’s surface [Guzman et al., 2017]. In the remainder of the cases, the opaque feature is either a water cloud, an ice cloud, or, very rarely, an aerosol layer.” (...)* “(1) only one cloud can be detected within a 5 km (15 shot) along-track average (...) and (2) this one cloud must be opaque (i.e., lowest feature detected in a column, and not subsequently classified as a surface return).”

1.b. *AR#3*: Are there particular regimes where low clouds are prevalent but transparent?

[Our answer](#): Yes. As shown by Figure 5 in Leahy et al. [2012], while transparent low clouds occur globally, they are much more prevalent in the southern oceans and, to a lesser extent, in the northern Pacific.

35 1.c. AR#3: There is a vague reference to “clouds such as the ones reported in Leahy et al. (2012)”. A  
36 more specific description would be better.

37 *Our answer:* Our revised description of the Leahy reference now reads as follows in section 2.1:

38 *“However, because the DR retrieval technique requires backscatter measurements from opaque water*  
39 *clouds [Hu et al., 2007b], it cannot be used to retrieve AOD from aerosols lying above the low,*  
40 *transparent water clouds that are frequently observed over remote oceans, especially in the southern*  
41 *hemisphere (e.g., Leahy et al. [2012]; Mace and Protat [2018]; O et al. [2018]).”*

42 2. AR#3: Figure 1 indicates that the Southern Ocean is the most prominent place on the globe for  
43 uniform single layer clouds, but panel b suggests that they are not suitable for the depolarization ratio  
44 method. Perhaps it is not of great importance if most of this region has little appreciable aerosol above  
45 the cloud layer. Nevertheless, I was left wondering why. Is it a quality of the clouds? Or merely a lack  
46 of aerosol optical thickness?

47 *Our answer:* Please see our response to the previous comment. The issue is the quality of the clouds;  
48 i.e., the clouds in the Southern Ocean are often transparent, and transparent clouds are not suitable for  
49 analysis using the DR method. We hope that the additional references (i.e., Mace and Protat [2018]; O  
50 et al. [2018]) will provide some further insights into the nature and causes of these geometrically and  
51 optically thin clouds.

52 3. AR#3: Panel d of figure 1 shows a substantial underestimate of cases of aerosol above cloud  
53 compared to a similar statistic based on the standard CALIOP aerosol optical thickness product for  
54 continents and for oceanic regions dominated by dust plumes. This is discussed in a couple of places in  
55 the manuscript, but nevertheless I remained confused as to the cause. The only indication in the body of  
56 the paper on line 316 where it says “. . . filtering out of ‘unobstructed’ but potentially aerosol-  
57 contaminated OWCs.” The paper does not make clear what “obstructed” or “unobstructed” means in  
58 this context or why such clouds would be filtered. This sentence is in dire need of some plain English.

59 *Our answer:* In response to the referee’s remark, we made numerous changes to the text in this  
60 paragraph. In particular, we replaced this sentence: “One reason for the lack of AAC cases offshore  
61 from the west coast of Africa in our dataset is the filtering out of “unobstructed” but potentially  
62 aerosol-contaminated OWCs (see section B3 in the appendix for more details)” with this more in-depth  
63 explanation: “The lack of AAC cases offshore from the southwest coast of Africa in the DR method  
64 dataset is the result of our conservative data filtering strategy. Because the IABs of aerosol-  
65 contaminated OWCs can differ significantly from those measured in pristine, aerosol-free conditions,  
66 OWCs suspected of being aerosol-contaminated (which are ubiquitous in this part of the world and very  
67 common over continents) are specifically excluded from our DR method analyses (see appendix section  
68 B3 for more details).”

69 4. AR#3: Another place where the description is so technical as to hide the point is in the discussion of  
70 the extinction-to-backscatter ratios in sections 3.2.2 and 3.2.3. My sense is that there is an important  
71 point in these sections and that differences in the probability distributions in figure 6 must be

72 significant. But it was not clear what that point is or what the significance to the main result of the paper  
73 is.

74 *Our answer:* This comment was particularly helpful to us. Thank you. The article under review is the  
75 result of many years of analysis. There was a time when this work was separated in two parts  
76 describing, on the one hand, our AAC aerosol optical depths (AOD) paired with CALIOP AAC  
77 extinction-to-backscatter values (S\_AAC) and, on the other, the Direct Aerosol Radiative Effects above  
78 clouds (DARE\_cloudy). The S\_AAC values were there to illustrate the different aerosol types present  
79 above clouds.

80  
81 Our ultimate goal in this paper now being the calculation of global DARE\_cloudy, and knowing that  
82 S\_AAC values are not needed in our calculation of DARE\_cloudy, these S\_AAC are more of a  
83 distraction to the reader. As a consequence, we have deleted section 3.2.2, 3.2.3, appendix B4 and all of  
84 its dependencies. We plan to publish these results separately.

85

86 5. AR#3: Minor point: In the sentence beginning in line 308 the authors state “. . .negative (positive)  
87 values in blue (red) show the number of AAC cases that are missed (gained). . .” Way back in 2010  
88 Prof. Robock pleaded with us to end this misuse of parentheses [Robock, A. (2010), Parentheses are  
89 (are not) for references and clarification (saving space), Eos Trans. AGU, 91(45), 419–419,  
90 doi:10.1029/2010EO450004]. My understanding is that one of the publishers in our field has  
91 specifically written it out of their style guide. I read pretty widely and the only genre of writing where I  
92 have experienced this application of parentheses is in the atmospheric sciences journals. I hope the  
93 authors will consider rewriting this sentence.

94 *Our answer:* We have re-written the sentence. Many thanks for the Robock reference.

95

96 **Referee #2 Dr Abhay Devasthale**

97 I will keep the review short and to the point. If not the lengthiest, it is one of the lengthiest manuscripts  
98 I have reviewed so far. So it took me some time to go through it few times and come to the grips of how  
99 the DARE\_OWCs are actually computed. But once I started reading it carefully, it was easier to follow  
00 and understand. I appreciate the hidden efforts behind the work needed to bring onboard information  
01 from the suit of sensors. I also appreciate the way authors contrast and compare their results with the  
02 previous studies. Table 5 is a good idea and could be useful for evaluating models. As far as the  
03 methodology and results are concerned, I do not see anything that should raise a red flag.

04

05 *Our answer:* We thank Dr Devasthale for his kind words and thoughtful comments. We are pleased to  
06 announce that the manuscript will be shorter after deleting section 3.2.2, 3.2.3, appendix B4 and all of  
07 its dependencies (following one of reviewer #3’s comments).

08

09 I do however have one key concern as mentioned below. CALIOP offers two distinct advantages over  
10 passive sensors, namely its superiority in detecting aerosol layers and their precise altitudes. While the  
11 authors go to such a great length and detail to be as realistic and up-to-date in taking into account  
12 aerosol and cloud layers (and their properties) as possible, if I am not mistaken, the altitude of these  
13 layers is assumed to be constant globally. And I can't help but wonder how this is going to affect their  
14 estimates, given the diversity in the verticality of aerosol and clouds in the AAC scenarios and its  
15 impact on DARE\_OWCs. It is not even clear to me if only tropospheric aerosols were selected (maybe I  
16 missed reading it somewhere). I understand that the authors comment on this in Section 4.5, but I would  
17 really appreciate if the authors do a quick sensitivity study (e.g. maybe over one of the hot-spots) by  
18 incorporating realistic vertical distribution of aerosol and cloud layers, to be able to get an idea of the  
19 uncertainty.

20  
21 We particularly appreciate Dr Devasthale's comment on the impact of assumed aerosol and cloud  
22 vertical distribution on DARE\_OWC. His suggestion has led us to substantially re-write and improve  
23 section 4.5. "assuming fixed aerosol and cloud vertical layers" to add more discussion of previous work  
24 on the subject. We are very grateful as we think this improves this section (and therefore our paper). As  
25 written in this section, multiple peer reviewed papers have emphasized the minimal impact of the height  
26 of the aerosols above clouds in the calculation of DARE\_OWCs, as compared to the effect of changes  
27 in other parameters such as the AOD, SSA, or cloud albedo. For this reason we have not included any  
28 further sensitivity analysis varying the aerosol and cloud height in our calculations in the present work.

29  
30 This is how section 4.5 reads now:

31  
32 *"Finally, Long Wave (LW) radiative forcing is particularly dependent on the vertical distribution of*  
33 *aerosols, especially for light absorbing aerosols [Chin et al., 2009]. This is because the energy these*  
34 *aerosols reradiate depends on the temperature, and hence their altitude. For example, Penner et al.*  
35 *[2003] emphasize the importance of soot and smoke aerosol injection height in LW TOA DARE<sub>all-sky</sub>*  
36 *(see Eq. 1) simulations (higher injection heights tend to enhance the negative LW radiative forcing).*  
37 *Quijano et al. [2000], Chung et al. [2005] and Chin et al. [2009] demonstrate the importance of an*  
38 *aerosol height, in relation to a cloud height (i.e., the aerosols located above, within or below the*  
39 *clouds) in an accurate estimation of SW TOA DARE<sub>all-sky</sub>. Chung et al. [2005], for example, show that*  
40 *varying the relative vertical distribution of aerosols and clouds leads to a range of global*  
41 *anthropogenic SW TOA DARE<sub>all-sky</sub> from -0.1 to -0.6 Wm<sup>-2</sup> (using a combination of MODIS satellite,*  
42 *AERONET ground-based observations and CTM simulations, see their Table 2).*  
43 *However, here, we concentrate on cases of aerosol layers overlying clouds in order to compute SW*  
44 *TOA DARE<sub>cloudy</sub>. Aerosol and cloud layer heights are assumed constant over the globe in our study (see*  
45 *section 2.2). Future studies should incorporate mean gridded (i.e., 4°x5° in this study)-seasonal*  
46 *CALIOP Level 2 aerosol and cloud vertical profiles into the calculation of DARE<sub>owc</sub>.*  
47 *However, constraining clouds between 2 and 3km in our study does not seem unreasonable as our AAC*  
48 *AOD calculations using the DR method can only be applied to aerosols overlying specific low opaque*  
49 *water clouds with, among other criteria, an altitude below 3km (see Table B2). On the other hand,*

50 *constraining aerosols between 3 and 4km in our study is not realistic over many parts of the globe (e.g.,*  
51 *see Fig. 7 of Devasthale et al. [2011]). For example, over the region of South East Atlantic during the*  
52 *ORACLES campaign, the HSRL team observed an aerosol layer located in average between 2 and 5km,*  
53 *and overlying a cloud at an average altitude of 1.2km.*  
54 *According to Zarzycki et al. [2010], the underlying cloud properties are orders of magnitude more*  
55 *crucial to the computation of  $DARE_{cloudy}$  than the location of the aerosol layer relative to the cloud, as*  
56 *long as the aerosol is above the cloud. In other words, the forcing does not seem to depend on the*  
57 *height of the aerosols above clouds as much as other parameters such as the AOD, SSA or cloud*  
58 *albedo. Zarzycki et al. [2010] investigated this assumption and found that over low and middle clouds,*  
59 *forcing changed by ~1-3% through the heights where the Black Carbon burden was the largest. These*  
60 *small changes in forcing are likely products of a change in atmospheric transmission above the aerosol*  
61 *layer [Haywood and Ramaswamy, 1998] (e.g., a change in the aerosol height linked to a change in the*  
62 *integrated column water vapor above the aerosol layer and this, in turn, would alter the incident solar*  
63 *radiation)."*  
64

65  
66 **Estimations of Global Shortwave Direct Aerosol Radiative Effects Above Opaque Water Clouds**  
67 **Using a Combination of A-Train Satellite Sensors**

68 [Meloë S. Kacenenbogen](#)<sup>1</sup>  
69 [Mark A. Vaughan](#)<sup>3</sup>  
70 [Jens Redemann](#)<sup>4</sup>  
71 [Stuart A. Young](#)<sup>5</sup>  
72 [Zhaoyan Liu](#)<sup>3,5</sup>  
73 [Yongxiang Hu](#)<sup>3</sup>  
74 [Ali H. Omar](#)<sup>3</sup>  
75 [Samuel LeBlanc](#)<sup>2</sup>  
76 [Yohei Shinozuka](#)<sup>2</sup>  
77 [John Livingston](#)<sup>2</sup>  
78 [Qin Zhang](#)<sup>2</sup>  
79 [Kathleen A. Powell](#)<sup>3</sup>

80  
81 <sup>1</sup>[NASA Ames Research Center, Moffett Field, CA, USA](#)  
82 <sup>2</sup>[Bay Area Environmental Research Institute, Sonoma, CA, USA](#)  
83 <sup>3</sup>[NASA Langley Research Center, Hampton, VA, USA](#)  
84 <sup>4</sup>[University of Oklahoma, 120 David L. Boren Blvd., Suite 5900, Norman, OK](#)  
85 <sup>5</sup>[Science Systems and Applications, Inc., Hampton, Virginia, USA](#)

86  
87 *Correspondence to:* [Meloë S. Kacenenbogen \(meloë.s.kacenenbogen@nasa.gov\)](mailto:meloë.s.kacenenbogen@nasa.gov)  
88

**Deleted:** [Meloë S. Kacenenbogen](#)<sup>1</sup>  
[Mark A. Vaughan](#)<sup>2</sup>  
[Jens Redemann](#)<sup>4</sup>  
[Stuart A. Young](#)<sup>5</sup>  
[Zhaoyan Liu](#)<sup>2,4</sup>  
[Yongxiang Hu](#)<sup>2</sup>  
[Ali H. Omar](#)<sup>2</sup>  
[Samuel LeBlanc](#)<sup>1,4</sup>  
[Yohei Shinozuka](#)<sup>1,4</sup>  
[John Livingston](#)<sup>1,4</sup>  
[Qin Zhang](#)<sup>1,4</sup>  
[Kathleen A. Powell](#)<sup>2</sup>  
<sup>1</sup>[Bay Area Environmental Research Institute, Sonoma, CA, USA](#)  
<sup>2</sup>[NASA Langley Research Center, Hampton, VA, USA](#)  
<sup>3</sup>[University of Oklahoma, 120 David L. Boren Blvd., Suite 5900, Norman, OK](#)  
<sup>4</sup>[Science Systems and Applications, Inc., Hampton, Virginia, USA](#)

07 **Abstract**

08 All-sky Direct Aerosol Radiative Effects (DARE) play a significant yet still uncertain role in climate.  
09 This is partly due to poorly quantified radiative properties of Aerosol Above Clouds (AAC). We  
10 compute global estimates of short-wave top-of-atmosphere DARE over Opaque Water Clouds (OWC),  
11  $DARE_{OWC}$ , using observation-based aerosol and cloud radiative properties from a combination of A-  
12 Train satellite sensors and a radiative transfer model. There are three major differences between our  
13  $DARE_{OWC}$  calculations and previous studies: (1) we use the Depolarization Ratio method (DR) on  
14 CALIOP (Cloud Aerosol Lidar with Orthogonal Polarization) Level 1 measurements to compute the  
15 AAC frequencies of occurrence and the AAC Aerosol Optical Depths (AOD), thus introducing fewer  
16 uncertainties compared to using the CALIOP standard product; (2) we apply our calculations globally,  
17 instead of focusing exclusively on regional AAC “hotspots” such as the southeast Atlantic; and (3)  
18 instead of the traditional look-up table approach, we use a combination of satellite-based sensors to  
19 obtain AAC intensive radiative properties. Our results agree with previous findings on the dominant  
20 locations of AAC (South and North East Pacific, Tropical and South East Atlantic, northern Indian  
21 Ocean and North West Pacific), the season of maximum occurrence, ~~and aerosol optical depths (a~~  
22 majority in the 0.01-0.02 range and that can exceed 0.2 at 532 nm) ~~over the globe. We find positive~~  
23 averages of global seasonal  $DARE_{OWC}$  between 0.13 and 0.26  $W \cdot m^{-2}$  (i.e., a warming effect on climate).  
24 Regional seasonal  $DARE_{OWC}$  values range from  $-0.06 W \cdot m^{-2}$  in the Indian Ocean, offshore from  
25 western Australia (in March-April-May) to  $2.87 W \cdot m^{-2}$  in the South East Atlantic (in September-  
26 October-November). High positive values are usually paired with high aerosol optical depths ( $>0.1$ ) and

Deleted: ,

Deleted: and aerosol extinction-to-backscatter ratios (a majority in the 40-50 sr range at 532 nm which is typical of dust aerosols)

30 low single scattering albedos ( $<0.94$ ), representative of, e.g., biomass burning aerosols. Because we use  
31 different spatial domains, temporal periods, satellite sensors, detection methods, and/or associated  
32 uncertainties, the  $DARE_{OWC}$  estimates in this study are not directly comparable to previous peer-  
33 reviewed results. Despite these differences, we emphasize that the  $DARE_{OWC}$  estimates derived in this  
34 study are generally higher than previously reported. The primary reasons for our higher estimates are (i)  
35 the possible underestimate of the number of dust-dominated AAC cases in our study; (ii) our use of  
36 Level 1 CALIOP products (instead of CALIOP Level 2 products in previous studies) for the detection  
37 and quantification of AAC aerosol optical depths, which leads to larger estimates of AOD above OWC;  
38 and (iii) our use of gridded  $4^\circ \times 5^\circ$  seasonal means of aerosol and cloud properties in our  $DARE_{OWC}$   
39 calculations instead of simultaneously derived aerosol and cloud properties from a combination of A-  
40 Train satellite sensors. Each of these areas is explored in depth with detailed discussions that explain  
41 both rationale for our specific approach and the subsequent ramifications for our DARE calculations.

42

**ACRONYMS**

AAC	Aerosol-Above-Clouds
AAOD	Absorption Aerosol Optical Depth
AOD	Aerosol Optical Depth
$\tau_{AAC}^{DR}$	Aerosol Optical Depth above clouds using the DR method
AeroCom	Aerosol Comparisons between Observations and Models
AERONET	Aerosol RObotic NETwork
AMSR-E	Advanced Microwave Scanning Radiometer - Earth Observing System
ARCTAS	Arctic Research of the Composition of the Troposphere from Aircraft and Satellites
ASR	integrated Attenuated Scattering Ratio
BRDF	Bidirectional Reflectance Distribution Function
CAC	Clear Air above Cloud
CALIOP	Cloud Aerosol Lidar with Orthogonal Polarization
CALIPSO	Cloud-Aerosol Lidar and Infrared Pathfinder Satellite Observations
CERES	Clouds and the Earth's Radiant Energy System
CF	Cloud Fraction
CloudSat	NASA Earth observation satellite
COD	Cloud Optical Depth

CR	Color Ratio technique
DARE <sub>all-sky</sub>	Direct Aerosol Radiative Effect in all-sky conditions (cloudy and non-cloudy)
DARE <sub>cloudy</sub>	Direct Aerosol Radiative Effect in cloudy conditions
DARE <sub>non-cloudy</sub>	Direct Aerosol Radiative Effect in non-cloudy conditions (clear-skies)
DARE <sub>OWC</sub>	Direct Aerosol Radiative Effect above opaque water clouds
DISORT	DIScrete ORdinate Radiative Transfer solvers
DR	Depolarization Ratio technique
$\delta^{OWC}$	layer-integrated volume depolarization ratio
$f_{AAC}$	AAC frequency of occurrence
HSRL	High Spectral Resolution Lidar
IAB	Integrated Attenuated Backscatter
IBS	Integrated aerosol Backscatter
InWA	Indian ocean, offshore from West Australia
LUT	Look Up Table
LWP	Liquid Water Path
MBL	Marine Boundary Layer
MCD43GF	MODIS BRDF/Albedo/NBAR CMG Gap-Filled Products
MODIS	MODerate Imaging Spectroradiometer
$\eta^{OWC}$	layer effective multiple scattering factor

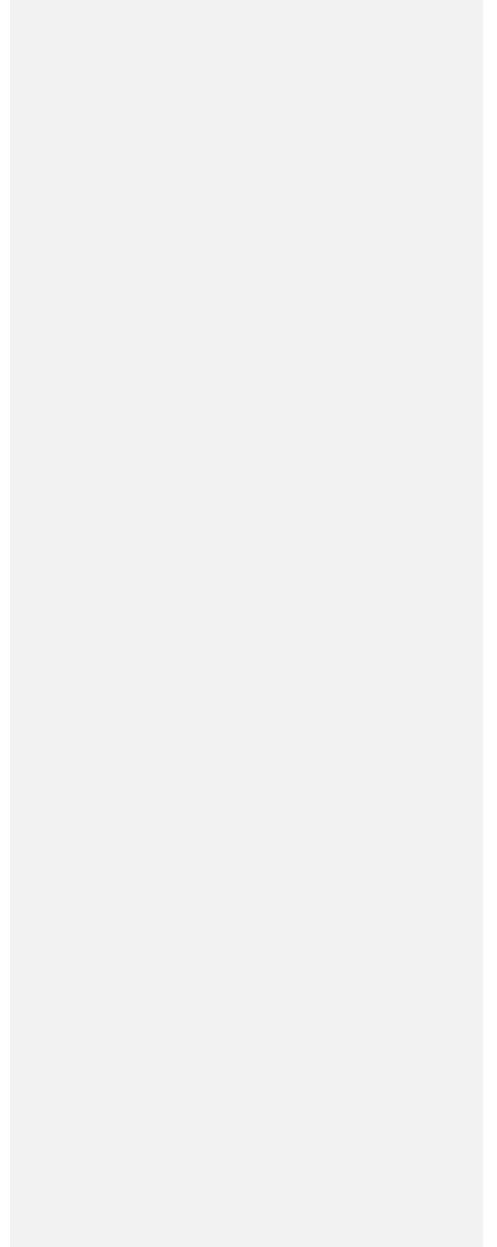
NEAs	North East Asia
NEPa	North East Pacific ocean
NWPa	North West Pacific ocean
OMI	Ozone Monitoring Instrument
ORACLES	ObseRvations of Aerosols above CLouds and their intEractionS
OWC	Opaque Water Cloud
POLDER	Polarization and Directionality of Earth's Reflectances
PBL	Planetary Boundary Layer
$R_e$	Cloud droplet effective radius
RT	Radiative Transfer scheme
$S_a$	Aerosol extinction-to-backscatter (lidar) ratio
$S_c$	Cloud extinction-to-backscatter (lidar) ratio
SCIAMACHY	Scanning Imaging Absorption Spectrometer for Atmospheric Cartography
SEAs	South East Asia
SEAt	South East Atlantic ocean
SEPa	South East Pacific ocean
SEVIRI	Spinning Enhanced Visible and InfraRed Imager
SNR	Signal-to-Noise Ratio
SS	Single Scattering
SSA	Single Scattering Albedo

Deleted:  $S_{AAC}$  ... [1]

SW            Short Wave  
TAt          Tropical Atlantic ocean  
TOA         Top Of Atmosphere

45

46



47 **1. Introduction**

48 The Direct Aerosol Radiative Effect (DARE) is defined as the change in the upwelling radiative flux  
49 ( $F^{\uparrow}$ ) at the top of the atmosphere (TOA) due to aerosols. Measured values of DARE depend on the  
50 accuracy and the geometry of the observation(s), the concentrations of various atmospheric constituents  
51 (e.g., aerosols, clouds, and atmospheric gases) and their radiative properties, and the Earth's surface  
52 reflectance. All-sky DARE ( $DARE_{all-sky}$ ) combines contributions from DARE under cloudy conditions  
53 ( $DARE_{cloudy}$ ) and DARE under cloud-free conditions ( $DARE_{non-cloudy}$ ):

54  $DARE_{all-sky} = DARE_{cloudy} \times \text{Cloud Fraction} + DARE_{non-cloudy} \times (1 - \text{Cloud Fraction})$  Eq. (1)

55 According to Yu et al., [2006], substantial progress has been made in the assessment of  $DARE_{non-cloudy}$   
56 using satellite and in situ data. Further evidence is provided in a companion to our study, Redemann et  
57 al. [2019], which use A-Train aerosol observations to constrain  $DARE_{non-cloudy}$  and compares the results  
58 with AeroCom (Aerosol Comparisons between Observations and Models) results (see Appendix A for  
59 further details). However, traditional passive aerosol remote sensing techniques are limited only to  
60 clear-sky conditions and significant efforts are required to estimate  $DARE_{cloudy}$ . Moreover, simulations  
61 of  $DARE_{cloudy}$  from various AeroCom models in Schulz et al. [2006] (see their figure 6) show large  
62 disparities. Our study focuses on Aerosol Above Cloud (AAC) scenes over the globe and subsequent  
63 estimates of  $DARE_{cloudy}$  (i.e., the instantaneous short wave (SW) upwelling TOA reflected radiative  
64 fluxes due to clouds only minus SW upwelling TOA fluxes due to clouds with overlying aerosols). Let  
65 us note that, ideally, TOA  $DARE_{cloudy}$  should include aerosols below, in-between and above clouds.  
66 Here we assume that TOA  $DARE_{cloudy}$  is only caused by aerosols above clouds. Table 1 lists TOA SW

Deleted: 2018

68 DARE<sub>cloudy</sub> results that use satellite observations in the literature, together with assumptions in their  
69 calculations. Compared to the peer-reviewed studies of Table 1, our study marks a departure on three  
70 accounts. First, most peer-reviewed DARE<sub>cloudy</sub> calculations focus primarily on the South East Atlantic  
71 (SEAt e.g., [Chand et al., 2009, Wilcox et al., 2012, Peters et al., 2011, De Graaf et al., 2012, 2014,  
72 Meyer et al., 2013, 2015, Peers et al., 2015, Feng and Christopher, 2015] in Table 1). Second, our  
73 results use a combination of A-Train satellite sensors (i.e., MODIS-OMI-CALIOP), instead of the  
74 Look-Up-Table (LUT) approach used in the other studies of Table 1, to obtain estimates of the intensive  
75 aerosol radiative properties above clouds. Third, the peer-reviewed global DARE<sub>cloudy</sub> calculations in  
76 Table 1 use standard products from the active satellite sensor Cloud Aerosol Lidar with Orthogonal  
77 Polarization (CALIOP) for either AAC Aerosol Optical Depth (AOD) and/or aerosol and cloud vertical  
78 distribution information in the atmosphere [Zhang et al., 2014, 2016, Matus et al., 2015, Oikawa et al.,  
79 2013]. In our case, we estimate DARE<sub>cloudy</sub> globally by using an alternate method applied to CALIOP  
80 Level 1 measurements [Hu et al., 2007b; Chand et al., 2008; Liu et al., 2015] to obtain AAC AOD and  
81 the AAC frequency of occurrence. In the sections below, we explain why we have used such a method,  
82 instead of other passive or active satellite sensor techniques.

83 **Table 1:** TOA SW DARE<sub>cloudy</sub> calculations that use satellite observations in the literature and specific  
84 assumptions in the calculations. See also the theoretical study by Chang and Christopher et al. [2017]  
85 (i.e. they impose fixed COD, Re, AOD, aerosol radiative properties, and aerosol / cloud vertical  
86 distribution) and the study by Costantino and Bréon et al. [2013] (their method uses MODIS-derived  
87 cloud microphysics that are not corrected for overlying aerosols). When not specified, the study uses the  
88 standard CALIOP data product; otherwise, it uses the DR (Depolarization Ratio) or CR (Color Ratio)

89 technique on CALIOP measurements. MODIS<sup>A</sup> and MODIS<sup>T</sup> respectively denote the AQUA or  
 90 TERRA platform. SEAt: South East Atlantic. LUT: Look Up Table. See acronyms for satellite sensors  
 91 MODIS, CALIOP, CloudSat, POLDER, CERES and AMSR-E.

Reference	Domain	Satellite sensor(s) used for DARE <sub>cloudy</sub> calculations			
		Cloud properties (e.g. COD, albedo, fraction)	AOD	Aerosol radiative properties (e.g. SSA, g)	Vertical distribution of aerosol and cloud
Chand et al. [2009]	SEAt	MODIS <sup>T</sup>	CALIOP <sup>CR</sup>	Fixed value	Assumed constant
Wilcox [2012]	SEAt	MODIS <sup>A</sup> , AMSR-E	CERES provides upwelling shortwave flux		
Peters et al. [2011]	Atlantic	MODIS <sup>A</sup> , AMSR-E	CERES provides upwelling shortwave flux		
De Graaf et al. [2012, 2014]	SEAt	Direct determination of DARE <sub>cloudy</sub> by building LUT of cloud and aerosol-free reflectances			
Meyer et al. [2013]	SEAt	MODIS <sup>A</sup>	CALIOP	LUT approach	CALIOP
Zhang et al. [2014, 2016]	Globe	MODIS <sup>A</sup> , CALIOP (uses probability density function of CALIOP above-cloud AOD and underlying MODIS COD)		LUT approach	CALIOP
Meyer et al. [2015]	SEAt	MODIS <sup>A</sup> (simultaneous retrieval of above-cloud AOD, COD and R <sub>c</sub> )		LUT approach	Assumed constant
Peers et al. [2015]	SEAt	POLDER (simultaneous retrieval of above-cloud aerosol OD, size and single scattering albedo, cloud optical depth and cloud top height)			
Feng and Christopher [2015]	SEAt	MODIS <sup>A</sup> , CERES	CERES provides upwelling shortwave flux		

Reference	Domain	Satellite sensor(s) used for DARE <sub>cloudy</sub> calculations			
		Cloud properties (e.g. COD, albedo, fraction)	AOD	Aerosol radiative properties (e.g. SSA, g)	Vertical distribution of aerosol and cloud
Matus et al. [2015]	Globe	CloudSat, MODIS <sup>A</sup> , CALIOP	CALIOP	LUT approach	CloudSat, CALIOP
Oikawa et al. [2013]	Globe	CALIOP, MODIS <sup>A</sup>	CALIOP	LUT approach	CALIOP
This study	Globe	MODIS <sup>A</sup>	CALIOP <sup>DR</sup>	MODIS <sup>A</sup> , OMI, CALIOP	Assumed constant

92

93 Table 2 lists some passive (i.e., Spinning Enhanced Visible and InfraRed Imager, SEVIRI, Moderate  
94 Resolution Imaging Spectroradiometer, MODIS, Polarization and Directionality of Earth's  
95 Reflectances, POLDER, Ozone Monitoring Instrument, OMI or the Scanning Imaging Absorption  
96 Spectrometer for Atmospheric Chartography, SCIAMACHY) and active (i.e., CALIOP and CloudSat)  
97 satellite sensors that were used to detect and quantify the AAC AODs. Among the peer-reviewed  
98 studies of Table 2, those few that present DARE<sub>cloudy</sub> results (see Table 1) are denoted by a “+” sign in  
99 the first column.

00 **Table 2:** Studies that observe AAC using passive and active satellite sensors (i.e., from left to right,  
01 SEVIRI, POLDER, CloudSat, OMI, MODIS, SCIAMACHY, CALIOP; see acronyms). When using  
02 CALIOP, the authors either use the standard Level 2 products (Std), the Depolarization method (DR)  
03 [Hu et al., 2007b] or the color ratio method (CR) [Chand et al., 2008]. SEAt stands for SE Atlantic,

- 04 SEAs for SE Asia, NEAs for NE Asia and TAt for Tropical Atlantic. The “+” sign in the first column
- 05 denotes the presence of DARE<sub>cloudy</sub> calculations.

	Reference	Domain	Satellite sensor(s) used for aerosol-above-cloud detection						
			SEVIRI	POLDER	CloudS	OMI	MODIS	SCIAMA	
1	Chang and Christopher [2016, 2017]	SEAt							
2	Waquet et al. [2013a]	Globe							
3	Waquet et al. [2009, 2013b]	SEAt, TAt							
4	Peers et al. [2015] <sup>+</sup>	SEAt							
5	Jethva et al [2013, 2014]	SEAt, TAt							
6	Torres et al. [2012]	SEAt							
7	Peters et al. [2011] <sup>+</sup>	Atlantic							
8	De Graaf et al. [2012, 2014] <sup>+</sup>	SEAt							
9	Meyer et al. [2015] <sup>+</sup>	SEAt							
10	Feng and Christopher [2015] <sup>+</sup>	SEAt							
11	Sayer et al. [2016]	SEAt, SEAs							
12	Matus et al. [2015] <sup>+</sup>	Globe							Std
13	Alfaro-Contreras et al. [2016]	Globe							Std
14	Alfaro-Contreras et al. [2014]	SEAt, SEAs							Std
15	Devasthale and Thomas [2011]	Globe							Std
16	Yu et al. [2012]	SEAt, TAt							Std
17	Wilcox [2012] <sup>+</sup>	SEAt							Std
18	Meyer et al. [2013] <sup>+</sup>	SEAt							Std
19	Zhang et al. [2014, 2016] <sup>+</sup>	Globe							Std
20	Oikawa et al. [2013] <sup>+</sup>	Globe							Std
21	Chung et al. [2016]	Globe							Std
22	Chand et al. [2008]	SEAt							CR, DR

	Reference	Domain	Satellite sensor(s) used for aerosol-above-cloud detection						
			SEVIRI	POLDER	CloudSat	SOMI	MODIS	SCIAMAC	CALIOP
23	Chand et al. [2009] <sup>+</sup>	SEAt							CR
24	Deaconu et al. [2017]	Globe							Std, DR
25	Liu et al. [2015]	SEAt, TAt							DR
26	This study <sup>+</sup>	Globe							DR

06

07 The brightening of clear patches near clouds [Wen et al., 2007] (i.e., “3-D cloud radiative effect” or  
08 “cloud adjacency effect”) can introduce biases into the current passive satellite AAC retrieval  
09 techniques (i.e., lines 1-11 of Table 2). To minimize these biases, this study relies primarily on CALIOP  
10 observations [Winker et al., 2009]. CALIOP is a three-channel elastic backscatter lidar with a narrow  
11 field of view and a narrow source of illuminating radiation, which limits cloud adjacency effects and the  
12 subsequent cloud contamination of aerosol data products [Zhang et al., 2005; Wen et al., 2007; Várnai  
13 and Marshak, 2009]. CALIOP measures high-resolution (1/3 km in the horizontal and 30m in the  
14 vertical in low and middle troposphere) profiles of the attenuated backscatter from aerosols and clouds  
15 at visible (532 nm) and near-infrared (1064 nm) wavelengths along with polarized backscatter in the  
16 visible channel [Hunt et al., 2009]. These data are distributed as part of the Level 1 CALIOP products.  
17 The Level 2 products are derived from the Level 1 products using a succession of sophisticated retrieval  
18 algorithms [Winker et al., 2009]. The Level 2 processing is composed of a feature detection scheme  
19 [Vaughan et al., 2009], a module that classifies features according to layer type (i.e., cloud versus  
20 aerosol) [Liu et al., 2010] and subtype (i.e., aerosol species) [Omar et al., 2009], and, finally, an  
21 extinction retrieval algorithm [Young and Vaughan, 2009] that retrieves profiles of aerosol backscatter  
22 and extinction coefficients and the total column AOD based on modeled values of the extinction-to-

23 backscatter ratio (also called lidar ratio and represented by the symbol  $S_a$ ) inferred for each detected  
24 aerosol layer subtype.

25 A few studies use standard CALIOP Level 2 Aerosol and Cloud Layer products to determine AAC  
26 occurrence over the globe (see line 12-21 in Table 2). However, a study by Kacenelenbogen et al.  
27 [2014] demonstrates that the standard version 3 CALIOP aerosol products substantially underreport the  
28 occurrence frequency of AAC when aerosol optical depths are less than  $\sim 0.02$ , mostly because these  
29 tenuous aerosol layers have attenuated backscatter coefficients less than the CALIOP detection  
30 threshold. CALIOP's standard extinction (and optical depth) data products are only retrieved between  
31 the tops and bases of detected features, and these boundaries may significantly underestimate the full  
32 vertical extent of the layer (Kim et al., 2017; Thorsen et al., 2017; Toth et al., 2018). Furthermore, the  
33 Kacenelenbogen et al. [2014] study found essentially no correlation between AAC AOD results  
34 reported by the CALIOP and collocated NASA Langley airborne High Spectral Resolution Lidar  
35 (HSRL). A subsequent study by Liu et al. [2015] shows that the CALIOP Level 2 standard aerosol data  
36 products underestimate dust AAC AOD by  $\sim 26\%$  over the Tropical Atlantic and smoke AAC AOD by  
37  $\sim 39\%$  over the SE Atlantic.

38 For these reasons, a few studies in Table 2 (see line 22-26) use alternate methods on Level 1 CALIOP  
39 products, such as the Color Ratio (CR) [Chand et al., 2008] or the Depolarization Ratio (DR) [Hu et al.,  
40 2007b; Liu et al., 2015] methods, instead of using the AOD reported in the CALIOP standard Level 2  
41 products.

42 In this study, we use the DR method and a combination of CALIOP Level 1 and Level 2 data products  
43 to compute global estimates of the AAC frequency of occurrence (i.e.,  $f_{AAC}$ ) and the AAC AOD (i.e.,  
44  $\tau_{AAC}^{DR}$ ) (section 2.1). We then use CALIOP results of  $f_{AAC}$ ,  $\tau_{AAC}^{DR}$  and other A-Train satellite products  
45 to compute global  $DARE_{cloudy}$  (section 2.2). Section 3 describes the geographical and seasonal  
46 distribution of global  $f_{AAC}$  (section 3.1),  $\tau_{AAC}^{DR}$  (section 3.2) and  $DARE_{cloudy}$  results (section 3.3).  
47 Section 4 revisits some of the limitations in the method and proposes ways to improve on these  
48  $DARE_{cloudy}$  calculations.

## 49 2. Method

### 50 2.1. AAC optical depth

51 [Because the CALIOP backscatter signal is totally attenuated below the lowest “feature” detected within](#)  
52 [any profile \[Vaughan et al., 2009\], this lowest feature is defined as being opaque. Approximately 69%](#)  
53 [of the time, the opaque feature detected in a profile is the Earth’s surface \[Guzman et al., 2017\]. In the](#)  
54 [remainder of the cases, the opaque feature is either a water cloud, an ice cloud, or, very rarely, an](#)  
55 [aerosol layer.](#)

56 The DR method, [which is also known as the “constrained opaque water cloud method” \[Liu et al.,](#)  
57 [2015\], relies on Opaque Water Clouds \(OWCs\) as reflectivity targets. The OWCs in this study are](#)  
58 [selected using the five criteria listed in Table B2 of the appendix. Most importantly, \(1\) only one cloud](#)  
59 [can be detected within a 5 km \(15 shot\) along-track average \(which means, for example, that marine](#)  
60 [stratus below thin cirrus are excluded\), and \(2\) this one cloud must be opaque \(i.e., lowest feature](#)  
61 [detected in a column, and not subsequently classified as a surface return\).](#) Furthermore, [all OWCs must](#)

Deleted: ,

Deleted: and the AAC extinction-to-backscatter ratios (i.e.,  $S_{AAC}$ )

Deleted: ,

Deleted: and  $S_{AAC}$

Deleted: and extinction-to-backscatter

Deleted: (

Deleted: )

Deleted: (

Deleted: )

Formatted: Space After: 0 pt

Deleted: can also be called

Deleted: as it uses

Deleted: this one cloud must be (2) opaque (which means that low but transparent clouds such as the ones reported in Leahy et al. [2012] are excluded),

76 [be](#) (3) spatially uniform (i.e., detected at single-shot resolution within every laser pulse included in the 5  
77 km averaging interval), (4) assigned a high confidence score by the CALIOP cloud-aerosol  
78 discrimination (CAD) algorithm and (5) identified as a high confidence water cloud by the CALIOP  
79 cloud phase identification algorithm. When there is aerosol above OWCs, the lidar backscatter signal  
80 received from the underlying water cloud is reduced in direct proportion to the two-way transmittance  
81 of the aerosol layer above. [However, because the DR retrieval technique requires backscatter  
82 measurements from opaque water clouds \[Hu et al. 2007b\], it cannot be used to retrieve AOD from  
83 aerosols lying above the low, transparent water clouds that are frequently observed over remote oceans,  
84 especially in the southern hemisphere \(e.g., Leahy et al. \[2012\]; Mace and Protat \[2018\]; O et al.  
85 \[2018\]\).](#)

86 Based on Hu et al. [2007a, 2007b], Eq. (2) describes how we compute  $\tau_{AAC}^{DR}$  using the DR method  
87 above OWCs.

$$88 \tau_{AAC}^{DR} = -0.5 \times \ln[IAB_{SS,AAC}^{OWC} / IAB_{SS,CAC}^{OWC}] \quad \text{Eq. (2)}$$

89 Here  $IAB_{SS,AAC}^{OWC}$  is the single scattering value (subscript SS) of the layer-integrated attenuated  
90 backscatter (IAB) for an OWC underlying one or more aerosol layer(s) above the cloud.  $IAB_{SS,CAC}^{OWC}$   
91 is the single scattering value of the IAB for an OWC underlying Clear air Above Cloud (CAC). By  
92 CAC, we mean that there are no aerosols detected above the OWC. In this study, we consider  $\tau_{AAC}^{DR}$   
93 valid when positive. According to Eq. (2), this means that  $IAB_{SS,AAC}^{OWC}$  needs to always be smaller in  
94 magnitude than  $IAB_{SS,CAC}^{OWC}$  and  $\tau_{AAC}^{DR}$  equals zero when  $IAB_{SS,AAC}^{OWC}$  equals  $IAB_{SS,CAC}^{OWC}$ .

Deleted: (  
Deleted: )  
Deleted: ,  
Deleted: ,  
Deleted: ,

00 Section B of the appendix provides additional information about the application of Eq. (2) and the  
01 various steps needed to derive  $\tau^{\text{DR}}_{\text{AAC}}$ . We list the selection criteria used to identify the OWC dataset in  
02 this study and describe the corrections required to obtain single-scattering estimates of IAB from  
03 measurements that contain substantial contributions from multiple scattering (B1). We also describe the  
04 technique used for distinguishing between CAC and AAC conditions (B2), and illustrate our derivation  
05 of an empirical parameterization of  $\text{IAB}^{\text{OWC}}_{\text{SS,CAC}}$  as a global function of latitude and longitude (B3).

06 As reported in Table 2, the CALIOP DR method was used to study the African dust transport pathway  
07 over the Tropical Atlantic [Liu et al., 2015] and the African smoke transport pathway over the South  
08 East Atlantic [Liu et al., 2015; Chand et al., 2008, 2009]. More recently, the CALIOP DR method was  
09 also used by Deaconu et al. [2017] to assess POLDER AAC AOD values [Waquet et al., 2009, 2013b  
10 and Peers et al., 2015] over the globe. In this study, we extend the previous regional studies of [Liu et  
11 al., 2015 and Chand et al., 2008, 2009] to derive global CALIOP-based AAC AOD estimates. Let us  
12 note that, in our study, the accuracy of  $\tau^{\text{DR}}_{\text{AAC}}$  depends on measurements of targets of very high signal-  
13 to-noise ratio (SNR) such as OWCs in clear skies and OWCs underlying aerosol layers.

## 14 2.2. AAC Direct Aerosol Radiative Effects

15 Having first retrieved global values of  $\tau^{\text{DR}}_{\text{AAC}}$  from the CALIOP measurements, we then compute  
16 global estimates of  $\text{DARE}_{\text{cloudy}}$  using DISORT (DIScrete ORDinate Radiative Transfer; Stamnes et al.,  
17 1988, Buras et al., 2011), a six-stream plane-parallel radiative transfer model with molecular absorption  
18 characterized by a correlated-k scheme [Fu and Liou, 1992] that is embedded within the LibRadtran  
19 Radiative Transfer (RT) package [Emde et al., 2016]. Hereafter, our seasonally and spatially gridded (4°

**Deleted:**  $S_{\text{AAC}}$  values are then computed by solving Eq. (15) of Fernald et al. [1972], constrained by valid (i.e., positive)  $\tau^{\text{DR}}_{\text{AAC}}$  and using the GEOS-5 molecular and ozone number density values and the CALIOP Level 1 attenuated backscatter profiles (see step S5 in Table B1).

**Deleted:** the ability to retrieve CALIOP  $S_{\text{AAC}}$  has no bearing on the accuracy of our CALIOP  $\tau^{\text{DR}}_{\text{AAC}}$  retrievals. T

**Deleted:** s

**Deleted:** On the other hand, many  $S_{\text{AAC}}$  retrievals depend on very low SNR measurements obtained from the weakly scattering and vertically diffuse aerosol layers above OWCs.

31 x 5°) averaged shortwave (SW) (250 nm to 5600 nm) global TOA  $DARE_{cloudy}$  results will be called  
32  $DARE_{OWC}$ , as they pertain to a specific category of clouds (i.e., OWCs) defined according to the  
33 CALIOP data selection criteria set forth in Table B2. We list the following input parameters to DISORT  
34 in order to derive estimates of  $DARE_{OWC}$ :

35 (1) **Atmospheric profiles** of pressure, temperature, air density, ozone, water vapor,  $CO_2$ , and  $NO_2$   
36 use standard US atmosphere profiles [Anderson et al., 1986].

37 (2) **Aerosol intensive radiative properties** (i.e. properties that depend solely on aerosol species,  
38 and are unrelated to the aerosol amount) are informed by seasonal maps ( $4^\circ \times 5^\circ$ , daytime in 2007)  
39 of combined MODIS-OMI-CALIOP (MOC) retrieved median spectral extinction coefficients,  
40 single scattering albedos and asymmetry parameters at 30 different wavelengths. As an example,  
41 Figure A1 in the appendix shows the seasonal maps of MOC SSA at 546.3 nm that were used in the  
42 calculation of  $DARE_{OWC}$ . These MOC retrievals, described in section A of the appendix, are at the  
43 basis of a companion study [Redemann et al., 2019]. Let us note that we only use the shape of the  
44 MOC extinction coefficient spectra and not its actual magnitude; the MOC spectral extinction  
45 coefficient spectra is normalized to the seasonal 2008-2012 average value of either  $\tau_{AAC}^{DR}$  or  $\tau_{AAC}^{DR}$   
46  $\times f_{AAC}$  within each grid cell. Our method assumes similar aerosol radiative properties above clouds  
47 and in near-by clear-sky regions.

48 (3) **Aerosol extensive radiative properties** (i.e., properties that depend on the aerosol amount  
49 present in the atmosphere) are informed by seasonal maps ( $4^\circ \times 5^\circ$ , nighttime from 2008 to 2012) of  
50 either CALIOP  $\tau_{AAC}^{DR}$  (see Eq. 2) or CALIOP  $\tau_{AAC}^{DR} \times f_{AAC}$ . We chose to use nighttime CALIOP

Deleted: 2018

52  $\tau_{AAC}^{DR}$  or  $\tau_{AAC}^{DR} \times f_{AAC}$  results in the estimation of  $DARE_{OWC}$  because, at nighttime, the CALIOP  
53 signal-to-noise-ratio (SNR) is not affected by ambient solar background and leads to a more  
54 accurate measurement of the aerosol signal (compared to daytime). By doing this, we implicitly  
55 chose a better accuracy in the aerosol extensive radiative properties over a temporal overlap  
56 between aerosol extensive (nighttime) and intensive (daytime) radiative properties.

57 (4) **Cloud albedos** are computed from cloud droplet effective radius ( $R_e$ ) and Cloud Optical Depth  
58 (COD) information inferred from MODIS averaged monthly  $1^\circ \times 1^\circ$  grids (i.e. liquid water cloud  
59 products of MYD08\_M3: “Cloud Effective Radius Liquid Mean Mean” and “Cloud Optical  
60 Thickness Liquid Mean Mean” [Platnick et al. 2015]) from 2008 to 2012 (see Equations 1-9 of Peng  
61 et al. [2002]). These maps are then further gridded (to  $4^\circ \times 5^\circ$ ) and seasonally averaged to match the  
62 format of the aerosol radiative properties. Appendix figure A2 shows the seasonal maps of MODIS  
63 COD that were used in the calculation of  $DARE_{OWC}$ .

64 (5) **Aerosol and cloud layer heights** are assumed constant over the globe (respectively between 3-  
65 4km and 2-3km in this study), similar to other studies in Table 1 (e.g., Meyer et al. [2015]).

66 (6) **Earth’s surface albedo** uses global gap-filled Terra and Aqua combined MODIS BRDF/albedo  
67 products. It uses the 16-day closest product (i.e., MCD43GF) to the middle of each season (i.e., Jan  
68 15<sup>th</sup> for DJF, April 15<sup>th</sup> for MAM, July 15<sup>th</sup> for JJA and October 15<sup>th</sup> for SON). In the open ocean,  
69 the Cox and Munk [1954] sea surface albedo parameterization is applied with a wind speed of 10  
70  $ms^{-1}$ .

71 Using these inputs, Daily  $DARE_{OWC}$  results for each of the  $4^\circ \times 5^\circ$  grid cells are obtained by averaging  
72 24 LibRadtran RT calculations, corresponding to 24 different sun positions at each hour of the day.  
24

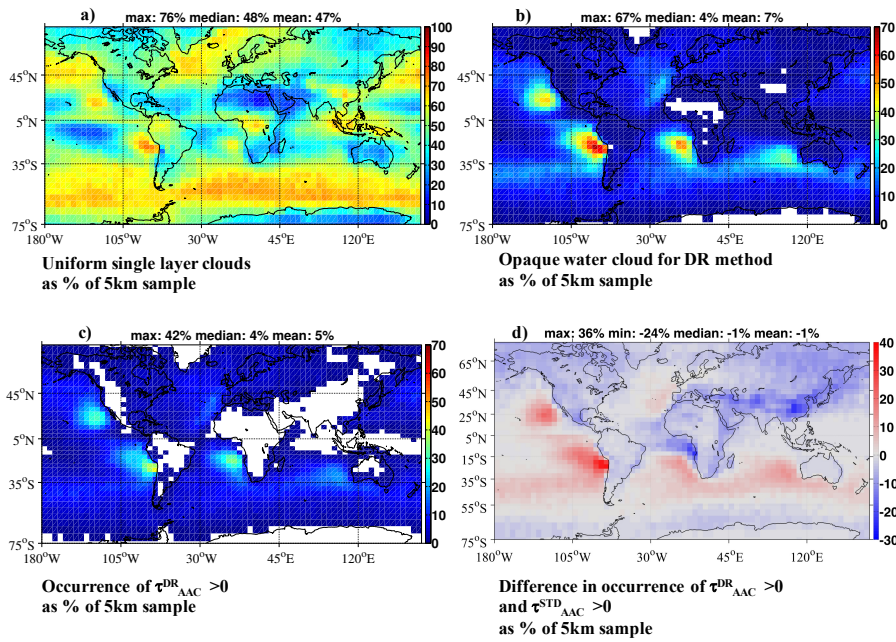
Formatted: Font: Not Bold

73 **3. Results**

74 **3.1. AAC Occurrence Frequencies**

75 To provide the necessary context for interpreting our TOA radiative transfer calculations, we first  
76 establish the observational AAC occurrence frequencies from which we will subsequently compute  
77 estimates of  $DARE_{OWC}$ . Figure 1 illustrates the annual gridded mean (5 years) global occurrence  
78 frequencies of a) single layer clouds, b) opaque water clouds that are suitable for the DR method and c)  
79 aerosol-above-clouds cases using the DR method. Figure 1d) shows the difference between the number  
80 of AAC cases using the DR method (i.e., number of cases with  $\tau_{AAC}^{DR} > 0$ ) and the number of AAC  
81 cases using the standard Version 3 CALIOP product.

82



83

84 **Figure 1:** During nighttime, from 2008 to 2012 on a 4°x5°-grid: Occurrence frequencies of (a) uniform  
 85 single layer clouds (C1-C3 of Table B2), (b) opaque water clouds suitable for the DR method (C1-C5 of  
 86 Table B2; these clouds can be obstructed or unobstructed) and (c) AAC cases that show a positive  
 87  $\tau_{AAC}^{DR}$  at 532 nm. (d) shows the difference between the number of AAC cases using the DR method  
 88 (i.e., number of cases with  $\tau_{AAC}^{DR} > 0$ ) and the number of AAC cases using the standard Version 3  
 89 CALIOP product (i.e., number of cases with  $\tau_{AAC}^{STD} > 0$ ); CALIOP AAC cases using the standard  
 90 algorithm are defined as 5 km-columns showing an uppermost layer classified as aerosols and a cloud  
 26

91 layer anywhere below that aerosol layer; the cloud itself does not have to satisfy any of the criteria of  
92 Table B2. Grid cells are 4° x 5° latitude/ longitude. The percentages in (a)-(d) use the number of 5 km  
93 CALIOP samples within each grid cell as a reference. White pixels show either no CALIOP  
94 observations, no CALIOP OWC detection, a small number of CALIOP unobstructed OWCs or a small  
95 number of positive  $\tau_{AAC}^{DR}$  values. The title of each map shows the global maximum, median and mean  
96 values.

97

98 Uniform single layer clouds (i.e. C1-C3 of Table B2) are detected in ~47% of all 5 km CALIOP  
99 samples over the globe (see Figure 1(a)). In other words, at any one time, approximately half of the  
00 globe is covered by uniform single layer clouds. As expected, the highest occurrence of those clouds is  
01 in the high and low latitude bands and especially over the southern oceans. According to Figure 1(b),  
02 OWCs suitable for the DR method (i.e. C1-C5 of Table B2) are mostly in the marine stratocumulus  
03 regions and represent a mean of 7% of all 5 km CALIOP samples over the globe. This significant  
04 reduction from half-the-globe coverage is explained by the five criteria used to select OWCs for the  
05 application of the DR method (i.e., C1-C5 of Table B2). The highest occurrence of OWCs can be found  
06 offshore from the west coasts of North and South America, southwest Africa and Australia. In  
07 particular, OWC cover ranges from 60 to 75 % over the region of SE Atlantic in August [Klein and  
08 Hartmann, 1993]. Also, the southeastern Pacific region off the Peruvian and Chilean coasts is the  
09 location of the largest and most persistent stratocumulus deck in the world [Klein and Hartmann, 1993].  
10 The percentage of AAC cases (i.e., AAC cases showing positive  $\tau_{AAC}^{DR}$ ) at the basis of our study is

11 very small compared to the total number of 5 km CALIOP profiles per grid cell (i.e. mean of 5% on  
12 Figure 1(c)). This is primarily due to a small number of low OWC used for the DR method over the  
13 globe (when comparing Figure 1(a) and 1(b)).

14 Figure 1(d) illustrates the difference in occurrence frequencies of AAC cases using the DR method  
15 compared to the standard Version 3 CALIOP product. Negative values, shown in blue, indicate the

16 fraction of cases for which the DR method fails to detect above-cloud aerosols that are reported in the  
17 standard CALIOP product. Similarly, positive values, shown in red, indicate the number of cases for  
18 which above-cloud aerosols are detected by the DR method but not reported in the standard CALIOP

19 data product. Unlike the AAC cases detected using the DR method, the AAC cases obtained from the  
20 CALIOP standard product do not impose any restrictions on the nature of the underlying clouds.

21 Instead, the CALIOP standard product reports aerosol detected above both opaque and transparent  
22 clouds, irrespective of cloud thermodynamic phase. The blue regions in Fig. 1(d) show that, relative to  
23 the CALIOP standard product, our implementation of the DR method could be failing to detect AAC

24 cases over most of land surfaces and over the Arabian Sea, the Tropical Atlantic, and the SE Atlantic  
25 regions. The lack of AAC cases offshore from the southwest coast of Africa in the DR method dataset is

26 the result of our conservative data filtering strategy. Because the IABs of aerosol-contaminated OWCs  
27 can differ significantly from those measured in pristine, aerosol-free conditions, OWCs suspected of  
28 being aerosol-contaminated (which are ubiquitous in this part of the world and very common over

29 continents) are specifically excluded from our DR method analyses (see appendix section B3 for more  
30 details). However, some regions such as the NE and SE Pacific exhibit up to 40% more AAC cases

31 when using the DR method. The SE Pacific region, especially offshore from Chile, shows particularly  
28

Deleted: ;

Deleted: negative (positive) values in blue (red) show the number of AAC cases that are missed (gained) by the DR method compared to using the standard CALIOP products. Unlike Figure 1(c),

Deleted: in Figure 1(d) that use

Deleted: require any assumptions

Deleted: Figure

Deleted: s

Deleted: that we could be missing (in blue)

Deleted: the

Deleted: by using the DR method instead of the standard CALIOP product. One reason for the lack of AAC cases offshore from the west coast of Africa in our dataset is the filtering out of "unobstructed" but potentially aerosol-contaminated OWCs (see section B3 in the appendix for more details).

Deleted: (in red)

48 tenuous aerosols, with attenuated backscatter values that typically fall below the CALIOP detection  
49 limit, thus hampering the detection of AAC using the standard CALIOP algorithm [Kacenelenbogen et  
50 al., 2014].

51 In the rest of this study, the frequency of occurrence of AAC,  $f_{AAC}$ , is defined as:

$$52 f_{AAC} = N_{AAC} / N_{OWC} \quad \text{Eq. (3)}$$

53 where  $N_{AAC}$  is the number of AAC cases (i.e., cases showing a positive  $\tau_{AAC}^{DR}$  at 532nm) and  $N_{OWC}$  is  
54 the number of OWCs within each  $4^\circ \times 5^\circ$  grid cell. Let us note that different studies use different  
55 references when computing the frequency of occurrence of AAC. The definition in Eq. (3) is similar to  
56 the one in Zhang et al. [2016] (see their Eq. (1)) and different from Devasthale and Thomas [2011],  
57 where  $f_{AAC}$  is defined as the ratio of AAC cases to the total number of CALIOP observations (similar to  
58 what is shown on Fig. 1(c)).

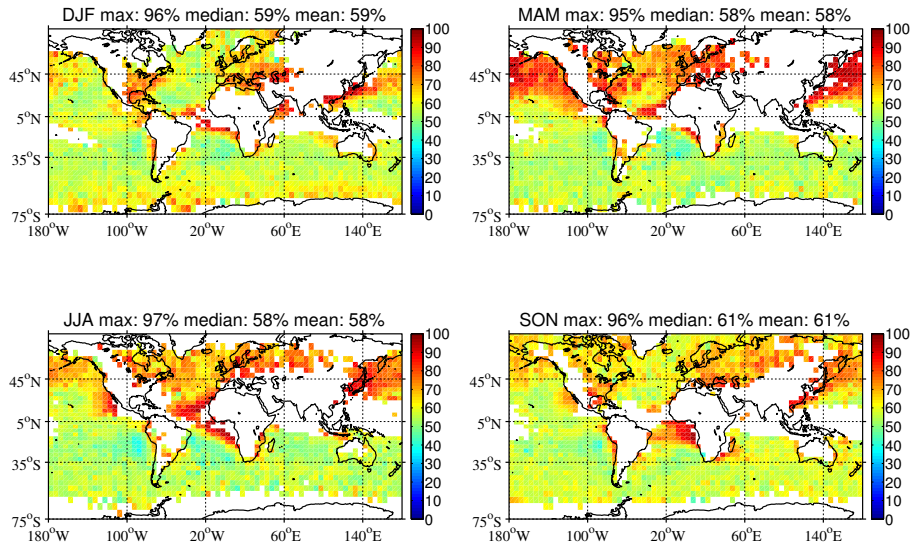
59 Figure 2 illustrates the global seasonal  $f_{AAC}$  (see Eq. 3) from 2008 to 2012. We find a median global  
60  $f_{AAC}$  of 58% to 61% with regional values that can reach more than 80% in some regions such as the SE  
61 Atlantic, especially during the JJA season. The AAC occurrence frequencies in Fig. 2 generally agree  
62 with previous findings [Zhang et al., 2016; Devasthale and Thomas, 2011] on the location and season of  
63 highest  $f_{AAC}$ .

64

Deleted: and, hence,

Deleted: s

67



68

69 **Figure 2:** Global seasonal 4°x5° nighttime AAC occurrence frequency (noted  $f_{AAC}$ , see Eq. (3)) from  
70 2008 to 2012. White pixels show either no CALIOP observations, a limited number of CALIOP  
71 unobstructed OWCs or a limited number of positive  $\tau_{AAC}^{DR}$  values. White pixels are not considered in  
72 the global mean and median  $f_{AAC}$  values in the title of each map. The title of each map shows the global  
73 maximum, median and mean values.

74

### 75 3.2. AAC Optical Depths

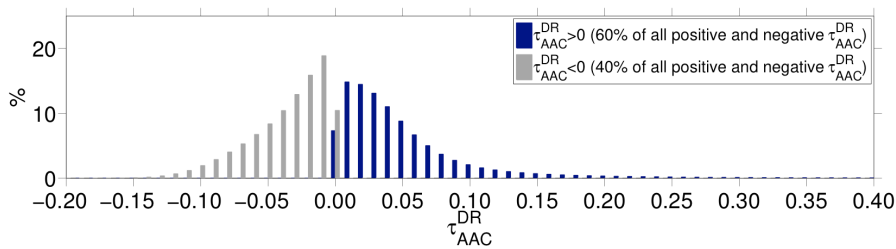
Deleted: , Extinction-to-Backscatter Ratios and South Atlantic Anomaly Effects

30

78 Figure 3 introduces the global, nighttime and multi-year (2008-2012) AAC optical depths ( $\tau_{AAC}^{DR}$ , see  
79 Eq. 2) dataset that was computed in this study.

Deleted: 3.2.1 AAC Optical Depths

80



81

82 **Figure 3:** Global distribution of  $\tau_{AAC}^{DR}$  at 532 nm. Positive (i.e., valid)  $\tau_{AAC}^{DR}$  values are in dark blue  
83 (N~3.4M) and negative  $\tau_{AAC}^{DR}$  values in grey (N~2.2M). These are nighttime CALIOP measurements  
84 from 2008-2012.

85 About 40% (i.e. 2.2M data points) of the initial dataset (i.e. N~5.6M) shows negative  $\tau_{AAC}^{DR}$  values and  
86 were flagged as invalid data (see Figure 3, in grey). When looking at all valid (i.e. positive)  $\tau_{AAC}^{DR}$   
87 values (blue), we show a majority of very small  $\tau_{AAC}^{DR}$  values in the 0.01-0.02 AOD range. This agrees  
88 with the findings of Devasthale and Thomas [2011]. Let us note that averaging all data points per  $4^{\circ} \times 5^{\circ}$   
89 grid cell (instead of the native resolution shown on Fig. 3) increases the AOD bin of maximum AAC  
90 occurrence globally from 0.01 (Fig. 3) to 0.03.

91 Table 3 shows four different ways of computing global seasonal and annual averages of aerosol optical  
92 depth above clouds: we use either  $\tau_{AAC}^{DR}$  or  $\tau_{AAC}^{DR} \times f_{AAC}$  (see Case I-II or III-IV) and then either (i)

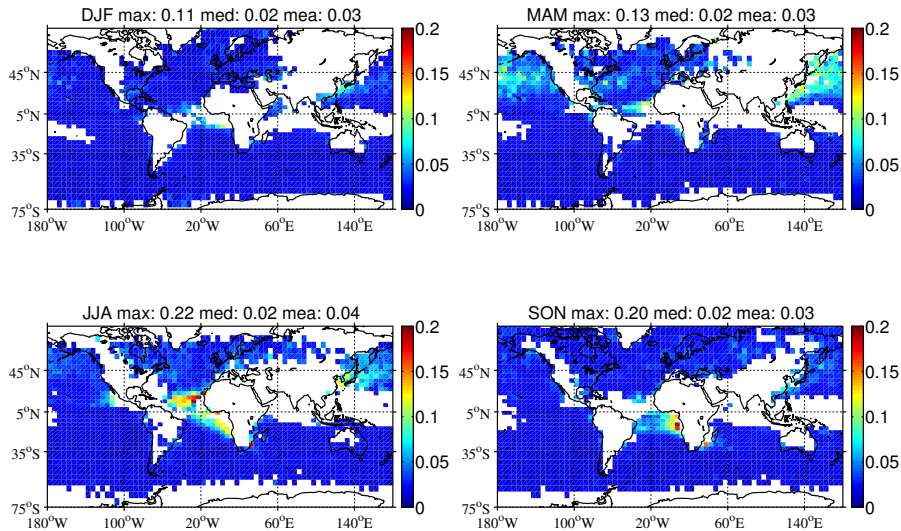
94 exclude all cases of  $\tau_{AAC}^{DR} < 0$  from the average (i.e., as in Case I and Case III), or (ii) set all cases of  
 95  $\tau_{AAC}^{DR} < 0$  to zero, and include these samples in the averages (i.e., as in Case II and Case IV). Let us  
 96 note that using  $\tau_{AAC}^{DR} \times f_{AAC}$  (instead of  $\tau_{AAC}^{DR}$ ) acknowledges the fact that some OWCs present no  
 97 overlying aerosols. In this case, we assume that when the DR technique retrieves an invalid AAC  
 98 measurement,  $f_{AAC} = 0$  and there are no aerosols above the cloud.

99 **Table 3:** Global seasonal and annual averages of  $\tau_{AAC}^{DR}$  (Case I and II) or  $\tau_{AAC}^{DR} \times f_{AAC}$  (Case III and  
 00 IV) when assuming either (i)  $\tau_{AAC}^{DR} < 0$  cases are excluded from the averages (Case I and III) or  
 01 (ii)  $\tau_{AAC}^{DR} < 0$  cases are set to zero and included in the averages (Case II and IV). Annual averages here  
 02 (last column) are the mean of the seasonal averages.

Global mean aerosol optical depth	DJF	MAM	JJA	SON	Annual
Case I $\tau_{AAC}^{DR}$ , invalid $\tau_{AAC}^{DR}$ excluded	0.04	0.05	0.05	0.05	0.05
Case II $\tau_{AAC}^{DR}$ , invalid $\tau_{AAC}^{DR} = 0$	0.02	0.02	0.02	0.02	0.02
Case III $\tau_{AAC}^{DR} \times f_{AAC}$ , invalid $\tau_{AAC}^{DR}$ excluded	0.03	0.03	0.04	0.03	0.03
Case IV $\tau_{AAC}^{DR} \times f_{AAC}$ , invalid $\tau_{AAC}^{DR} \times f_{AAC} = 0$	0.01	0.01	0.01	0.01	0.01

03 Figure 4 shows global seasonal nighttime median  $\tau_{AAC}^{DR} \times f_{AAC}$  from 2008 to 2012 (i.e., as in Case III  
 04 of Table 3). The title of each seasonal map (respectively DJF, MAM, JJA, SON) in Figure 4 shows the  
 05 global maximum (respectively 0.11, 0.13, 0.22, 0.20), median (0.02 for all seasons) and mean (0.03 in  
 06 DJF, MAM and SON and 0.04 in JJA)  $\tau_{AAC}^{DR} \times f_{AAC}$  values.

07



08

09 **Figure 4:** Global seasonal  $4^\circ \times 5^\circ$  nighttime median  $\tau^{\text{DR}}_{\text{AAC}} \times f_{\text{AAC}}$  from 2008 to 2012. Underlying clouds  
10 satisfy the criteria in Table B2. White pixels show either no CALIOP observations, a limited number of  
11 CALIOP unobstructed OWCs or a limited number of positive  $\tau^{\text{DR}}_{\text{AAC}}$  values. White pixels are not  
12 included when calculating the global mean and median  $\tau^{\text{DR}}_{\text{AAC}}$  values in the title of each map (i.e., as in  
13 Case III in Table 3). Note that if the white pixels were set equal to zero, the seasonal and annual global  
14  $\tau^{\text{DR}}_{\text{AAC}}$  values would correspond to Case IV in Table 3. The title of each map shows the global  
15 maximum, median and mean values.

16

33

Deleted: 2

18 We do not expect the  $\tau_{AAC}^{DR} \times f_{AAC}$  values of Figure 4 to be similar to the results of [Zhang et al., 2014,  
 19 Devasthale and Thomas, 2011, Alfaro-Contreras et al., 2016 or Yu and Zhang, 2013] (see Table 2) as  
 20 these studies use standard CALIOP Level 2 aerosol and cloud layer products for AAC observations,  
 21 instead of using the DR method. On the other hand, the results of Figure 4 seem to be in qualitative  
 22 agreement with the global AAC AOD derived from spaceborne POLDER observations [Waquet et al.,  
 23 2013a]. Let us note that Waquet et al. [2013a] have to assume an underlying COD larger than 3 to  
 24 ensure the saturation of the polarized light scattered by the cloud layer. Although Deaconu et al. [2017]  
 25 make different assumptions in the application of the DR method on CALIOP measurements (e.g., they  
 26 impose a constant cloud lidar ratio for OWCs with clear air above), they find that POLDER and  
 27 CALIOP  $\tau_{AAC}^{DR}$  are in good agreement over the SE Atlantic ( $R^2 = 0.83$ ) and over the Tropical Atlantic  
 28 ( $R^2 = 0.82$ ) from May to October 2008.

### 3.3. AAC Direct Aerosol Radiative Effects

#### 3.3.1. Global results of $DARE_{OWC}$

32 Figure 5 shows the seasonal TOA SW  $DARE_{OWC}$  estimates ( $W \cdot m^{-2}$ ) that use CALIOP  $\tau_{AAC}^{DR} \times f_{AAC}$   
 33 (see Fig. 4) as input to a radiative transfer model, together with the other parameters described in  
 34 section 2.2.  $DARE_{OWC}$  in Fig. 5 is set equal to zero (i.e., white pixels) if  $DARE_{OWC}$  is invalid or  
 35 missing.

Deleted: 7

#### Deleted: 3.2.2. Extinction-to-Backscatter Ratios

Figure 5 illustrates global seasonal gridded nighttime median AAC extinction-to-backscatter ratio ( $S_{AAC}$ ) values from 2008 to 2012 (section 2.2. describes the calculation of  $S_{AAC}$ ). Bréon [2013] uses POLDER's specific directional signature close to the backscatter direction to derive aerosol extinction-to-backscatter values over the globe. Figure 4 of Bréon [2013], although in clear-sky conditions (compared to above OWCs in our case), seems to be in qualitative agreement with Figure 5. However, Bréon [2013] seems to not detect sufficient aerosol signals in the SE Pacific region to reach any conclusions.

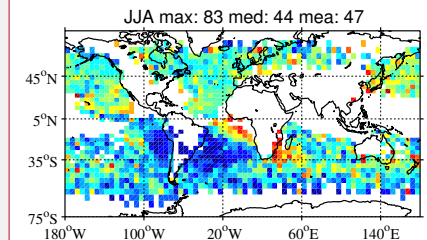
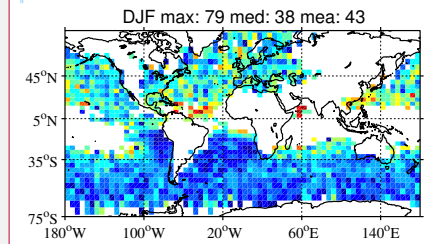
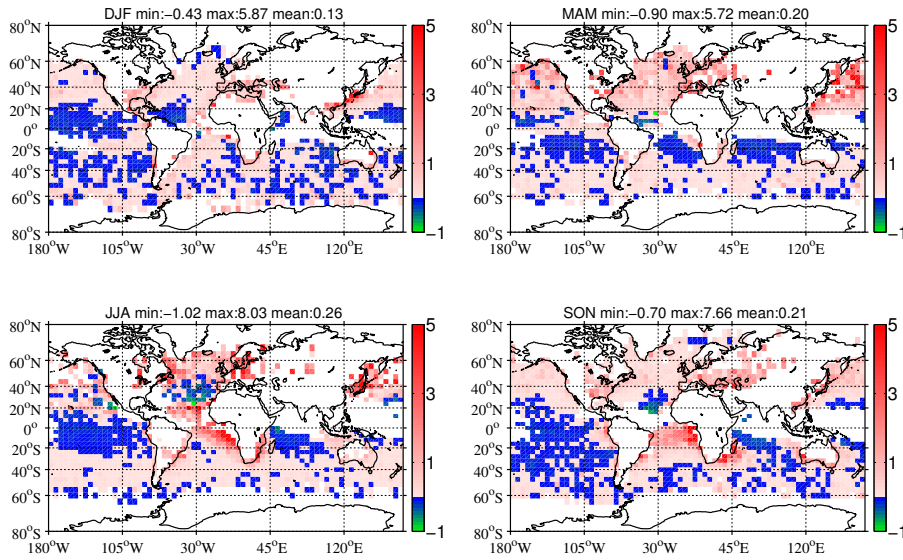


Figure 5: Global seasonal  $4^{\circ} \times 5^{\circ}$  nighttime median  $S_{AAC}$  at 532 nm (sr) from 2008 to 2012. Underlying clouds satisfy the criteria in Table B2. White pixels show a limited number of CALIOP OWCs, positive  $\tau_{AAC}^{DR}$  or valid  $S_{AAC}$  values (i.e. positive value, the solution has converged and/or the relative difference in  $\tau_{AAC}^{DR}$  is below 0.01). White pixels are not considered in the global mean and median  $S_{AAC}$  values in the title of each map. The title of each map shows the global maximum, median and mean values.

For reference, Table B3 in the appendix lists values of aerosol extinction-to-backscatter (lidar) ratios at 532 nm for different aerosol types (e.g. marine, urban industrial pollution, desert dust, polluted dust, biomass burning) reported in the literature. According to Table

Deleted: 7

Deleted: 7



09

10 **Figure 5:** Global seasonal 4°x5° TOA SW DARE<sub>owc</sub> estimates (W·m<sup>-2</sup>, as described in section 2.2). A  
 11 white pixel is counted as DARE<sub>owc</sub>=0 in the global mean DARE<sub>owc</sub> values in the title of each map.  
 12 White pixels show a limited number of CALIOP OWCs, positive  $\tau^{\text{DR}}_{\text{AAC}}$  values or auxiliary MODIS-  
 13 OMI-CALIOP combined satellite observations. The title of each map shows the global minimum,  
 14 maximum, and mean values.

15

Deleted: 7

17 Similar to TOA  $DARE_{cloudy}$  values from combined A-Train satellites in Oikawa et al. [2013] (see their  
18 Fig. 10) and from General Circulation Models (GCMs) (e.g. SPRINTARS) in Schulz et al. [2006] (see  
19 their Fig. 6 and 7), TOA  $DARE_{OWC}$  values in Fig. 5 are mostly positive (i.e., a warming effect due to  
20 less energy leaving the climate system) over the globe. We find, globally, 72% positive  $4^{\circ} \times 5^{\circ}$   
21  $DARE_{OWC}$  values (i.e.,  $N=4045$ ) against 28% negative values (i.e.,  $N=1581$ ) when considering all four  
22 seasons on Fig. 5. On the other hand, the highest negative TOA  $DARE_{OWC}$  values on Fig. 5 (i.e.,  
23 cooling effects shown in green pixels) are over the Tropical Atlantic (in MAM, JJA and SON), in the  
24 Pacific Ocean offshore from Mexico (in JJA) and at the periphery of the Arabian Sea (in JJA).

25 There are multiple ways to compute the global seasonal and annual  $DARE_{cloudy}$  averages (i.e.,  
26  $DARE_{OWC}$  in our case), and it is not clear which method would bring us closer to the true  $DARE_{cloudy}$   
27 state of the planet. For this reason, we list several different methods in Table 4. We either use CALIOP  
28  $\tau_{AAC}^{DR}$  or CALIOP  $\tau_{AAC}^{DR} \times f_{AAC}$  (Case I-II or III-IV) and we either exclude invalid  $DARE_{OWC}$  values  
29 or set invalid  $DARE_{OWC} = 0$  (Case I-III or II-IV). For completeness and as an intermediate step towards  
30  $DARE_{all-sky}$  (see Eq. 1), Case V and VI show the global seasonal averages of  $DARE_{OWC} \times$  Cloud Fraction  
31 (CF), instead of  $DARE_{OWC}$ . The CF values use monthly MODIS AQUA MYD08\_M3 products (variable  
32 “Cloud Retrieval Fraction Liquid FMean”), which are seasonally averaged and  $4^{\circ} \times 5^{\circ}$ -gridded.

33  
34 **Table 4:** Global seasonal and annual averages of TOA SW  $DARE_{OWC}$  estimates ( $W \cdot m^{-2}$ , as described in  
35 section 2.2). Annual averages (last column) are the mean of the seasonal averages (e.g., 0.53 for Case I  
36 is the average of 0.34, 0.52, 0.71 and 0.56); CF stands for Cloud Fraction.

Deleted: 7

Deleted: 7

Deleted: 7

Deleted: 5

Deleted: 5

Global averaged $DARE_{cloudy}$ ( $W \times m^{-2}$ )	DJF	MAM	JJA	SON	Annual
Case I $DARE_{OWC}, \tau^{DR}_{AAC}$ , invalid $DARE_{OWC}$ excluded	0.34	0.52	0.71	0.56	0.53
Case II $DARE_{OWC}, \tau^{DR}_{AAC}$ , invalid $DARE_{OWC}=0$	0.19	0.26	0.35	0.29	0.27
Case III $DARE_{OWC}, \tau^{DR}_{AAC} \times f_{AAC}$ , invalid $DARE_{OWC}$ excluded	0.24	0.40	0.53	0.40	0.39
Case IV $DARE_{OWC}, \tau^{DR}_{AAC} \times f_{AAC}$ , invalid $DARE_{OWC}=0$	0.13	0.20	0.26	0.21	0.20
Case V $DARE_{OWC} \times CF, \tau^{DR}_{AAC}$ , invalid $DARE_{OWC}$ excluded	0.11	0.16	0.25	0.19	0.18
Case VI $DARE_{OWC} \times CF, \tau^{DR}_{AAC} \times f_{AAC}$ , invalid $DARE_{OWC}=0$	0.04	0.06	0.09	0.07	0.07

42

43 Global seasonal and annual  $DARE_{OWC}$  averages (see titles in Fig. 5 and Table 4) in our study represent  
 44 the surface area of each grid cell. Each valid  $DARE_{OWC}$  value per pixel on each map of Fig. 5 is  
 45 multiplied by the surface of the pixel. These values per grid cell are then summed up and divided by the  
 46 sum of the surface of all valid grid cells.

Deleted: 7  
 Deleted: 5  
 Deleted: 7

47 Figure 5 corresponds to the setting of Case IV in Table 4. The reason why we have selected to  
 48 showcase this setting is because it closely resembles the settings of the  $DARE_{cloudy}$  calculations in  
 49 Zhang et al. [2016]; i.e., it assumes  $DARE = 0$  when CALIOP cannot detect an aerosol layer. Figure 5  
 50 shows positive global seasonal  $DARE_{OWC}$  averages between 0.13 and 0.26  $W \cdot m^{-2}$  (and an annual  
 51 average of 0.20  $W \cdot m^{-2}$  in Table 4) as well as the lowest  $DARE_{OWC}$  values when compared to  $DARE_{OWC}$

Deleted: 7  
 Deleted: 5  
 Deleted: 7  
 Deleted: 5

37

59 values from Case I through Case IV in Table 4. These values are nonetheless much larger than the  
60 global annual ocean DARE<sub>cloudy</sub> values reported in Zhang et al. [2016] and Schulz et al. [2006] (e.g.,  
61 annual average of  $0.015 \text{ W} \times \text{m}^{-2}$  reported over ocean in Zhang et al. [2016]). Moreover, Matus et al.  
62 [2015] find (see their Table 2) a global TOA DARE<sub>cloudy</sub> value of  $0.1 \text{ W} \cdot \text{m}^{-2}$  over thick clouds (these  
63 clouds are similar to our study), compensated by a global TOA DARE<sub>cloudy</sub> value of  $-2 \text{ W} \cdot \text{m}^{-2}$  over thin  
64 clouds.

65 Section 3.3.2 further analyzes DARE<sub>owc</sub>, together with  $f_{\text{AAC}}$ ,  $\tau^{\text{DR}}_{\text{AAC}}$ , SSA, and COD results in a few  
66 selected regions and compares these results to previous studies.

### 67 **3.3.2. Regional results of DARE<sub>owc</sub>**

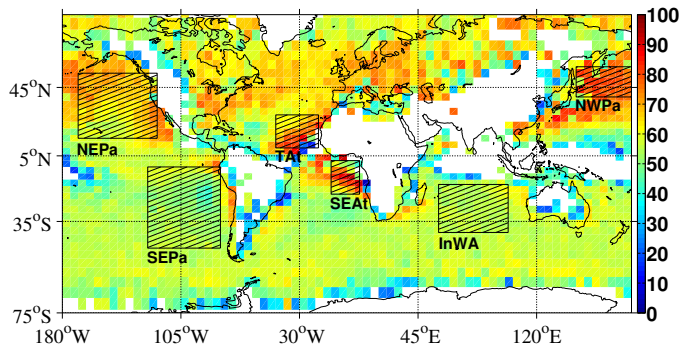
68 The  $f_{\text{AAC}}$  results in Fig. 2 help us define six major AAC “hotspots” over the North East Pacific (NEPa),  
69 South East Pacific (SEPa), Tropical Atlantic (TAt), South East Atlantic (SEAt), Indian ocean, offshore  
70 from West Australia (InWA), and North West Pacific (NWPa). To assist in the analysis of the  
71 remaining figures in this study, Figure 6 and Table 5 briefly describe these six AAC hotspots.

72

Deleted: 5

Deleted: 8

Deleted: 6



76  
 77 **Figure 6:** Six regions of high AAC occurrence, further defined in Table 5. Background map is the  
 78 global annual  $4^\circ \times 5^\circ$  nighttime AAC occurrence frequency ( $f_{AAC}$ , see Eq. 3 and Fig. 2 for seasonal  $f_{AAC}$   
 79 maps). Global annual maximum, median and mean  $f_{AAC}$  values are respectively 93%, 57% and 57%.

Deleted: 8  
 Deleted: 6

80  
 81 **Table 5:** Six regions of high AAC occurrence (see Fig. 6), their season of highest AAC occurrence and  
 82 its corresponding mean  $f_{AAC}$  value

Deleted: 6  
 Deleted: 8

Region	[latitude; longitude]	Season of most $f_{AAC}$
North East Pacific Ocean (NEPa)	[16N, 52N; 170W, 120W]	MAM (80%)
South East Pacific Ocean (SEPa)	[49S, 2S; 126W, 80W]	DJF (55%)
Tropical Atlantic Ocean (TAT)	[10N, 30N; 45W, 18W]	JJA (80%)
South East Atlantic Ocean (SEAt)	[19S, 2N; 10W, 8E]	SON (87%)
Indian Ocean, offshore from West Australia (InWA)	[41S, 13S; 58E, 102E]	SON (60%)
North West Pacific Ocean (NWPa)	[40N, 55N; 145E, 180E]	MAM (90%)

87

88 Figure 7a illustrates the mean regional, seasonal or annual estimates of SW TOA  $DARE_{OWC}$  ( $W \cdot m^{-2}$ ) in  
89 each region of Table 5. Figure 7b-7f show the primary parameters used in the  $DARE_{OWC}$  calculations  
90 (see section 2.2): the mean regional, seasonal or annual (b) percentage of grid cells that show valid (i.e.,  
91 positive)  $f_{AAC} \times \tau^{DR}_{AAC}$  values compared to the total number of  $4^\circ \times 5^\circ$  pixels in each region, (c)  
92 CALIOP  $f_{AAC}$  values, (d) CALIOP  $f_{AAC} \times \tau^{DR}_{AAC}$  values, (e) assumed overlying SSA values at 546.3 nm  
93 and (f) assumed underlying COD values from MODIS.

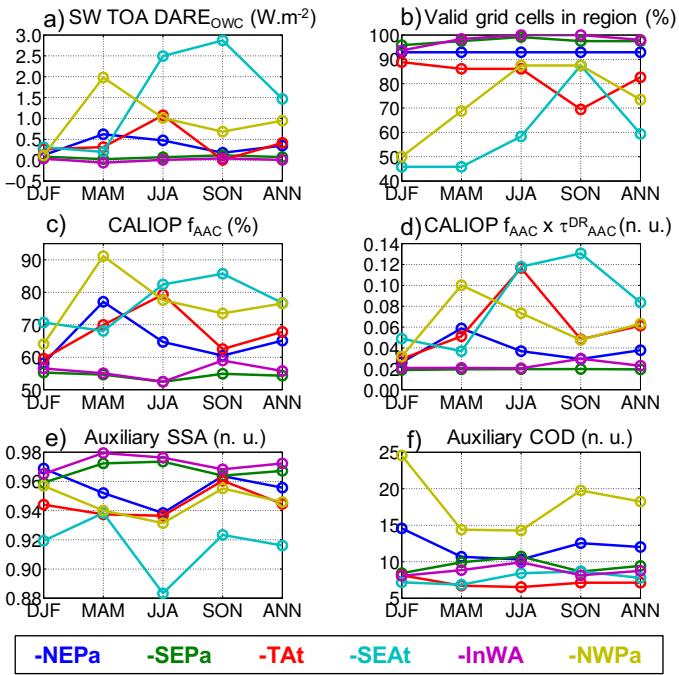
94

Deleted: 9

Deleted: 6

Deleted: 9

Deleted: 9



00

01 **Figure 7:** Mean regional, seasonal or annual (a) estimated SW TOA DARE<sub>OWC</sub> (W·m<sup>-2</sup>, calculation is  
 02 described in section 2.2), (b) percentage of grid cells that show valid f<sub>AAC</sub> x τ<sup>DR</sup><sub>AAC</sub> (i.e., positive)  
 03 values compared to the total number of 4° x 5° pixels in each region, (c) CALIOP f<sub>AAC</sub> (%), (d) f<sub>AAC</sub> x  
 04 τ<sup>DR</sup><sub>AAC</sub> (no unit), (e) assumed overlying SSA at 546.3 nm from a combination of MODIS-OMI-

Deleted: 9

06 CALIOP and (f) assumed underlying COD from MODIS in each region of Table 5. DARE<sub>owc</sub> in (a) is  
 07 computed using the case IV of Table 4.

Deleted: 6

Deleted: 5

09 Table 6 reports the estimated seasonal or annual, regional range, mean and standard deviations of our  
 10 TOA DARE<sub>owc</sub> dataset (i.e., values of Fig. 7a)

Deleted: 7

Deleted: 9

11 **Table 6:** Estimated SW TOA DARE<sub>owc</sub> (W·m<sup>-2</sup>, setting is case IV of Table 4) in each region of Table  
 12 5.

Deleted: 7

Deleted: 5

Deleted: 6

Region	min, max	mean DJF	mean MAM	mean JJA	mean SON	mean ANN
NEPa	-0.57, 5.10	0.12±0.18	0.62±0.79	0.47±0.78	0.18±0.25	0.35 ± 0.50
SEPa	-0.21, 2.85	0.09±0.19	0.02±0.15	0.07±0.37	0.12±0.44	0.07 ± 0.29
TAt	-1.02, 5.25	0.26±0.43	0.31±0.43	1.08±1.66	0.01±0.42	0.41 ± 0.74
SEAt	0.20, 7.59	0.31±1.09	0.20±0.41	2.49±2.54	2.87±2.33	1.47 ± 1.59
InWA	-0.39, 0.83	0.04±0.16	-0.06±0.10	0.01±0.11	0.04±0.27	0.01 ± 0.16
NWPa	0.07, 5.72	0.11±0.14	1.98±1.85	1.01±1.65	0.68±0.46	0.95 ± 1.02

13  
 14 We record positive TOA DARE<sub>owc</sub> values above 1 W·m<sup>-2</sup> in Fig. 7a over TAt in JJA (1.08 ± 1.66),  
 15 SEAt in JJA and SON (2.49 ± 2.54 and 2.87 ± 2.33) and NWPa in MAM (1.98 ± 1.85). Let us note that  
 16 the highest positive TOA DARE<sub>owc</sub> values on Fig. 7a and in Table 6 may not be entirely representative  
 17 of each region, because they are based on a smaller number of valid DARE<sub>owc</sub> results (86% valid  
 18 values in JJA in TAt, 58-88% in JJA-SON in SEAt and 69% in MAM in NWPa). SEAt and NWPa are  
 19 the only regions showing an all-positive range of DARE<sub>owc</sub> values in Table 6 (i.e., respectively within

Deleted: 9

Deleted: 9

Deleted: 7

Deleted: 7

31 0.20 and 7.59 and within 0.07 and 5.72  $\text{W}\cdot\text{m}^{-2}$ ). The spread (i.e., standard deviation) on those mean  
32 regional  $\text{DARE}_{\text{OWC}}$  is of the same order of magnitude as the mean values themselves. For example,  
33 although TAt shows an annual mean  $\text{DARE}_{\text{OWC}}$  value of 0.41  $\text{W}\cdot\text{m}^{-2}$ , most points (i.e., about 68%,  
34 assuming a normal distribution of  $\text{DARE}_{\text{OWC}}$ ) are within  $0.41 \pm 0.74 \text{ W}\cdot\text{m}^{-2}$  (see Table 6). Those regions  
35 and seasons of highly positive  $\text{DARE}_{\text{OWC}}$  values are associated with the highest CALIOP  $\tau^{\text{DR}}_{\text{AAC}} \times f_{\text{AAC}}$   
36 values (see Fig. 7d: 0.12 in JJA in TAt, 0.12-0.13 in JJA-SON in SEAt and 0.10 in MAM in NWPa).  
37 They are also associated with lower SSA values (i.e.,  $< 0.94$  in Fig. 7e), typical of more light absorbing  
38 aerosols such as biomass burning. The underlying COD values are fairly constant (between  $\sim 5$ -10 on  
39 Fig. 7f), except for a noticeably higher COD over the NWPa region (between  $\sim 15$ -25 on Fig. 7f). NWPa  
40 is the region of highest latitudes in our study (i.e., between 40N and 55N). More variation in the COD at  
41 higher latitudes is also observed in Fig. A2 in the Appendix. This agrees with King et al. [2013], who  
42 show a larger zonal variation of COD (and increased uncertainty in the MODIS cloud property  
43 retrievals) in the higher latitudes of both hemispheres, particularly in winter (see their Fig. 12b).  
44 When computing mean  $\text{DARE}_{\text{OWC}}$  results within the “SE Atlantic” region defined in Zhang et al.  
45 [2016] (i.e., [30S, 10N; 20W, 20E] instead of [19S, 2N; 10W, 8E] in our study), we find a small  
46 fraction of valid pixels (i.e., an average of  $\sim 37\%$ ) but a mean annual  $\text{DARE}_{\text{OWC}}$  value of 0.57  $\text{W}\cdot\text{m}^{-2}$ ,  
47 which resides within their range of annual  $\text{DARE}_{\text{cloudy}}$  values (i.e., 0.1 to 0.68  $\text{W}\cdot\text{m}^{-2}$  in Zhang et al.  
48 [2016]). Similar to Matus et al. [2015], the season of highest  $\text{DARE}_{\text{OWC}}$  is SON over the SE Atlantic  
49 (they find 10% of  $\text{DARE}_{\text{OWC}}$  larger than 10  $\text{W}\cdot\text{m}^{-2}$  over thick clouds with  $\text{COD} > 1$ , see their Fig. 9d).  
50 However, our  $\text{DARE}_{\text{OWC}}$  results are significantly higher than the ones in Zhang et al. [2016] in our  
43

Deleted: 7

Deleted: 9

Deleted: 9

Deleted: 9

Deleted: 9

56 SEAt region (defined as a smaller region and offshore from the “SE Atlantic” region in Zhang et al.  
57 [2016]) as well as in the TAt (similar latitude/ longitude boundaries to the ones of region “TNE  
58 Atlantic” in Zhang et al. [2016]) and the NWPa (similar boundaries to “NW Pacific” in Zhang et al.  
59 [2016]) regions.

60 We emphasize that the DARE<sub>owc</sub> estimates in this study are not directly comparable to many previous  
61 studies (see Table 1) because of different spatial domain, period, satellite sensors and associated  
62 uncertainties. This will lead to the detection of different fractions of AAC above different types of  
63 clouds and different AAC types over the globe. The calculations of DARE<sub>cloudy</sub> can also differ greatly  
64 depending on different AAC aerosol radiative properties assumptions above clouds (especially  
65 absorption) and different assumptions in aerosol and cloud vertical heights (see Table 1).

66 Apart from the major differences in methods and sensors, it seems reasonable to say that we are missing  
67 AAC cases over pure dust-dominant regions such as the Arabian Sea or the TAt region (compared to  
68 e.g. Zhang et al. [2016] and Matus et al. [2015]). Both Matus et al. [2015] and Zhang et al. [2016] use  
69 the CALIOP Level 2 standard products to distinguish among a few aerosol types and infer specific  
70 aerosol optical properties in their DARE<sub>cloudy</sub>. According to Figure 1(d), SEAt, TAt and the Arabian Sea  
71 are regions where we might be missing up to 40% of AAC cases when using the DR technique  
72 compared to the CALIOP standard products. The number of potentially missing AAC cases in our study  
73 is larger over the Arabian sea ([0-30°N and 40-80°E] due to the limited number of OWCs suitable for  
74 the DR method (see section [B1](#) in the Appendix). Zhang et al. [2016] show that pure dust aerosols over  
75 these dust-dominant regions tend to produce a negative DARE<sub>cloudy</sub> when the underlying COD is below

Deleted: B3

77 ~7 and this is the case for most of the clouds over these regions in their study. In summary, two factors  
78 in the DR method seem to hamper the detection of AAC in these regions: the low cloud optical depths  
79 of underlying clouds and very few cases of “clear air” above clouds. As a consequence, we propose that  
80 the positive  $DARE_{OWC}$  values in our study should, in reality, be counter-balanced by more negative  
81 dust-driven  $DARE_{cloudy}$  values over regions such as TAt and the Arabian Sea. On the other hand, the  
82  $DARE_{cloudy}$  results from Matus et al. [2015] and Zhang et al. [2016] might also differ from the true  
83 global  $DARE_{cloudy}$  state of the planet for different reasons. As described in Matus et al. [2015], using  
84 CALIOP Level 2 standard products as in Matus et al. [2015] and Zhang et al. [2016] could lead to  
85 possible misclassification of dust aerosols as clouds [Omar et al., 2009], specifically around cloud edges  
86 in the TAt region. Moreover, even if the AAC is correctly detected in Matus et al. [2015] and Zhang et  
87 al. [2016], the amount of AAC AOD might be biased low due to their use of the CALIOP Level 2  
88 standard products [Kacenelenbogen et al., 2014].

#### 89 **4. Uncertainties in our DARE above cloud results and the path forward**

##### 90 **4.1. Detecting and quantifying the true amount of AAC cases**

91 Our study uses mainly CALIOP Level 1 measurements to detect aerosols above specific OWCs that  
92 satisfy the criteria given in Table B2. We suggest that the number of CALIOP profiles that contain  
93 aerosols over any type of cloud (instead of only OWCs in this study) should be informed by a  
94 combination of different techniques applied to CALIOP observations (e.g., the standard products, the  
95 DR and the CR technique). Airborne observations such as those from the ObseRvations of Aerosols

96 above Clouds and their intEractionS (ORACLES) field campaigns [Zuidema et al., 2016] are well  
97 suited for providing further guidance on when to apply which technique.

98 To the best of our knowledge, the true global occurrence of aerosols above any type of cloud remains  
99 unknown. This question cannot be entirely answered with the use of CALIOP observations only. We  
00 suggest that a more complete global quantification and characterization of aerosol above any type of  
01 cloud should be informed by a combination of AAC retrievals from CALIOP, passive satellite sensors  
02 (e.g. POLDER [Waquet et al., 2013a,b, Peers et al., 2015, Deaconu et al., 2017] and MODIS [Meyer et  
03 al., 2013, Zhang et al., 2014, 2016], see Table 2) and model simulations [Schulz et al., 2006].

#### 04 **4.2. Considering the diurnal variability of aerosol and cloud properties**

05 While we consider the diurnal cycle of solar zenith angles in our DARE<sub>cloudy</sub> calculations, we use  
06 MODIS for underlying COD and cloud  $R_e$  information as well as a combination of MODIS, OMI and  
07 CALIOP for overlying aerosol properties (see section 2.2). By using A-Train satellite observations (i.e.,  
08 the AQUA, AURA and CALIPSO platforms), with an overpass time of 1:30 PM local time at the  
09 Equator, we are only using a daily snapshot of cloud and aerosol properties and not considering their  
10 daily variability.

11 Min and Zhang [2014] show a strong diurnal cycle of cloud fraction over the SEAt region (i.e., a 5-year  
12 mean trend of diurnal cloud fraction using SEVIRI that varies from ~60% in the late afternoon to 80%  
13 in the early morning on their Fig. 4). According to Min and Zhang [2014] (see their Table 2), assuming  
14 a constant cloud fraction derived from MODIS/ AQUA generally leads to an underestimation (less  
15 positive) by ~16% in the DARE<sub>all-sky</sub> calculations (see Eq. 1). Further studies should explore the

16 implications of diurnal variations of COD and cloud  $R_e$  on  $DARE_{cloudy}$  results using, for example,  
17 geostationary observations from SEVIRI.

18 Daily variations of aerosol (intensive and extensive) radiative properties above clouds cannot be  
19 ignored either. Arola et al. [2013] and Kassaniov et al. [2013] both show that even when the AOD  
20 strongly varies during the day, the accurate prediction of 24h-average  $DARE_{non-cloudy}$  requires only daily  
21 averaged properties. However, in the case of under-sampled aerosol properties, such as when using A-  
22 Train derived aerosol properties (this study), the error in the 24h- $DARE_{non-cloudy}$  can be as large as 100%  
23 [Kassaniov et al., 2013]. Xu et al. [2016] show that the daily mean TOA  $DARE_{non-cloudy}$  is overestimated  
24 by up to  $3.9 \text{ W}\cdot\text{m}^{-2}$  in the summertime in Beijing if they use a constant MODIS/ AQUA AOD value,  
25 compared to accounting for the observed hourly-averaged daily variability. Kassaniov et al. [2013]  
26 propose that using a simple combination of MODIS TERRA and AQUA products would offer a  
27 reasonable assessment of the daily averaged aerosol properties for an improved estimation of 24h-  
28  $DARE_{non-cloudy}$ .

#### 29 **4.3. Considering the spatial and temporal variability of cloud and aerosol fields**

30 We have used coarse resolution (i.e.,  $4^\circ \times 5^\circ$ ) seasonally gridded aerosol and cloud properties in our  
31  $DARE_{owc}$  calculations (see section 2.2). As a consequence, sub-grid scale variability (or heterogeneity)  
32 of cloud and aerosol properties has not been considered. This approach is similar to assuming spatially  
33 and temporally homogeneous cloud and aerosol fields in our  $DARE_{owc}$  results.

34 Marine Boundary Layer (MBL) clouds show significant small-scale horizontal variability [Di Girolamo  
35 et al., 2010; Zhang et al., 2011]. Using mean gridded COD in  $DARE_{cloudy}$  calculations, for example, can

36 lead to significant biases in  $DARE_{cloudy}$  calculations, an effect called the “plane-parallel albedo bias”  
37 [e.g., Oreopoulos et al., 2007, Di Girolamo et al., 2010, Zhang et al., 2011, Zhang et al., 2012]. Min and  
38 Zhang [2014] show that using a mean gridded COD significantly overestimates (by ~10% over the  
39 SEAt region) the  $DARE_{cloudy}$  results when the cloud has significant sub-grid horizontal heterogeneity.  
40 Furthermore, this overestimation increases with increasing AOD, COD and cloud inhomogeneity.  
41 Future studies should examine the difference between  $DARE_{cloudy}$  results calculated with gridded mean  
42 COD and cloud  $R_e$  values (this study) and  $DARE_{cloudy}$  results calculated with MODIS Level-3 joint  
43 histograms of MODIS COD and cloud  $R_e$  (e.g., similar to Min and Zhang [2014]).

44 Aerosol spatial variation can be significant over relatively short distances of 10 to 100km, depending on  
45 the type of environment [Anderson et al., 2003; Kovacs, 2006; Santese et al., 2007; Shinozuka and  
46 Redemann, 2011; Schutgens et al., 2013]. Shinozuka and Redemann [2011] argue that only a few  
47 environments can be more heterogeneous than the Canadian phase of the ARCTAS (Arctic Research of  
48 the Composition of the Troposphere from Aircraft and Satellites) experiment where the air mass was  
49 subject to fresh local biomass emissions. In this type of environment, they observed a 19% variability of  
50 the AOD over a 20 km length (comparable in scale to a  $\sim 0.1^\circ \times 0.1^\circ$  area). They also found a 2%  
51 variability in the AOD over the same length in a contrasting homogeneous environment that occurred  
52 after a long-range aerosol transport event. As a consequence, similar to using a mean gridded  
53 underlying COD and cloud  $R_e$ , using mean gridded overlying aerosol radiative properties could very  
54 well bias our  $DARE_{OWC}$  results.

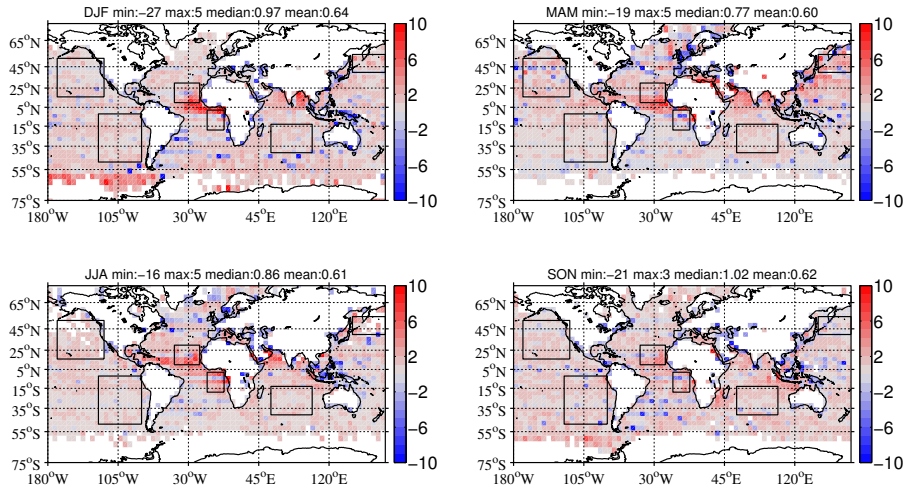
55 As a preliminary investigation into the sources and magnitudes of these potential biases, we have used  
56 TOA  $DARE_{non-cloudy}$  (see Eq. 1) estimates derived using well-located aerosol properties (hereafter  
57 called “retrieve-then-average” or R-A) from a companion study (Redemann et al. [2019]; see section A  
58 of the appendix) and compared those to  $DARE_{non-cloudy}$  estimates computed using seasonally gridded  
59 mean aerosol properties at seasonally gridded mean vertical heights (hereafter called “average-then-  
60 retrieve” or A-R). Both  $DARE_{non-cloudy}$  results obtained with the two methods are compared over ocean  
61 and at a resolution of  $4^{\circ} \times 5^{\circ}$ .

62 A majority (i.e., ~58%) of A-R  $DARE_{non-cloudy}$  results are within  $\pm 35\%$  of the R-A  $DARE_{non-cloudy}$   
63 results. We find very few (i.e., ~1%) negative R-A  $DARE_{non-cloudy}$  values paired with positive A-R  
64  $DARE_{non-cloudy}$  values and very few large differences between both methods (i.e., less than 1% of the  
65 differences are above  $\pm 10 W m^{-2}$ ). However, we find a weak agreement between A-R and R-A  
66  $DARE_{non-cloudy}$  values during each of the seasons (i.e., a correlation coefficient between 0.21 and 0.34).  
67 The A-R  $DARE_{non-cloudy}$  values are generally biased high relative to the R-A calculations, as illustrated  
68 by positive mean and median values of the A-R to R-A differences (respectively  $0.64 W m^{-2}$  and  $0.92$   
69  $W m^{-2}$ ; standard deviation of 2.25). When computing the global seasonal mean A-R and R-A  $DARE_{non-}$   
70  $cloudy$  values separately, we find that the global seasonal A-R  $DARE_{non-cloudy}$  values overestimate the  
71 global seasonal R-A  $DARE_{non-cloudy}$  values by 17%, 19%, 21%, and 17% in DJF, MAM, JJA and SON.  
72 Moreover, the seasonal median A-R  $DARE_{non-cloudy}$  values overestimate the seasonal median R-A  
73  $DARE_{non-cloudy}$  values in all six regions of Table 5 (i.e., median differences between  $0.28 W m^{-2}$  in  
74 NWPa in SON and  $3.05 W m^{-2}$  in SEAt in JJA). The geospatial distributions of these differences in  
75 DARE calculation strategies are illustrated in Figure 8.

Deleted: 2018

Deleted: 6

Deleted: 10



80

81

82 **Figure 8:** Seasonal maps showing the differences in SW TOA DARE<sub>non-cloudy</sub> computed using the  
 83 average-then-retrieve (A-R) and the retrieve-then-average (R-A) strategies. Positive values (in red)  
 84 show regions where the A-R DARE calculations are larger, whereas negative values (in blue) show  
 85 regions where the R-A DARE calculations are larger. The squares show different regions defined in  
 86 Table 5. The title of each map shows the global minimum, maximum, median and mean values.

Deleted: 10

87

88 **4.4. Assuming similar intensive aerosol properties above clouds and in near-by cloud-**  
 89 **free skies**

Deleted: 6

92 In the calculation of  $DARE_{owc}$ , we assume similar intensive aerosol properties above clouds and in  
93 near-by clear skies. This assumption might not be valid and should be investigated in future studies by  
94 comparing aerosol properties and their probability distributions over clear and cloudy conditions using  
95 observations from the ORACLES field campaign.

#### 96 4.5. Assuming fixed aerosol and cloud vertical layers

97 Finally, Long Wave (LW) radiative forcing is particularly dependent on the vertical distribution of  
98 aerosols, especially for light absorbing aerosols [Chin et al., 2009]. This is because the energy these  
99 aerosols reradiate depends on the temperature, and hence their altitude. For example, Penner et al.  
00 [2003] emphasize the importance of soot and smoke aerosol injection height in LW TOA  $DARE_{all-sky}$   
01 (see Eq. 1) simulations (higher injection heights tend to enhance the negative LW radiative forcing).

02  
03 Quijano et al. [2000], Chung et al. [2005] and Chin et al. [2009] demonstrate the importance of an  
04 aerosol height, in relation to a cloud height (i.e., the aerosols located above, within or below the clouds)  
05 in an accurate estimation of SW TOA  $DARE_{all-sky}$ . Chung et al. [2005], for example, show that varying  
06 the relative vertical distribution of aerosols and clouds leads to a range of global anthropogenic SW  
07 TOA  $DARE_{all-sky}$  from  $-0.1$  to  $-0.6 \text{ W}\cdot\text{m}^{-2}$  (using a combination of MODIS satellite, AERONET ground-  
08 based observations and CTM simulations, see their Table 2).

09  
10 However, here, we concentrate on cases of aerosol layers overlying clouds in order to compute SW  
11 TOA  $DARE_{cloudy}$ . Aerosol and cloud layer heights are assumed constant over the globe in our study (see

Formatted: Font: 12 pt  
Formatted: Justified, Line spacing: Double

Formatted: Font: 12 pt

Formatted: Font: 12 pt

Formatted: Font: 12 pt

Formatted: Font: 12 pt

Formatted: Font: Font color: Auto

Formatted: Font: 12 pt, Not Highlight

Formatted: Not Highlight

Formatted: Font: 12 pt, Not Highlight

Formatted: Not Highlight

Formatted: Font: 12 pt, Not Highlight

Formatted: Not Highlight

Formatted: Font: 12 pt, Not Highlight

Formatted: Not Highlight

Formatted: Font: 12 pt, Not Highlight

Formatted: Font: 12 pt, Subscript, Not Highlight

Formatted: Font: 12 pt, Not Highlight

Formatted: Not Highlight

12 section 2.2). Future studies should incorporate mean gridded (i.e., 4°x5° in this study)-seasonal CALIOP  
13 Level 2 aerosol and cloud vertical profiles into the calculation of DARE<sub>OWC</sub>.

14 However, constraining clouds between 2 and 3km in our study does not seem unreasonable as our AAC  
15 AOD calculations using the DR method can only be applied to aerosols overlying specific low opaque  
16 water clouds with, among other criteria, an altitude below 3km (see Table B2). On the other hand,  
17 constraining aerosols between 3 and 4km in our study is not realistic over many parts of the globe (e.g.,  
18 see Fig. 7 of Devasthale et al. [2011]). For example, over the region of South East Atlantic during the  
19 ORACLES campaign, the HSRL team observed an aerosol layer located in average between 2 and 5km,  
20 and overlying a cloud at an average altitude of 1.2km.

21  
22 According to Zarzycki et al. [2010], the underlying cloud properties are orders of magnitude more  
23 crucial to the computation of DARE<sub>cloudy</sub> than the location of the aerosol layer relative to the cloud, as  
24 long as the aerosol is above the cloud. In other words, the forcing does not seem to depend on the height  
25 of the aerosols above clouds as much as other parameters such as the AOD, SSA or cloud albedo.  
26 Zarzycki et al. [2010] investigated this assumption and found that over low and middle clouds, forcing  
27 changed by ~1-3% through the heights where the Black Carbon burden was the largest. These small  
28 changes in forcing are likely products of a change in atmospheric transmission above the aerosol layer  
29 [Haywood and Ramaswamy, 1998] (e.g., a change in the aerosol height is linked to a change in the  
30 integrated column water vapor above the aerosol layer and this, in turn, would alter the incident solar  
31 radiation).

Formatted: Line spacing: Double

Formatted: Justified, Line spacing: Double

Formatted: Font: 12 pt, Not Highlight

Formatted: Normal

Formatted: Font: 12 pt, Subscript, Not Highlight

Formatted: Font: 12 pt, Not Highlight

Formatted: Space Before: 0 pt, After: 0 pt, Line spacing: Double

## 5. Conclusions

We have computed a first approximation of global seasonal TOA short wave Direct Aerosol Radiative Effects (DARE) above Opaque Water Clouds (OWCs),  $DARE_{OWC}$ , using observation-based aerosol and cloud radiative properties from a combination of A-Train satellite sensors and a radiative transfer model. Our  $DARE_{OWC}$  calculations make three major departures from previous peer-reviewed results: (1) they use extensive aerosol properties derived from the Depolarization Ratio, DR, method applied to Level 1 CALIOP measurements, whereas previous studies often use CALIOP Level 2 standard products which introduce higher uncertainties and known biases; (2) our  $DARE_{OWC}$  calculations are applied globally, while most previous studies focus on specific regions of high AAC occurrence such as the SE Atlantic; and (3) our calculations use intensive aerosol properties retrieved from a combination of A-Train satellite sensor measurements (e.g., MODIS, OMI and CALIOP).

Our study agrees with previous findings on the locations and seasons of the maximum occurrence of AAC over the globe. We identify six regions of high AAC occurrence (i.e., AAC hotspots): South and North East Pacific (SEAt and NEPa), Tropical and South East Atlantic (TAt and SEAt), Indian Ocean offshore from West Australia (InWA) and North West Pacific (NWPa). We define  $\tau^{DR}_{AAC}$ , the Aerosol Optical Depth (AOD) above OWCs using the DR method on CALIOP measurements,  $f_{AAC}$ , and the frequency of occurrence of AAC cases. We record a majority of  $\tau^{DR}_{AAC} \times f_{AAC}$  values at 532nm in the 0.01-0.02 range and that can exceed 0.2 over a few AAC hotspots.

We find positive averages of global seasonal  $DARE_{OWC}$  between 0.13 and 0.26  $W \cdot m^{-2}$  and an annual global mean  $DARE_{OWC}$  value of 0.20  $W \cdot m^{-2}$  (i.e., a warming effect on climate). Regional seasonal

**Deleted:** Finally, aerosol and cloud layer heights are assumed constant over the globe in our study (see section 2.2). Matus et al. [2015] state that estimates of  $DARE_{cloud}$  over SEAt are highly sensitive to the relative vertical distribution of cloud and aerosols. Quijano et al. [2000], Penner et al. [2003] and Chung et al. [2005] demonstrate the importance of the vertical distributions of cloud and aerosol layers in an accurate estimate of radiative fluxes. Chung et al. [2005], for example, show that varying the relative vertical distribution of aerosols and clouds leads to a range of global modeled anthropogenic TOA  $DARE_{all-sky}$  (see Eq. 1) from -0.1 to -0.6  $W \cdot m^{-2}$  (see their Table 2). Future studies should incorporate mean gridded (i.e.,  $4^{\circ} \times 5^{\circ}$  in this study)-seasonal CALIOP Level 2 aerosol and cloud vertical profiles into the calculation of  $DARE_{OWC}$ .

**Deleted:** and,  $S_{AAC}$ , the extinction-to-backscatter (lidar) ratio above OWCs

**Deleted:** The majority of the  $S_{AAC}$  values lie in the 40 – 50 sr range, which is typical of dust aerosols.  $S_{AAC}$  is also consistent with typical dominant aerosol types over the TAt and SEAt regions (respectively dust and biomass burning).

72 DARE<sub>owc</sub> values range from  $-0.06 \text{ W}\cdot\text{m}^{-2}$  in the Indian Ocean, offshore from western Australia (in  
73 March-April-May) to  $2.87 \text{ W}\cdot\text{m}^{-2}$  in the South East Atlantic (in September-October-November). High  
74 positive values are usually paired with high aerosol optical depths ( $>0.1$ ) and low single scattering  
75 albedos ( $<0.94$ ), representative of e.g. biomass burning aerosols.

76 Although the DARE<sub>owc</sub> estimates in this study are not directly comparable to previous studies because  
77 of different spatial domain, period, satellite sensors, detection methods, and/ or associated uncertainties,  
78 we emphasize that they are notably higher than the ones from [Zhang et al., 2016; Matus et al., 2015  
79 and Oikawa et al., 2013]. In addition to differences in satellite sensors, AAC detection methods, and  
80 the assumptions enforced in the calculation of DARE<sub>cloudy</sub>, there are several other factors that may  
81 contribute to the overall higher DARE<sub>owc</sub> values we report in this study. The most likely contributors  
82 are (1) a possible underestimate of the number of dust-dominated AAC cases; (2) our use of the DR  
83 method on CALIOP Level 1 data to quantify the AAC AOD; and, in particular, (3) the technique we  
84 have chosen for aggregating sub-grid aerosol and cloud spatial and temporal variability. We discuss  
85 each of these in turn in the following paragraphs.

86 Two factors seem to be preventing the DR method from recording enough AAC cases in these regions:  
87 the low cloud optical depths of underlying clouds and very few cases of “clear air” above clouds. The  
88 DR method used in this study is restricted to aerosols above OWCs that satisfy a long list of criteria.  
89 The AAC dataset in this study underestimates (i) the total number of CALIOP 5 km profiles that  
90 contain AAC over all OWCs (i.e., not just suitable to the DR technique), (ii) the total number of  
91 CALIOP 5 km profiles that contain AAC over any type of clouds over the globe and (iii) the true global

92 occurrence of AAC over any type of clouds. To the best of our knowledge, the true amount of AAC in  
93 (i), (ii) and (iii) remains unknown. A better characterization of the “unobstructed” OWCs in the  
94 application of the DR technique on CALIOP measurements might bring us closer to answering (i). A  
95 combination of CALIOP standard, DR and CR techniques together with airborne observations (e.g.,  
96 from the ORACLES field campaign) might answer (ii). Finally, (iii) cannot be answered with the only  
97 use of CALIOP observations. The results in this study should be combined with aerosol-above-cloud  
98 retrievals from passive satellite sensors (e.g. POLDER [Waquet et al., 2013a,b, Peers et al., 2015,  
99 Deaconu et al., 2017] or MODIS [Meyer et al., 2013, Zhang et al., 2014, 2016]) and model simulations  
00 [Schulz et al., 2006] to obtain a more complete global quantification and characterization of aerosol  
01 above any type of clouds.

02 Compared to other methods, the DR technique applied to CALIOP measurements retrieves  $\tau^{\text{DR}}_{\text{AAC}}$  with  
03 fewer assumptions and lower uncertainties. Other global  $\text{DARE}_{\text{cloudy}}$  results (e.g., Matus et al. [2015]  
04 and Zhang et al. [2016]) use CALIOP standard products to detect the AAC cases, quantify the AAC  
05 AOD and define the aerosol type (and specify the aerosol intensive properties). These studies rely on  
06 the presence of aerosol in concentrations sufficient to be identified by the CALIOP layer detection  
07 scheme, and on the ability of the CALIOP aerosol subtyping algorithm to correctly identify the aerosol  
08 type and thus select the correct lidar ratio for the AOD retrieval. While several recent studies have  
09 taken various approaches to quantifying the amount of aerosol currently being undetected in the  
10 CALIOP backscatter signals, their general conclusions are unanimous. The CALIOP standard products  
11 underestimate above-cloud aerosol loading and the corresponding AAC AOD (Kacenelenbogen et al.,

12 2014; Kim et al., 2017; Toth et al., 2018; Watson-Parris et al., 2018), and this in turn leads to  
13 underestimates of both  $DARE_{\text{non-cloudy}}$  and  $DARE_{\text{cloudy}}$  (Thorsen and Fu, 2015; Thorsen et al., 2017).

14 In this study, we have assumed spatially and temporally homogeneous clouds and aerosols in our  
15  $DARE_{\text{owc}}$  calculations. As a preliminary investigation of such effects on our calculations, we have  
16 compared DARE calculations derived from well collocated aerosol properties (retrieve-then-average) to  
17 DARE calculations using seasonally gridded mean aerosol properties (average-then-retrieve). We have  
18 shown that the average-then-compute DARE results generally overestimate the retrieve-then-average  
19 results both on a global scale and in each of our selected regions. Further research and analysis are  
20 required to determine which of these two computational approaches provides the most accurate  
21 estimates of real-world DARE.

22

23 **Appendix A: Method to obtain aerosol radiative properties in non-cloudy (i.e., clear-sky)**  
24 **conditions using MODIS, OMI and CALIOP and to estimate  $DARE_{non-cloudy}$**

25

26 A companion paper, Redemann et al. [2019], develops and refines a method for retrieving full spectral  
27 (i.e., at 30 different wavelengths) extinction coefficients, Single Scattering Albedo (SSA) and  
28 asymmetry parameters from satellite aerosol products in non-cloudy (i.e., clear-sky) conditions. The  
29 method requires collocation of quality-screened satellite data, selection of aerosol models that reproduce  
30 the satellite observations within stated uncertainties, and forward calculation of aerosol radiative  
31 properties based on the selected aerosol models. They use MODIS-Aqua AOD at 550 and 1240 nm,  
32 CALIPSO integrated backscattering (IBS) at 532 nm and OMI Absorption Aerosol Optical Depth  
33 (AAOD) at 388 nm (see Table A1). The aerosol radiative properties resulting from this method are  
34 called MOC retrievals (for MODIS-OMI-CALIOP).

35

Deleted: 2018

37

38 Table A1. Data sets currently used for global MODIS-OMI-CALIOP (MOC) retrievals of aerosol  
39 radiative properties [Redemann et al., 2019]; DT: Dark Target and EDB: Enhanced Deep Blue.

Deleted: 2018

Product	Source	Assumed Uncertainties*	Weight**,**
550 nm AOD	MODIS Collection 6 (Ocean, DT-Land, EDB-Land)	$\pm 5\% \pm 30 \text{ Mm}^{-1}$	0.1488
1240 nm AOD	MODIS Collection 6 (extrapolated spectrally over land)	$\pm 5\% \pm 30 \text{ Mm}^{-1}$	0.1422
388 nm AAOD	OMI (OMAERO for ocean, OMAERUV for DT-land), MODIS EDB	$\pm 30\% \pm 50 \text{ Mm}^{-1}$	0.5542
532 nm IBS	CALIPSO V3-01	$\pm 30\% \pm 0.1 \text{ Mm}^{-1} \text{sr}^{-1}$	0.1548

40 \* For the values after division by CALIPSO layer depth

41 \*\* The weight,  $w_i$ , is used to calculate the cost function  $X = (\sum w_i ((x_i - \hat{x}_i) / \delta \hat{x}_i)^2)^{1/2}$  where  $x_i$  are the retrieved parameters,

42  $\hat{x}_i$  are the observables,  $\delta \hat{x}_i$  are the uncertainties in the observables.

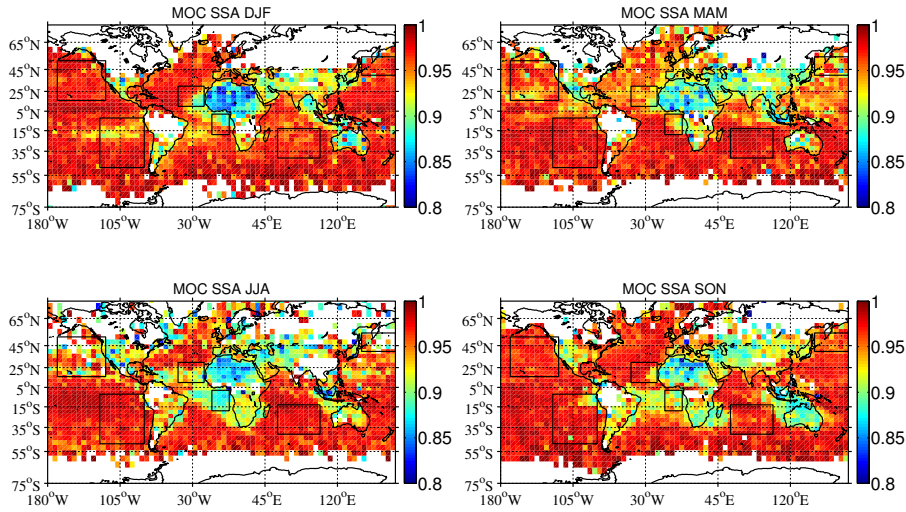
43 The choice of OMI satellite algorithms (see Table A1) reflects their assessment of the  
44 representativeness of subsampling OMI data along the CALIPSO track; i.e., they compared the  
45 probability distribution (PDF) of the OMI retrievals along the CALIPSO track to the global PDF and  
46 chose the data set that had the best match between global and along-track PDF for the over-ocean and  
47 two over-land data sets, the latter being different in their use of MODIS dark target (DT) versus  
48 enhanced Deep-Blue (EDB) data as the source of AOD. They collocate the MODIS and OMI products  
49 within a 40x40 km<sup>2</sup> box centered at each CALIPSO 5-km profile location after Redemann et al. [2012].

51 For the OMAERUV data set, they choose the SSA product for the layer height indicated by the  
52 collocated CALIOP backscatter profile.

53 Their aerosol models emulate those of the MODIS aerosol over-ocean algorithm [Remer et al., 2005].  
54 Like the MODIS algorithm, they define each model with a lognormal size distribution and wavelength-  
55 dependent refractive index. They then combine two of these models, weighted by their number  
56 concentration, and compute optical properties for the bi-modal lognormal size distribution. Unlike the  
57 MODIS algorithm, they allow combinations of two fine-mode or two coarse-mode models. They use  
58 ten different aerosol models, which stem from some of the MODIS over-ocean models [Remer et al.,  
59 2005] but include more absorbing models, which was motivated by application of their methodology to  
60 the Arctic Research of the Composition of the Troposphere from Aircraft and Satellites (ARCTAS)  
61 field campaign data, requiring more aerosol absorption than included in the current MODIS over-ocean  
62 aerosol models. They use MOC spectral aerosol radiative properties to then calculate Direct Aerosol  
63 Radiative Effects (i.e.,  $DARE_{non-cloudy}$ , see Eq. 1) through a delta-four stream radiative transfer model  
64 with fifteen spectral bands from 0.175 to 4.0  $\mu\text{m}$  in SW and twelve longwave (LW) spectral bands  
65 between 2850 and  $0\text{ cm}^{-1}$  [Fu and Liou, 1992].

66 In order to use these MOC parameters (retrieved in clear-skies) in our  $DARE_{owc}$  calculations, we need  
67 to assume similar aerosol intensive properties in clear skies compared to above clouds and we need to  
68 spatially and/ or temporally grid these MOC parameters. As discussed in section 2.2, we use seasonally  
69 averaged MOC spectral SSA, aerosol asymmetry parameter, and extinction retrievals on  $4^\circ \times 5^\circ$  grids.  
70 Figure A1 illustrates seasonal maps of MOC SSA used in our calculations of  $DARE_{owc}$ .

71



72

73 Figure A1: Seasonal maps of MOC SSA at 546.3 nm in 2007 used in the calculations of DARE<sub>owc</sub>.

74 The squares show different regions defined in Table 5.

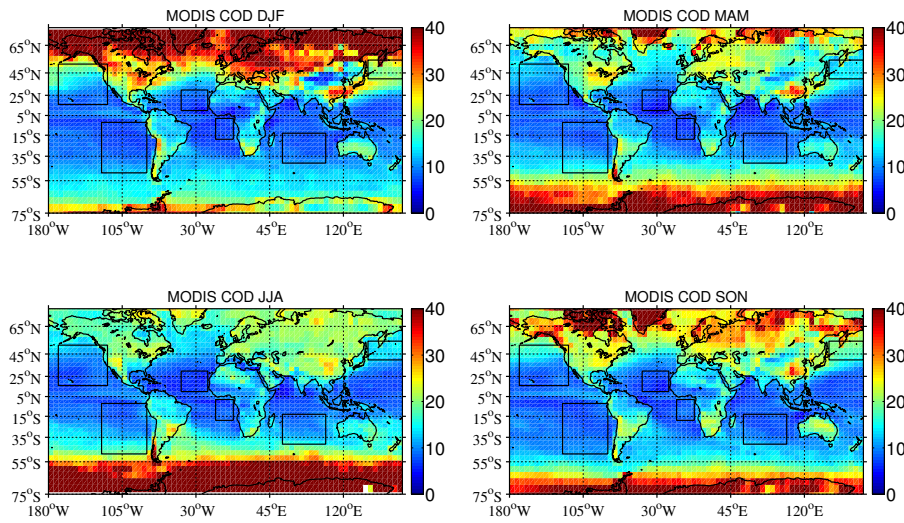
Deleted: 6

75

76 The DARE<sub>owc</sub> calculations in our study also require information about the underlying cloud optical  
77 properties. As discussed in section 2.2, we use seasonally mean gridded COD from MODIS such as  
78 illustrated in Figure A2.

79

60



81  
 82 Figure A2: Seasonal maps of COD used in the calculations of  $DARE_{OWC}$ . COD information is inferred  
 83 from MODIS seasonally averaged monthly  $1^\circ \times 1^\circ$  grids (i.e. liquid water cloud products of MYD08\_M3:  
 84 “Cloud Effective Radius Liquid Mean Mean” and “Cloud Optical Thickness Liquid Mean Mean”  
 85 [Platnick et al. 2015]) from 2008 to 2012. The squares show different regions defined in Table 5.

86  
 87 **Appendix B: Method for AAC detection and AAC AOD computation**

88 The depolarization ratio (DR) method [Hu et al., 2007b] used to derive estimates of the optical depths  
 89 ( $\tau$ ) of aerosols above clouds (AAC) is given in Eq. (2) and repeated here for convenience:

90 
$$\tau_{AAC}^{DR} = -0.5 \times \ln[IAB_{SS,AAC}^{OWC} / IAB_{SS,CAC}^{OWC}] \quad (B1)$$

Deleted: 6

Deleted: .

Deleted: and  $S_{AAC}$

94 The subscripts SS and CAC represent, respectively, ‘single scattering’ and ‘clear above clouds’.  
 95  $IAB^{OWC}_{SS}$  (i.e., either  $IAB^{OWC}_{SS,AAC}$  or  $IAB^{OWC}_{SS,CAC}$ ) is the single scattering integrated attenuated  
 96 backscatter (IAB), derived from the product of the measured 532 nm attenuated backscatter coefficients  
 97 integrated from cloud top to cloud base,  $IAB^{OWC}$ , and a layer effective multiple scattering factor,  $\eta^{OWC}$ ,  
 98 derived from the layer-integrated volume depolarization ratio of the water cloud (called  $\delta^{OWC}$ ) using:

$$99 \quad \eta^{OWC} = [(1-\delta^{OWC})/(1+\delta^{OWC})]^2 \quad (B2)$$

00 [Hu et al., 2007a]. The single scattering IAB is thus derived using:

$$01 \quad IAB^{OWC}_{SS,X} = \eta^{OWC} \times IAB^{OWC}_{measured,X} \quad (B3)$$

02 for both aerosol above cloud cases ( $X = AAC$ ) and those cases with clear skies above ( $X = CAC$ ). An  
 03 assumption of the DR method is that  $\delta^{OWC}$  is negligibly affected by any aerosols that lie in the optical  
 04 path between the OWC and the lidar.

05 Table B1 provides a high-level overview of the procedure we use to compute aerosol optical depth  
 06 ( $\tau^{DR}_{AAC}$ ) above OWCs over the globe. We chose to concentrate on night-time CALIOP observations  
 07 only, as they have substantially higher signal-to-noise ratios (SNR) than the daytime measurements  
 08 [Hunt et al., 2009].

09

10 **Table B1:** Steps required to compute  $\tau^{DR}_{AAC}$  (\*): we construct global maps of  $4 \times 5^\circ$  pixels using  
 11 median values. Superscripts 1 and 2 denote respectively CALIOP Level 1 and Level 2 aerosol or cloud  
 12 layer products.

Deleted: and aerosol extinction-to-backscatter ratio ( $S_{AAC}$ )

Deleted: and  $S_{AAC}$

Step	Description	CALIOP, GEOS-5 and other computed products that are used in each step	More detail
S1	Select specific Opaque Water Clouds (OWC) suitable for the DR technique	CAD Score <sup>2</sup> , Integrated Attenuated Backscatter Uncertainty <sup>2</sup> , Integrated Volume Depolarization Ratio Uncertainty <sup>2</sup> , Horizontal Averaging, Opacity Flag <sup>2</sup> , Feature Classification Flags <sup>2</sup> , Layer Top Altitude <sup>2</sup> , Layer Top Temperature <sup>2</sup> , Surface Wind Speed <sup>2</sup>	section B1, Table B2
S2	Select a subset of OWCs from (S1) with clear air above	Overlying Integrated Attenuated Backscatter <sup>532</sup> , simulated molecular layer-integrated attenuated backscatter [Powell et al., 2002 and 2006] and OWCs from (S1)	section B2
S3	Process seasonal maps of median $IAB_{SS,CAC}^{OWC}$ and record number of $IAB_{SS,CAC}^{OWC}$ values per grid cell <sup>(*)</sup>	Integrated Attenuated Backscatter <sup>532</sup> , Integrated Volume Depolarization Ratio <sup>2</sup> , and OWCs with clear air above from (S2)	section B3
S4	Compute $\tau_{AAC}^{DR}$ along track	Total Attenuated Backscatter <sup>532</sup> , Molecular Number Density <sup>1</sup> , Ozone Number Density <sup>1</sup> Integrated Attenuated Backscatter <sup>532</sup> , Integrated Volume Depolarization Ratio <sup>2,+</sup> , Layer Top Altitude <sup>2,+</sup> , Layer Base Altitude <sup>2,+</sup> and seasonal maps of $IAB_{SS,CAC}^{OWC}$ from (S3) Note: (*) these parameters are re-computed from CALIOP level 1 data, and may differ from the standard CALIOP products	Eq. (2) or Eq. (B1)
S5	Process seasonal maps of median $\tau_{AAC}^{DR}$ and record number of $\tau_{AAC}^{DR}$ values per grid cell <sup>(*)</sup>	$\tau_{AAC}^{DR}$ of (S4) and we filter using number of $IAB_{SS,CAC}^{OWC}$ values per grid cell and per season from (S3)	Results in section 3.2

- Deleted: , SAAC from (S5)
- Deleted: and SAAC
- Deleted: S6
- Deleted: and SAAC

15

16 The first step (S1) is to identify OWCs that are suitable for the application of the DR method. The

17 acceptance criteria used to identify these clouds are described below in section B1 and listed in Table

18 B2. In the second step (S2), we use the overlying integrated attenuated backscatter (i.e., the 532 nm

23 attenuated backscatter coefficients integrated from TOA to the OWC cloud tops) to partition the OWC  
24 into two classes: (i) “unobstructed” clouds, for which the magnitude of the overlying IAB suggests that  
25 only aerosol-free clear skies lie above; and (ii) “obstructed” clouds for which we expect to be able to  
26 retrieve positive estimates of  $\tau_{AAC}^{DR}$ . Section B2 describes the objective method we have developed to  
27 separate unobstructed clouds (for which we can compute  $IAB_{SS,CAC}^{OWC}$ ) from obstructed clouds (for  
28 which we calculate  $IAB_{SS,AAC}^{OWC}$ ).

29 In step (S3), we construct global seasonal maps of median  $IAB_{SS,CAC}^{OWC}$  using 5 consecutive years  
30 (2008-2012) of CALIOP nighttime data (see section B3). By doing this we can subsequently compute  
31 estimates of  $\tau_{AAC}^{DR}$  without invoking assumptions about the lidar ratios of water clouds in clear skies  
32 [Hu et al., 2007]. Throughout this study, we chose to compute global median values within each grid  
33 cell (instead of mean values) to limit the impact of particularly high or low outliers on our statistics.

34 In step (S4), we compute estimates of  $\tau_{AAC}^{DR}$  for all obstructed OWC within each grid cell using Eq. (2)  
35 or Eq. (B1) and the 5-year nighttime seasonal median values of  $IAB_{SS,CAC}^{OWC}$  from (S3) (i.e., each  
36  $\tau_{AAC}^{DR}$  value along the CALIOP track is computed using one median value of  $IAB_{SS,CAC}^{OWC}$  per  $4^\circ \times 5^\circ$   
37 pixel and per season).

38 For the OWCs considered in this study, true layer base cannot be measured by CALIOP, simply  
39 because the signal becomes totally attenuated at some point below the layer top. Instead, what is  
40 reported in the CALIOP data products is an apparent base, which indicates the point at which the signal  
41 was essentially indistinguishable from background levels. Numerous validation studies have established  
42 the accuracy of the CALIOP cloud layer detection scheme (e.g., McGill et al., 2007; Kim et al., 2011;

43 Thorsen et al., 2011; Yorks et al., 2011; Candlish et al., 2013). Strong attenuation of the signal by  
 44 optically thick aerosols above an OWC can, in some cases, introduce biases into the cloud height  
 45 determination, which would lead to misestimates of  $IAB^{OWC}_{SS,AAC}$  and subsequent errors in  $\tau^{DR}_{AAC}$ . To  
 46 ensure the use of consistent data processing assumptions throughout our retrievals of  $\tau^{DR}_{AAC}$ , we  
 47 recalculated the components of  $IAB^{OWC}_{SS,AAC}$  (i.e., the “Integrated Attenuated Backscatter 532” and  
 48 “Integrated Volume Depolarization Ratio”) using parameters in the CALIOP Level 1 product (“Total  
 49 Attenuated Backscatter 532”, “Molecular Number Density” and “Ozone Number\_Density”) and  
 50 optimized estimates of cloud top and base altitudes based on the “Layer Top Altitude” and “Layer Base  
 51 Altitude” values reported in the CALIOP Level 2 layer product.

52 Apart from the identification of specific OWCs in step (S1), the primary Level 2 CALIOP parameters  
 53 used to calculate  $\tau^{DR}_{AAC}$  (S2-S4 in Table B1) are (i) the integrated attenuated backscatter above cloud  
 54 top to detect “clear air” cases (i.e. “Overlying Integrated Attenuated Backscatter 532” in step (S2)), (ii)  
 55 the layer integrated attenuated backscatter of the OWC with clear air above (i.e. “Integrated Attenuated  
 56 Backscatter 532” in step (S3)) and (iii) the cloud multiple scattering factor, derived as a function of the  
 57 layer integrated volume depolarization ratio (i.e. the “Integrated Volume Depolarization Ratio” in S3  
 58 and S4).

59 Below, we list the potential sources of errors associated with those three products:

- 60 (a) the accuracy of the 532 nm channel calibrations,
- 61 (b) the signal-to-noise ratio (SNR) of the backscatter data within the layer,
- 62 (c) the estimation of molecular scattering in the integrated attenuated backscatter (section 3.2.9.1 of the

Deleted: and  $S_{AAC}$

Deleted: In step (S5), we compute the  $S_{AAC}$  above OWC by solving the two-component lidar equation given by Eq. (15) of Fernald et al. [1972], and (following Young et al., 2018) reproduced below as Eq. (B4):

$$= \dots \dots \dots (B4)$$

$T^2_{AAC}(0,r)$  is the two-way aerosol two-way transmittance between the lidar (at range = 0) and range  $r$ . In our application,  $r_{top}$  is the range bin immediately above the OWC top altitude, so that  $T^2_{AAC}(0,r_{top}) = \exp(-2\chi\tau^{DR}_{AAC})$ .  $T_m(0,r)$  is the one-way transmittance due to molecular scattering and ozone absorption,  $S_m$  is the molecular extinction-to-backscatter ratio,  $\beta'(r)$  is the attenuated backscatter coefficient at range  $r$ , i.e.,

$$\beta'(r) = (\beta'_m(r) + \beta'_{AAC}(r)) \times T^2_m(0,r) \times T^2_{AAC}(0,r) \dots \dots \dots (B5)$$

[Young and Vaughan, 2009]. Because the regions studied typically have very low aerosol loading, molecular scattering often contributes most of the signal hence the two-component lidar equation is required. Moreover, because equation (B4) is transcendental and cannot be solved algebraically, solutions are obtained using an iterative method. Valid  $S_{AAC}$  values must satisfy  $\tau^{DR}_{AAC} > 0$  and  $S_{AAC} > 0$ , and the iteration must converge to a solution for which the relative difference between successive  $\tau^{DR}_{AAC}$  estimates is less than 0.01 (i.e.  $|(\tau^{DR}_{AAC} - \tau^{Fernald}_{AAC}) / \tau^{DR}_{AAC}| < 0.01$ ).

87 CALIPSO Feature Detection ATBD, [http://www-calipso.larc.nasa.gov/resources/pdfs/PC-SCI-](http://www-calipso.larc.nasa.gov/resources/pdfs/PC-SCI-202_Part2_rev1x01.pdf)  
88 [202\\_Part2\\_rev1x01.pdf](http://www-calipso.larc.nasa.gov/resources/pdfs/PC-SCI-202_Part2_rev1x01.pdf)), and

89 (d) the accuracy of the depolarization calibration (see section 5 in Powell et al., [2009]).

90 Concerning (a), Rogers et al. [2011] show that the NASA LaRC HSRL and CALIOP Version 3 532 nm  
91 total attenuated backscatter agree on average within ~3%, demonstrating the accuracy of the CALIOP  
92 532 nm calibration algorithms.

93 Concerning (b), we assume the influence of the SNR returned from the OWC is negligible as the OWCs  
94 are strongly scattering features and our dataset is composed of nighttime data only. However, the  
95 backscatter from tenuous and spatially diffuse aerosol layers with large extinction-to-backscatter ratios  
96 can lie well beneath the CALIOP attenuated backscatter detection threshold. When such layers lie  
97 above OWCs, the measured overlying integrated attenuated backscatter can fall within one standard  
98 deviation of the expected 'purely molecular' value that is used to identify CAC (or "unobstructed")  
99 OWC in our dataset (S2; see Sect. B2). Within the context of this study, these tenuous and spatially  
00 diffuse aerosol layers can have appreciable AOD, and thus care must be taken to ensure that these sorts  
01 of cases are not misclassified as CAC OWC. Section B3 discusses such cases, possibly found, for  
02 example, over the region of SEAt.

03

04 **B1. Select specific Opaque Water Clouds suitable for DR technique**

05 Successful application of the DR method (Eq. 2 or Eq. B1) requires a very specific type of underlying  
 06 cloud (step (S1) in Table B1). Table B2 lists the criteria we have applied to the CALIOP 5 km cloud  
 07 layer products for the selection of these specific OWCs over the globe.

08  
 09 **Table B2:** Criteria used to select the Opaque Water Clouds (OWC) for the application of the DR  
 10 method to obtain the AAC frequency of occurrence, AAC optical depth, AAC lidar ratio and  $DARE_{owc}$   
 11 in this study.

criteria	metric	interpretation
C1	Number of cloud layers = 1	a single cloud in each column
C2	High CALIOP cloud-aerosol discrimination (CAD) score ( $90 \leq CAD \leq 100$ ) and high SNR (IAB SNR $> 159$ , $\delta^{owc}$ SNR $> 2$ )	highly confident of cloud classification
C3	Cloud detected at 5 km averaging resolution with CALIOP single shot cloud cleared fraction = 0	cloud is spatially uniform over a 5 km averaging interval
C4	CALIOP opacity flag = 1; surface wind speed $< 9$ m/s	cloud is opaque
C5	CALIOP phase classification is high confidence water; $\delta^{owc} < 0.5$ ; cloud top altitude $< 3$ km; cloud top temperature $\geq -10^\circ$ C	highly confident of cloud phase identification (water)

12 We ensure that each cloud is the only cloud detected within the vertical column (C1) and is guaranteed  
 13 to be of high quality by imposing filters on various CALIOP quality assurance flags (C2). Imposing the  
 14 “single shot cloud cleared fraction = 0” in criterion (C3) assures that the clouds are uniformly detected  
 15 at single shot resolution throughout the full 5 km (15 shot) horizontal extent. As a result, we will

16 intentionally miss any broken clouds and any clouds that show a weaker scattering intensity within one  
17 or more laser pulses with the 15 shot average. On the other hand, enforcing the single shot cloud  
18 fraction = 0 criteria simultaneously ensures that all  $\tau_{AAC}^{DR}$  values in this study will lie below a certain  
19 threshold: larger values would attenuate the signal to the point that single shot detection of underlying  
20 clouds is no longer likely. Consequently, some highly attenuating biomass burning events (e.g., with  
21  $\tau_{AAC}^{DR} > 2.5$ ) can be excluded from the cases considered here.

22 At high surface wind speeds over oceans, the CALIOP V3 layer detection algorithm may fail to detect  
23 surface backscatter signals underneath optically thick but not opaque layers. In such cases, CALIOP's  
24 standard algorithm may misclassify the column as containing an opaque overlying cloud. To avoid such  
25 scenarios, we exclude all the cases with high surface wind conditions (C4). Let us note that this  
26 condition was applied on the entire dataset, disregarding the surface type (i.e. land or ocean), as our  
27 OWC dataset resides mostly over ocean surfaces (see Figure 1b).

28 Criterion (C5) requires that the OWC be both low enough (cloud top below 3km) and warm enough  
29 (cloud top temperature above  $-10^{\circ}\text{C}$  as in Zelinka et al. [2012]) to ensure that it is composed of liquid  
30 water droplets. After applying all the criteria of Table B2, the median OWC top height of our dataset is  
31  $\sim 1.6$  km. According to Hu et al. [2009], any feature showing a cloud layer integrated volume  
32 depolarization ratio above 50% should correspond to an ice cloud with randomly oriented particles.  
33 Criterion (C5) assures the deletion of such cases.

34 The averaged single-layer, high QA, uniform cloud (i.e. C1-C3 in Table B2) has a top altitude of  $\sim 8$   
35 km, a top temperature around  $-38^{\circ}\text{C}$  and mean surface winds of  $\sim 6\text{ m s}^{-1}$ . Selecting only those clouds

36 with top temperatures above  $-10^{\circ}$  C removes 30-40% of the observations. Subsequently filtering out  
 37 clouds with top heights above 3 km removes an additional 30% of the observations. Finally, filtering  
 38 out clouds with underlying winds above  $9 \text{ m s}^{-1}$  deletes another 20% of the observations. Among all  
 39 single-layer, high QA, uniform clouds (i.e. C1-C3 in Table B2), we find that  $\sim 45\text{-}50\%$  are opaque  
 40 clouds (C4), and that  $\sim 11\text{-}12\%$  satisfy all criteria (C1-C5) of Table B2.

41

42 **B2. Select a subset of Opaque Water Clouds with clear air above**

43 To distinguish between OWCs having clear skies above (i.e., unobstructed clouds, see S2 in Table B1)  
 44 and those having overlying aerosols, we examine the overlying integrated attenuated backscatter  
 45 reported in the CALIOP Level 2 cloud layer products. The total Integrated Attenuated Backscatter  
 46 (IAB) value above a cloud (i.e.,  $IAB^{\text{tot}}_{\text{aboveCloud}}$ ) can be written as follows:

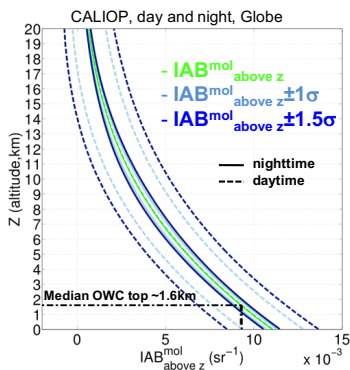
47 
$$IAB^{\text{tot}}_{\text{aboveCloud}} = \int_0^{\text{cloudtop}} [\beta_a(r)T_a^2(0,r)T_m^2(0,r)]dr + \int_0^{\text{cloudtop}} [\beta_m(r)T_m^2(0,r)T_a^2(0,r)]dr \quad (\text{B4})$$

48 Here  $\beta_a(r)$  and  $\beta_m(r)$  are, respectively, the aerosol and the molecular backscatter coefficients ( $\text{km}^{-1} \text{ sr}^{-1}$ )  
 49 at range  $r$  (km), and  $T_a^2(0,r)$  and  $T_m^2(0,r)$  are the two-way transmittances between the lidar (at range  $r =$   
 50 0) and range  $r$  due to, respectively, aerosols and molecules.

51 Figure B1 shows simulated profiles of the integrated attenuated backscatter above any given altitude,  $z$ ,  
 52 ( $IAB^{\text{mol}}_{\text{above } z}$ ) for a purely molecular atmosphere for both daytime (solid green curve) and nighttime  
 53 conditions (dashed green curve). These data were generated by the CALIPSO lidar simulator [Powell et  
 54 al., 2002; Powell, 2005; Powell et al., 2006] using molecular and ozone number density profiles

Deleted: B6

56 obtained from the GEOS-5 atmospheric data products distributed by the NASA Goddard Global  
 57 Modeling and Assimilation Office (GMAO). The error envelopes at  $\pm 1$  standard deviation (light blue  
 58 curves) and  $\pm 1.5$  standard deviation (dark blue curves) around the mean represent measurement  
 59 uncertainties for CALIPSO profiles averaged to a nominal horizontal distance of 5 km. The mean  
 60  $IAB^{\text{mol}}_{\text{above } z}$  profiles represent an average of all data along the CALIPSO orbit track on 17 March 2013  
 61 that began at 03:29:28 UTC and extended from 78.8°N, 20.3°E to 77.3°S, 77.0°W. Spot checks of  
 62 mean  $IAB^{\text{mol}}_{\text{above } z}$  profiles from different seasons show variations of  $\sim 10\%$  or less, depending on  
 63 latitude, for altitudes of 3 km and below. The largest differences are found poleward of 30°. While the  
 64 daytime and nighttime mean values are, as expected, essentially indistinguishable from one another, the  
 65 error envelopes differ drastically due to the influence of solar background noise during daylight  
 66 measurements. In this study, we use nighttime measurements only.



67  
 68 **Figure B1:** Nighttime (solid) and daytime (dashed) simulated vertical profile of integrated attenuated  
 69 backscatter above any given altitude,  $z$ ,  $IAB^{\text{mol}}_{\text{above } z}$  (green curve). The light blue (respectively dark  
 70

70 blue) envelope shows 1 (respectively 1.5) standard deviation ( $\sigma$ ) around the  $IAB^{\text{mol}}_{\text{above } z}$  profile. Data  
 71 was generated by the CALIPSO lidar simulator [Powell et al., 2002 and 2006]. The  $IAB^{\text{mol}}_{\text{above } z}$  value  
 72 associated to the median OWC top height of  $\sim 1.6$  km in our dataset corresponds to  $0.0093 \text{ sr}^{-1}$ .

73  
 74 In this study, we assume “clear air” when  $IAB^{\text{tot}}_{\text{aboveCloud}}$  is within the simulated  $IAB^{\text{mol}}_{\text{aboveCloud}}$  value  $\pm$   
 75  $1\sigma$  (i.e., the light blue envelope shown in Figure B1). This definition of “clear air above” conditions is  
 76 somewhat more restrictive than those imposed in previous studies. For example, Liu et al. [2015]  
 77 conducted an extensive study of AAC optical depths and lidar ratios using CALIOP measurements over  
 78 the tropical and southeast Atlantic. To identify clear air above cloud cases, Liu et al. [2015] require that  
 79 the integrated attenuated scattering ratio, defined as

$$81 \quad ASR = \frac{\int_{3\text{km}}^{OWC_{\text{top}}} (\beta_m(r) + \beta_a(r)) T_m^2(0,r) T_a^2(0,r) dr}{\int_{3\text{km}}^{OWC_{\text{top}}} \beta_m(r) T_m^2(0,r) dr}$$

(B5)

Deleted: B7

82 , fall within the range of  $0.95 < ASR < 1.05$ , irrespective of cloud top altitude. For comparison, at the  
 83 maximum OWC top altitude used in our analyses (3 km),  $(IAB^{\text{mol}}_{\text{aboveCloud}} \pm 1\sigma) / IAB^{\text{mol}}_{\text{aboveCloud}} = 1 \pm$   
 84  $0.0380$ . This restriction tightens for lower cloud top heights; e.g., at our mean OWC top altitude of 1.6  
 85 km,  $(IAB^{\text{mol}}_{\text{aboveCloud}} \pm 1\sigma) / IAB^{\text{mol}}_{\text{aboveCloud}} = 1 \pm 0.0325$ .

86 The pioneering study by Chand et al. [2008], who first used the CALIOP DR method to assess the  
 87 radiative effects of aerosols above clouds, took a different approach to identifying “clear above cloud”  
 88 cases. Rather than examining the overlying IAB, they instead assumed clear air above conditions  
 71

90 whenever  $IAB^{OWC}_{SS} > 0.025 \text{ sr}^{-1}$ . As will be shown in section B3, in addition to the  $IAB^{mol}_{aboveCloud}$   
91 limits cited above, our study also enforces limits on  $IAB^{OWC}_{SS,CAC}$ . This combination of limits on both  
92  $IAB^{mol}_{aboveCloud}$  and  $IAB^{OWC}_{SS,CAC}$  serves to more effectively reject aerosol-contaminated profiles from  
93 the “clear above” data set than either one alone.

94

### 95 **B3. Process median seasonal maps of Integrated Attenuated Backscatter of Opaque Water Clouds** 96 **showing Clear Air Above**

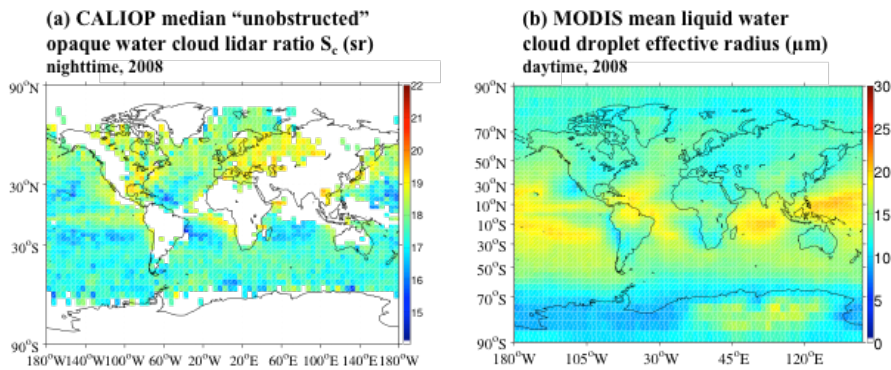
97 Once we select specific OWCs (i.e., that satisfy the criteria of Table B2) and define which ones are  
98 “unobstructed” (see section B2), we can easily compute  $IAB^{OWC}_{SS,CAC}$  by using Eq. (B3). For clouds  
99 that totally attenuate the lidar signal (i.e., cloud optical depths greater than  $\sim 6$  [Young et al., 2018]),  
00  $IAB^{OWC}_{SS,CAC}$  in Eq. (2) or Eq. (B1) is related to the OWC lidar ratio (called  $S_c$ ), so that

$$01 \quad S_c = 1 / (2 \times \eta^{OWC} \times IAB^{OWC}_{CAC}) = 1 / (2 \times IAB^{OWC}_{SS,CAC}) \quad (B6)$$

02 [Platt, 1973]. OWC  $S_c$  values are relatively stable at the visible and near infrared wavelengths [Pinnick  
03 et al., 1983, O’Connor et al., 2004], but show large variations over land [Pinnick et al., 1983; Hu et al.,  
04 2006].  $S_c$  is known to vary as a function of cloud droplet microphysics, and is especially sensitive to  
05 cloud droplet effective radius ( $R_e$ ) and the imaginary part of the refractive index (see Fig. 8 of Deaconu  
06 et al. [2017]). Hu et al., [2006], Liu et al. [2015] and Deaconu et al. [2017] show that a decrease of  $R_e$  is  
07 often paired with an increase of estimated  $S_c$  at 532 nm for pure, non-aerosol-contaminated water  
08 clouds (i.e., cloud droplets having an imaginary refractive index of 0).

10 As an example, Figure B3a shows the median nighttime CALIOP  $S_c$  values over the globe during 2008.  
11 Figure B3b shows MODIS AQUA-derived mean liquid water  $R_c$  in 2008 (using MODIS Level 3  
12 monthly product “Cloud Effective Radius Liquid Mean Mean”).

13



14 **Figure B3:** a) Global CALIOP yearly median nighttime “unobstructed” (i.e. clear air above) OWC lidar  
15 ratio,  $S_c$ , in 2008 that satisfy all criteria of Table B2. For the reasons outlined in this section, any OWC  
16 along the CALIOP track for which  $S_c > 20$  sr or  $S_c < 14$  sr is deleted before temporal and spatial  
17 averaging. White pixels show a limited number of OWCs; b) Global MODIS yearly mean daytime  
18 liquid water cloud droplet effective radius,  $R_c$  (in  $\mu\text{m}$ , “Cloud Effective Radius Liquid Mean Mean”  
19 parameter from MODIS MYD08\_M3 product).

20

22 Greater  $S_c$  values paired with lower cloud  $R_c$  can be seen offshore and close to the west coasts of Africa  
23 and the Americas on Figure B3. Other notable regions of low cloud  $R_c$  and high  $S_c$  on Figure B3 are  
24 above industrial regions like northern Europe, the eastern US and South East Asia. These results appear  
25 to support Twomey's analysis [Twomey, 1977; Rosenfeld and Lensky, 1998], showing an enhancement  
26 of the cloud albedo through the increase of droplet number concentration and a decrease in the droplet  
27 size driven by increased aerosol concentration. On the other hand, Figure B3a mostly exhibits low  $S_c$   
28 values (paired with large  $R_c$ ) over the inter-tropical convergence zone (ITCZ), likely associated with  
29 deep convective regimes. In addition, Figure B3a generally shows larger OWC  $S_c$  values in the northern  
30 hemisphere than in the southern hemisphere, which we attribute to differences in sources of cloud  
31 condensation nuclei. Figure B3b shows patterns that are generally similar to those in Figure B3a, but of  
32 opposite intensity. Let us note that the polarization measurements from the space-borne POLDER  
33 sensor [Deschamps et al., 1994] were also used to estimate  $R_c$  of liquid water clouds over the globe  
34 [Bréon and Colzy, 2000] and seem to be in qualitative agreement with the findings of Figure B3b.

35 During our assessment of 5 years of CALIOP data over the globe, we have observed significantly  
36 higher "unobstructed" OWC  $S_c$  values (i.e.,  $S_c > 20$  sr, not shown on Fig B3a) near the coasts of West  
37 Africa and over the region of SE Asia (e.g., see Young et al., [2018]). These may be physically  
38 plausible and either (1) associated with small cloud  $R_c$ , resulting from the Twomey's effect as explained  
39 above or (2) associated with the presence of light-absorbing aerosols residing within the OWCs  
40 [Mishchenko et al., 2014; Chylek and Hallett, 1992; Wittbom et al., 2014]. These aerosols would be  
41 undetected in our  $IAB_{aboveCloud}^{mol}$  clear air selection method (see section B2) and would impact the  
42 chemical composition of the cloud droplets, modifying their backscattered light. The latter is well

43 illustrated in Fig. 8 of Deaconu et al. [2017], which shows simulations of cloud  $S_c$  with an imaginary  
44 part of the refraction index equals to 0.0001, as a function of cloud droplet effective radius. Other  
45 reasons for these unusually high  $S_c$  values could be the sources of uncertainty noted (a), (b), (c) and (d)  
46 in the beginning of section B, with (c) (i.e., the SNR of the backscatter data within the layer) possibly  
47 having a much higher impact on  $S_c$  than all other factors. An additional source of uncertainty on the  
48 retrieval of  $S_c$  could be a failure of the CALIPSO surface detection scheme. If CALIOP fails to detect  
49 the surface adequately, part of the Earth's surface could be misclassified as an opaque water cloud and  
50 these misclassified clouds would have abnormally high  $S_c$ .

51 Let us note that the vast majority of the  $S_c$  values reported in the literature (i.e., in Hu et al., [2006], Liu  
52 et al. [2015] and Deaconu et al., [2017]) are estimated using a Mie code and not directly measured.  
53 However, none of these results show  $S_c$  values above 20 sr for non-aerosol-contaminated OWCs. On the  
54 other hand (and to add a lower bracket on our OWC  $S_c$  calculations), none of these results show  $S_c$   
55 values below 14 sr. For this reason, we have imposed an additional threshold on the OWC  $S_c$  values as  
56 part of step (S3) in Table B1: we delete any "unobstructed" OWC along the CALIOP track for which  $S_c$   
57  $> 20$  sr (i.e., unrealistically small water cloud droplets) or an  $S_c < 14$  sr (i.e., unrealistically large water  
58 cloud droplets). Every OWC  $S_c$  value along the CALIOP track was then compiled to produce four  
59 global median seasonal  $4^\circ \times 5^\circ$  maps of OWC  $S_c$  using 5 years of night-time CALIOP data (from 2008 to  
60 2012).

61 There is additional precedent for establishing an upper limit of  $S_c = 20$  sr. Note that, from Eq. B6, the  
62 value of  $IAB^{OWC}_{SS,CAC}$  corresponding to  $S_c = 20$  sr is  $0.025 \text{ sr}^{-1}$ . As mentioned earlier, this is the same  
63 OWC IAB threshold value used by Chand et al. [2008] to identify their “clear air above” cases.

64

66

Deleted: 8

Deleted: B4. Extinction-to-Backscatter (Lidar) Ratio

Table B3 lists some typical, recently reported values of the aerosol lidar ratios ( $S_a$ ) measured for various aerosol types. These data include CALIOP retrievals for several species (e.g., marine, dust, and smoke) as well as ground-based measurements made using high spectral resolution lidars (HSRL) and Raman lidars.

Table B3: retrieved aerosol extinction-to-backscatter ratios ( $S_a$ ) reported in the literature (PBL: Planetary Boundary Layer)  
 $S_a$  (532 nm, sr) ... [3]

78 **Data Availability:**

79 This study used the following A-Train data products: (i) CALIPSO version 3 lidar level 1 profile  
80 products (Powell et al. [2013]; NASA Langley Research Center Atmospheric Science Data Center;  
81 [https://doi.org/10.5067/CALIOP/CALIPSO/CAL\\_LID\\_L1-ValStage1-V3-01\\_L1B-003.01](https://doi.org/10.5067/CALIOP/CALIPSO/CAL_LID_L1-ValStage1-V3-01_L1B-003.01); last access:  
82 26 September 2018), (ii) CALIPSO version 3 lidar level 2 5 km cloud layer products (Powell et al.  
83 [2013]; NASA Langley Research Center Atmospheric Science Data Center;  
84 [https://doi.org/10.5067/CALIOP/CALIPSO/CAL\\_LID\\_L2\\_05kmCLay-Prov-V3-01\\_L2-003.01](https://doi.org/10.5067/CALIOP/CALIPSO/CAL_LID_L2_05kmCLay-Prov-V3-01_L2-003.01); last  
85 access: 26 September 2018), (iii) MODIS Atmosphere L2 Version 6 Aerosol Product (Levy and Hsu  
86 [2015]; NASA MODIS Adaptive Processing System, Goddard Space Flight Center, USA;  
87 [http://dx.doi.org/10.5067/MODIS/MOD04\\_L2.006](http://dx.doi.org/10.5067/MODIS/MOD04_L2.006); last access: 26 September 2018), and (iv) L2  
88 Version 3 OMI products OMAERO [Stein-Zweers and Veefkind, 2012] and OMAERUV [Torres,  
89 2006].

90

91 **Author contributions:**

92 The overarching research goals were formulated by Dr Redemann, Dr. Kacenelenbogen, Dr. Young and  
93 Mr. Vaughan influenced the evolution of these research goals. Dr. Kacenelenbogen carried out the  
94 formal analyses, investigations and visualizations and wrote the original draft. All co-authors have  
95 reviewed and edited the multiple drafts of the manuscript. The methodology behind the global  
96 application of the DR method to CALIOP measurements was first developed by Dr. Hu, and adapted by  
97 Dr. Kacenelenbogen, Dr. Young, Mr. Vaughan, and Ms. Powell to accommodate the requirements of

98 this study. The methodology for using this combination of A-Train satellites to infer aerosol intensive  
99 radiative properties was conceptualized by Dr Redemann. The joint MODIS-OMI-CALIOP aerosol  
00 radiative properties were developed and provided by Dr. Shinozuka, Mr. Livingston and Ms. Zhang. Dr.  
01 LeBlanc performed the radiative transfer calculations that provided Direct Aerosol Radiative Effects  
02 estimates in clear skies and above clouds.

03

04 **Competing interests:**

05 The authors declare that they have no conflict of interest.

06

07 **Acknowledgements:**

08 We thank the CALIPSO lidar science working group and data management team for their efforts in  
09 providing and discussing these data sets. We appreciate the comments of [Dr. Devasthale and other](#)  
10 reviewers that have helped us to improve the paper. We are grateful for comments from Dr. Zuidema  
11 and Dr. Wood on cloud microphysics over the South East Atlantic. [We also thank Dr. Pistone for her](#)  
12 [help](#). This study was funded in part by NASA's Research Opportunities in Space and Earth Sciences  
13 (ROSES) program under grant NNH12ZDA001N-CCST.

14

Deleted: the

16 **References**

17 Alfaro-Contreras, R., Zhang, J., Reid, J. S., Campbell, J. R., and Holz, R. E., Evaluating the impact  
18 of aerosol particles above cloud on cloud optical depth retrievals from MODIS, *J. Geophys. Res.*  
19 *Atmos.*, 119, 5410–5423, doi:10.1002/2013JD021270, 2014.

20 Alfaro-Contreras, R., Zhang, J., Campbell, J. R., and Reid, J. S., Investigating the frequency and  
21 interannual variability in global above-cloud aerosol characteristics with CALIOP and OMI, *Atmos.*  
22 *Chem. Phys.*, 16, 47-69, doi:10.5194/acp-16-47-2016, 2016.

23 Anderson, G., Clough, S., Kneizys, F., Chetwynd, J., and Shettle, E., AFGL atmospheric constituent  
24 profiles (0-120 km), Tech. Rep. AFGL-TR-86-0110, Air Force Geophys. Lab., Hanscom Air Force  
25 Base, Bedford, Mass, 1986.

26 Anderson, T. E., Charlson, R. J., Winker, D. M., Ogren, J. A., and Holmen, K.: Mesoscale  
27 Variations of Tropospheric Aerosols, *J. Atmos. Sci.*, 60, 119–136, 2003.

28 Arola, A., et al., Influence of observed diurnal cycles of aerosol optical depth on aerosol direct  
29 radiative effect, *Atmos. Chem. Phys.*, 13.15: 7895-7901., 2013.

30 ~~Bréon, F. M. and S. Colzy, Global distribution of cloud droplet effective radius from POLDER  
31 polarization measurements, *Geo. Reas. Lett.*, Vol. 27, N 24, P 4065-4068, 2000.~~

**Deleted:** Blot, R., and Coauthors, Ultrafine sea spray aerosol over the southeastern Pacific: Open-ocean contributions to marine boundary layer CCN. *Atmos. Chem. Phys.*, 13, 7263–7278, doi:10.5194/acp-13-7263-2013, 2013.

32 ~~Buras, R., Dowling, T., and Emde, C., New secondary-scattering correction in DISORT with  
33 increased efficiency for forward scattering, *J. Quant. Spectrosc. Ra.*, 112, 2028–2034, 2011.~~

**Deleted:** Bréon, F-M., Aerosol extinction-to-backscatter ratio derived from passive satellite measurements, *Atmos. Chem. Phys.* 13.17: 8947-8954, 2013.

34 Candlish, L. M., R. L. Raddatz, G. G. Gunn, M. G. Asplin and D. G. Barber: A Validation of

42 CloudSat and CALIPSO's Temperature, Humidity, Cloud Detection, and Cloud Base Height over  
43 the Arctic Marine Cryosphere, *Atmos. Ocean*, 51, 249–264, doi:10.1080/07055900.2013.798582,  
44 2013.

45 Chand, D., T. L. Anderson, R. Wood, R. J. Charlson, Y. Hu, Z. Liu, and M. Vaughan, Quantifying  
46 above-cloud aerosol using spaceborne lidar for improved understanding of cloudy-sky direct climate  
47 forcing, *J. Geophys. Res.*, 113, D13206, doi:10.1029/007JD009433, 2008.

48 Chand, D., R. Wood, T. L. Anderson, S. K. Satheesh, and R. J. Charlson, Satellite-derived direct  
49 radiative effect of aerosols dependent on cloud cover, *Nat. Geosci.*, 2, 181–184,  
50 doi:10.1038/ngeo437, 2009.

51 ~~Chang, Ian, and Sundar A. Christopher, "Identifying Absorbing Aerosols Above Clouds From the~~  
52 ~~Spinning Enhanced Visible and Infrared Imager Coupled With NASA A-Train Multiple Sensors."~~  
53 ~~IEEE T. Geosci. Remote. S., 54.6: 3163-3173, 2016.~~

54 Chang, Ian, and Sundar A. Christopher., "The impact of seasonalities on direct radiative effects and  
55 radiative heating rates of absorbing aerosols above clouds." *Q. J. Roy. Meteor. Soc.*, 143.704: 1395-  
56 1405, 2017.

57 [Chin, Mian. \*Atmospheric aerosol properties and climate impacts\*. Diane Publishing, 2009](#)

58 Chung, C. E., V. Ramanathan, D. Kim, and I. A. Podgorny: Global anthropogenic aerosol direct  
59 forcing derived from satellite and ground-based observations. *J. Geophys. Res.*, 110, D24207,  
60 doi:10.1029/2005JD006356, 2005.

**Deleted:** Chand, D., Hegg, D. A., Wood, R., Shaw, G. E., Wallace, D., and Covert, D. S., Source attribution of climatically important aerosol properties measured at Papos (Chile) during VOCALS, *Atmos. Chem. Phys.*, 10, 10789–10801, doi:10.5194/acp-10-10789-2010, 2010.

66 Chylek, Petr, and John Hallett, "Enhanced absorption of solar radiation by cloud droplets containing  
67 soot particles in their surface." *Q. J. Roy. Meteor. Soc.*, 118.503: 167-172, 1992.

68 Costantino, L. and Bréon, F.-M., Satellite-based estimate of aerosol direct radiative effect over the  
69 South-East Atlantic, *Atmos. Chem. Phys. Discuss.*, 13, 23295-23324, doi:10.5194/acpd-13-23295-  
70 2013, 2013.

71 Cox, Charles, and Walter Munk. "Measurement of the roughness of the sea surface from  
72 photographs of the sun's glitter." *Josa* 44.11: 838-850, 1954.

73 ~~Deaconu, L. T., F. Waquet, D. Josset, N. Ferlay, F. Peers, F. Thieuleux, F. Ducos, N. Pascal, D.  
74 Tanré, and P. Goloub, "Consistency of aerosols above clouds characterization from A-Train active  
75 and passive measurements", *Atmos. Meas. Tech. Discuss.*, doi:10.5194/amt-2017-42, 2017.~~

**Deleted:** Dawson, N. Meskhidze, D. Josset, and S. Gassó, A new study of sea spray optical properties from multi-sensor spaceborne observations, *Atmos. Chem. Phys. Discuss.*, 14, 213–244, 2014.

76 De Graaf, M., L. G. Tilstra, P. Wang, and P. Stammes, Retrieval of the aerosol direct radiative  
77 effect over clouds from spaceborne spectrometry, *J. Geophys. Res.*, 117, D07207,  
78 doi:10.1029/2011JD017160, 2012.

79 De Graaf, M., N. Bellouin, L. G. Tilstra, J. Haywood, and P. Stammes, Aerosol direct radiative  
80 effect of smoke over clouds over the southeast Atlantic Ocean from 2006 to 2009, *Geophys. Res.  
81 Lett.*, 41, 7723–7730, doi:10.1002/2014GL061103, 2014.

82 Deschamps, P. Y., F. M. Breon, M. Leroy, A. Podaire, A. Bricaud, J. C. Buriez and G. Seze, The  
83 POLDER mission: Instrument characteristics and scientific objectives. *IEEE T. Geosci. Remote. S.*,  
84 32, 598-615, 1994.

88 Devasthale, A., and M. A. Thomas, A global survey of aerosol-liquid water cloud overlap based on  
89 four years of CALIPSO–CALIOP data, *Atmos. Chem. Phys.*, 11, 1143–1154, 2011.

90 Di Girolamo L, Liang L, Platnick S. A global view of one-dimensional solar radiative transfer  
91 through oceanic water clouds. *Geophys. Res. Lett.*;37:L18809, 2010.

92 Emde, C., Buras-schnell, R., Kylling, A., Mayer, B., Gasteiger, J., Hamann, U., Kylling, J., Richter,  
93 B., Pause, C., Dowling, T. and Bugliaro, L., The libRadtran software package for radiative transfer  
94 calculations (version 2.0.1), *Geosci. Model Dev.*, 9, 1647–1672, doi:10.5194/gmd-9-1647-2016,  
95 2016.

96 Feng, N., and S. A. Christopher, Measurement-based estimates of direct radiative effects of  
97 absorbing aerosols above clouds, *J. Geophys. Res. Atmos.*, 120, 6908–6921, doi:10.1002/  
98 2015JD023252, 2015.

99 Fu, Q. and Liou, K., On the correlated k-distribution method for radiative transfer in  
00 nonhomogeneous atmospheres, *J. Atmos. Sci.*, 49, 2139–2156, 1992.

**Deleted:** Fernald F.G., B. M. Herman and J. A. Reagan, Determination of Aerosol Height Distribution by Lidar, *J. Appl. Meteor.*, 11, 482-489, 1972.¶

01 Guzman, R., Chepfer, H., Noel, V., Vaillant de Guélis, T., Kay, J. E., Raberanto, P., Cesana, G.,  
02 Vaughan, M. A., and Winker, D. M.: Direct atmosphere opacity observations from CALIPSO  
03 provide new constraints on cloud-radiation interactions, *J. Geophys. Res.*, 122, 1066–1085,  
04 <https://doi.org/10.1002/2016JD025946>, 2017.

**Deleted:** Giannakaki, E., van Zyl, P. G., Müller, D., Balis, D., and Komppula, M.: Optical and microphysical characterization of aerosol layers over South Africa by means of multi-wavelength depolarization and Raman lidar measurements, *Atmos. Chem. Phys.*, 16, 8109-8123, <https://doi.org/10.5194/acp-16-8109-2016>, 2016.¶

05 Haywood, J. M., and V. Ramaswamy, Global sensitivity studies of the direct radiative  
06 forcing due to anthropogenic sulfate and black carbon aerosols, *J. Geophys. Res.*, 103,

**Formatted:** references, Line spacing: Double

16 [6043–6058, doi:10.1029/97JD03426, 1998.](#)

17 [Holben, B. N., Eck, T. F., Slutsker, I., Tanré, D., Buis, J. P., Setzer, A., Vermote, E., Reagan, J. A.,](#)  
18 [Kaufman, Y. J., Nakajima, T., Lavenu, F., Jankowiak, I., and Smirnov, A., AERONET–A federated](#)  
19 [instrument network and data archive for aerosol characterization, Remote Sens. Environ., 66, 1–16,](#)  
20 [1998.](#)

21 [Hu, Y., Vaughan, M., Winker, D., Liu, Z., Noel, V., Bissonnette, L., Roy, G., McGill, M., and](#)  
22 [Treppe, C., A simple multiple scattering-depolarization relation of water clouds and its potential](#)  
23 [applications, Proceedings of 23rd International Laser Radar Conference, Nara, Japan, 24–28 July,](#)  
24 [19–22, 2006.](#)

25 [Hu, Y., Vaughan, M., Liu, Z., Lin, B., Yang, P., Flittner, D., Hunt, W., Kuehn, R., Huang, J., Wu,](#)  
26 [D., Rodier, S., Powell, K., Treppe, C., and Winker, D.: The depolarization-attenuated backscatter](#)  
27 [relation: CALIPSO lidar measurements vs. theory, Optics Express, 15, 5327–5332,](#)  
28 [doi:10.1364/OE.15.005327, 2007a.](#)

29 [Hu, Y., M. Vaughan, Z. Liu, K. Powell, and S. Rodier, Retrieving Optical Depths and Lidar Ratios](#)  
30 [for Transparent Layers Above Opaque Water Clouds From CALIPSO Lidar Measurements, IEEE](#)  
31 [Geosci. Remote Sens. Lett., 4, 523-526, 2007b.](#)

32 [Hu, Y., et al., CALIPSO/CALIOP cloud phase discrimination algorithm, J. Atmos. Ocean. Tech.,](#)  
33 [26.11: 2293-2309, 2009.](#)

34 [Hunt, W. H., D. M. Winker, M. A. Vaughan, K. A. Powell, P. L. Lucker, and C. Weimer, CALIPSO](#)

**Formatted:** Font: 12 pt, Font color: Text 1, Not Highlight

**Deleted:** ¶

Haywood, J. M., S. R. Osborne, P. Francis, M. Glew, N. Loeb, E. Highwood, D. Tanré, G. Myhre, P. Formenti, and E. Hirst, Radiative properties and direct radiative effect of Saharan dust measured by the C-130 aircraft during SHADE: 1. Solar spectrum, *J. Geophys. Res.*, 108(D18), 8577, doi:10.1029/2002JD002687, 2003.¶

Herman, J. R., P. K. Bhartia, O. Torres, C. Hsu, C. Sefior, and E. Celarier, Global distribution of UV-absorbing aerosols from Nimbus 7/TOMS data, *J. Geophys. Res.*, 102, 16,911–16,922, 1997.¶

**Deleted:** 'c

47 lidar description and performance assessment, *J. Atmos. Ocean. Tech.*, 26, 1214–1228,  
48 doi:10.1175/2009JTECHA1223.1, 2009.

49 Jethva, H., O. Torres, L. A. Remer, and P. K. Bhartia, A color ratio method for simultaneous  
50 retrieval of aerosol and cloud optical thickness of above-cloud absorbing aerosols from passive  
51 sensors: Application to MODIS measurements, *IEEE T. Geosci. Remote. S.*, 51(7), 3862–3870,  
52 doi:10.1109/TGRS.2012.2230008, 2013.

53 Jethva, H., O. Torres, F. Waquet, D. Chand, and Y. Hu, How do A-train sensors intercompare in the  
54 retrieval of abovecloud aerosol optical depth? A case study-based assessment, *Geophys. Res. Lett.*,  
55 41, doi:10.1002/2013GL058405, 2014.

56 Kacenelenbogen, M., J. Redemann, M. A. Vaughan, A. H. Omar, P. B. Russell, S. Burton, R. R.  
57 Rogers, R. A. Ferrare, and C. A. Hostetler, An evaluation of CALIOP/CALIPSO's aerosol-above-  
58 cloud detection and retrieval capability over North America, *J. Geophys. Res. Atmos.*, 119, 230–  
59 244, doi:10.1002/2013JD020178, 2014.

60 Kassianov, E., et al. "Do diurnal aerosol changes affect daily average radiative forcing?" *Geophys.*  
61 *Res. Lett.*, 40.12: 3265-3269, 2013.

62 Kim, S.-W., E.-S. Chung, S.-C. Yoon, B.-J. Sohn, and N. Sugimoto, "Intercomparisons of cloud-top  
63 and cloud-base heights from ground-based Lidar, CloudSat and CALIPSO measurements", *Int. J.*  
64 *Remote Sens.*, 32, 1179–1197, doi:10.1080/01431160903527439, 2011.

65 Kim, M.-H., A. H. Omar, M. A. Vaughan, D. M. Winker, C. R. Trepte, Y. Hu, Z. Liu and S.-W.  
66 Kim, 2017: "Quantifying the low bias of CALIPSO's column aerosol optical depth due to

**Deleted:** Josset D., R Rogers, J Pelon, Yongxiang Hu, Zhaoyan Liu, Ali Omar, and Peng-Wang Zhai, CALIPSO lidar ratio retrieval over the ocean, Vol. 19, No. 19 / *Opt. Express.*, 2011.

70 undetected aerosol layers”, *J. Geophys. Res. Atmos.*, **122**, 1098–1113, doi:10.1002/2016JD025797.

71 King, Michael D., et al. "Spatial and temporal distribution of clouds observed by MODIS onboard  
72 the Terra and Aqua satellites." *IEEE T. Geosci. Remote. S.*, 51.7: 3826-3852, 2013.

73 Klein, S. A. and Hartmann, D. L., The seasonal cycle of low stratiform clouds, *J. Climate*, 6, 1587–  
74 1606, 1993.

75 Kovacs, T.: Comparing MODIS and AERONET aerosol optical depth at varying separation  
76 distances to assess ground-based validation strategies for spaceborne lidar, *J. Geophys. Res.*, 111,  
77 D24203, doi:10.1029/2006JD007349, 2006.

78 Leahy, L. V., R. Wood, R. J. Charlson, C. A. Hostetler, R. R. Rogers, M. A. Vaughan, and D. M.  
79 Winker, On the nature and extent of optically thin marine low clouds, *J. Geophys. Res.*, 117,  
80 D22201, doi:10.1029/2012JD017929, 2012.

81 Levy, R., and C. Hsu. "MODIS Atmosphere L2 Aerosol Product." *NASA MODIS Adaptive*  
82 *Processing System*, 2015.

83 ~~Liu, D., Wang, Z., Liu, Z., Winker, D. M., and Trepte, C., A height resolved global view of dust~~  
84 ~~aerosols from the first year CALIPSO lidar measurements, *J. Geophys. Res.*, 113, D16214,~~  
85 ~~doi:10.1029/2007JD009776, 2008.~~

86 Liu, Z., R. Kuehn, M. Vaughan, D. Winker, A. Omar, K. Powell, C. Trepte, Y. Hu, and C.  
87 Hostetler, The CALIPSO cloud and aerosol discrimination: Version 3, Algorithm and test results,  
88 25<sup>th</sup> International Laser and radar conference, 2010.

89 Liu Z, D. Winker, A. Omar, M. Vaughan, J. Kar, C. Trepte, Y. Hu, and G. Schuster, Evaluation of

85

**Deleted:** Liu, Z., N. Sugimoto, and T. Murayama, Extinction-to-backscatter ratio of Asian dust observed with high-spectral-resolution lidar and Raman lidar, *Appl. Optics.*, 41.15, 2760-2767, 2002.

94 CALIOP 532nm aerosol optical depth over opaque water clouds, Atmos. Chem. Phys., 15, 1265–  
95 1288, 2015.

96 [Mace, G. G. and Protat, A.: Clouds over the Southern Ocean as Observed from The RV Investigator](#)  
97 [during CAPRICORN. Part 1: Cloud Occurrence and Phase Partitioning. J. Appl. Meteor. Climatol.,](#)  
98 [57, 1783–1803, doi:10.1175/JAMC-D-17-0194.1, 2018.](#)

99 [Matus, Alexander V., et al., The role of clouds in modulating global aerosol direct radiative effects](#)  
00 [in spaceborne active observations and the Community Earth System Model.” J. Climate, 28.8: 2986-](#)  
01 [3003, 2015.](#)

02 McGill, M. J., M. A. Vaughan, C. R. Trepte, W. D. Hart, D. L. Hlavka, D. M. Winker, and R.  
03 Kuehn, Airborne validation of spatial properties measured by the CALIPSO lidar, J. Geophys. Res.,  
04 **112**, D20201, doi:10.1029/2007JD008768, 2007.

05 Meyer, K., S. Platnick, L. Oreopoulos, and D. Lee, Estimating the direct radiative effect of  
06 absorbing aerosols overlying marine boundary layer clouds in the southeast Atlantic using MODIS  
07 and CALIOP, J. Geophys. Res. Atmos., 118, 4801–4815, doi:10.1002/jgrd.50449, 2013.

08 Meyer, K., S. Platnick, and Z. Zhang: Simultaneously inferring above-cloud absorbing aerosol  
09 optical thickness and underlying liquid phase cloud optical and microphysical properties using  
10 MODIS, J. Geophys. Res. Atmos., 120, 5524–5547, doi:10.1002/2015JD023128, 2015.

11 Min, M., and Z. Zhang, On the influence of cloud fraction diurnal cycle and sub-grid cloud optical  
12 thickness variability on all-sky direct aerosol radiative forcing, J. Quant. Spectrosc. RA., 142: 25-  
13 36, 2014.

**Deleted:** Mamouri, R. E., et al. Low Arabian dust extinction-to-backscatter ratio. Geophys. Res. Lett., 40.17: 4762-4766, 2013.

17 Mishchenko, Michael I., et al., Optics of water cloud droplets mixed with black-carbon aerosols,  
18 Opt. Lett., 39:9: 2607-2610, 2014.

19 Mitchell R. M., S. K. Campbell, and Y. Qin, Recent increase in aerosol loading over the Australian  
20 arid zone, Atmos. Chem. Phys., 10, 1689– 1699, 2010.

21 [O. K.-T., Wood, R., and Tseng, H.-H.: Deeper precipitating PBLs associated with optically thin  
22 veil clouds in the Sc-Cu transition, Geophysical Research Letters, 45, 5177–5184,  
23 <https://doi.org/10.1029/2018GL077084>, 2018.](https://doi.org/10.1029/2018GL077084)

24 O'Connor, E. J., A. J. Illingworth, and R. J. Hogan, A technique for autocalibration of cloud lidar, J.  
25 Atmos. Ocean. Tech., 21, 777– 786, doi:10.1175/1520-0426, 2004.

26 Oikawa, E., T. Nakajima, T. Inoue, and D. Winker, A study of the shortwave direct aerosol forcing  
27 using ESSP/CALIPSO observation and GCM simulation, J. Geophys. Res. Atmos., 118, 3687–  
28 3708, doi:10.1002/jgrd.50227, 2013.

29 Omar, A., et al., The CALIPSO automated aerosol classification and lidar ratio selection algorithm,  
30 J. Atmos. Ocean. Tech., 26, 1994–2014, doi:10.1175/2009JTECHA1231.1, 2009.

31 Oreopoulos, Lazaros, Robert F. Cahalan, and Steven Platnick. "The plane-parallel albedo bias of  
32 liquid clouds from MODIS observations." *Journal of Climate* 20.20: 5114-5125, 2007.

33 Peers F., F. Waquet, C. Cornet, P. Dubuisson, F. Ducos, P. Goloub, F. Szczap, D. Tanré, and F.  
34 Thieuleux, Absorption of aerosols above clouds from POLDER/PARASOL measurements and  
35 estimation of their direct radiative effect, Atmos. Chem. Phys., 15, 4179–4196, 2015.

**Deleted:** Müller, D., A. Ansmann, I. Mattis, M. Tesche, U. Wandinger, D. Althausen, and G. Pisani, Aerosol-type-dependent lidar ratios observed with Raman lidar, J. Geophys. Res., 112, D16202, doi:10.1029/2006JD008292, 2007.¶  
Noel, V., Chepfer, H., Hoareau, C., Reverdy, M., and Cesana, G.: Effects of solar activity on noise in CALIOP profiles above the South Atlantic Anomaly, Atmos. Meas. Tech., 7, 1597–1603, doi:10.5194/amt-7-1597-2014, 2014.¶

**Deleted:** Omar, A., et al., Extinction-to-backscatter ratios of Saharan dust layers derived from in situ measurements and CALIPSO overflights during NAMMA, J. Geophys. Res., 115, D24217, doi:10.1029/2010JD014223, 2010.¶

**Deleted:** Pedrós R., V. Estellés, M. Sicard, J. L. Gómez-Amo, M. Pilar Utrillas, J. A. Martínez-Lozano, F. Rocadenbosch, C. Pérez, and J. M. Baldasano Recio, Climatology of the Aerosol Extinction-to-Backscatter Ratio from Sun-Photometric Measurements, IEEE T. Geosci. Remote. S., 48- 1, 2010.¶

53 Peng et al., The cloud albedo-cloud droplet effective radius relationship for clean and polluted  
54 clouds from RACE and FIRE.ACE, J. Geophys. Res., VOL. 107, NO. D11,  
55 10.1029/2000JD000281, 2002.

56 Penner, J. E., Soot and smoke aerosol may not warm climate. J. Geophys. Res., 108, 4657,  
57 doi:10.1029/2003JD003409, 2003.

58 Peters, K., J. Quaas, and N. Bellouin, Effects of absorbing aerosols in cloudy skies: A satellite study  
59 over the Atlantic Ocean. Atmos. Chem. Phys., 11, 1393–1404, doi:10.5194/acp-11-1393-2011,  
60 2011.

61 Pinnick, R. G., Jennings, S. G., Chylek, P., Ham, C., and Grandy Jr., W. T., Backscatter and  
62 extinction in water clouds, J. Geophys. Res., 88, 6787–6796, 1983.

63 Platnick, S., et al., MODIS Atmosphere L3 Monthly Product. NASA MODIS Adaptive Processing  
64 System, Goddard Space Flight Center, USA, doi:10.5067/MODIS/MOD08\_M3.006, 2015.

65 Platt, C. M. R., Lidar and radiometric observations of cirrus clouds, J. Atmos. Sci., 30.6: 1191-1204,  
66 1973.

67 Powell, K., W. Hunt, and D. Winker, Simulations of CALIPSO Lidar Data, Proceedings of the 21<sup>st</sup>  
68 International Laser Radar Conference (ILRC), Quebec City, Quebec (available at [http://www-  
69 calipso.larc.nasa.gov/resources/pdfs/ILRC\\_2002/ILRC2002\\_Powell\\_Simulator.pdf](http://www-calipso.larc.nasa.gov/resources/pdfs/ILRC_2002/ILRC2002_Powell_Simulator.pdf)), 2002.

70 Powell, K. A., Development of the CALIPSO Lidar Simulator”, M.S. Thesis, Department of  
71 Applied Science, The College of William and Mary, 228 pp, 2005.

72 Powell, K. A., Liu, Z., and W. H. Hunt, Simulation of Random Electron Multiplication in CALIPSO  
73 Lidar Photomultipliers, Proceedings of the 23<sup>rd</sup> International Laser Radar Conference (ILRC), Nara,  
74 Japan (available at [http://www-calipso.larc.nasa.gov/resources/pdfs/ILRC\\_2006/Powell-](http://www-calipso.larc.nasa.gov/resources/pdfs/ILRC_2006/Powell-PhotomultiplierSimulation-2P-23.pdf)  
75 [PhotomultiplierSimulation-2P-23.pdf](http://www-calipso.larc.nasa.gov/resources/pdfs/ILRC_2006/Powell-PhotomultiplierSimulation-2P-23.pdf)), 2006.

76 Powell, K. A., et al., CALIPSO lidar calibration algorithms. Part I: Nighttime 532-nm parallel  
77 channel and 532-nm perpendicular channel, *J. Atmos. Ocean. Tech.*, 26.10: 2015-2033, 2009.

78 Powell, K., Vaughan, M., Winker, D., Lee, K.-P., Pitts, M., Trepte, C., Detweiler, P., Hunt, W.,  
79 Lambeth, J., Lucker, P., Murray, T., Hagolle, O., Lifermann, A., Faivre, M., Garnier, A., and Pelon,  
80 J.: Cloud–Aerosol LIDAR Infrared Pathfinder Satellite Observations (CALIPSO) Data Products  
81 Catalog, Document No: PC-SCI-503, Release 3.5, available on-line at [https://www-](https://www-calipso.larc.nasa.gov/products/CALIPSO_DPC_Rev3x5.pdf)  
82 [calipso.larc.nasa.gov/products/CALIPSO\\_DPC\\_Rev3x5.pdf](https://www-calipso.larc.nasa.gov/products/CALIPSO_DPC_Rev3x5.pdf) (last access: 12 October 2018), 2013.

83 Quijano, A. L., I. N. Sokolik, and O. B. Toon, Radiative heating rates and direct radiative forcing by  
84 mineral dust in cloudy atmospheric conditions. *J. Geophys. Res.*, 105, 12 207–12 219,  
85 doi:10.1029/2000JD900047, 2000.

86 Redemann, J., Vaughan, M. A., Zhang, Q., Shinozuka, Y., Russell, P. B., Livingston, J. M.,  
87 Kacenelenbogen, M., and Remer, L. A., The comparison of MODIS-Aqua (C5) and CALIOP (V2 &  
88 V3) aerosol optical depth, *Atmos. Chem. Phys.*, 12, 3025-3043, doi:10.5194/acp-12-3025-2012,  
89 2012.

90 Redemann J., Y. Shinozuka, M. Kacenelenbogen, S. LeBlanc, M. Segal-Rozenhaimer, M. Vaughan,  
91 P. Stier, N. Schutgens, Use of A-Train aerosol observations to constrain direct aerosol radiative  
92 effects (DARE) and comparisons with AeroCom phase II DARE results, in preparation.

93 Remer, L. A., Y. J. Kaufman, D. Tanré, S. Mattoo, D. A. Chu, J. V. Martins, R.-R. Li, C. Ichoku, R.  
94 C. Levy, R. G. Kleidman, T. F. Eck, E. Vermote and B. N. Holben, The MODIS aerosol algorithm,  
95 products and validation. *J. Atmos. Sci.*,62 (4),947-973, 2005.

96 Rogers, R. R., Hostetler, C. A., Hair, J. W., Ferrare, R. A., Liu, Z., Obland, M. D., Harper, D. B.,  
97 Cook, A. L., Powell, K. A., Vaughan, M. A., and Winker, D. M., Assessment of the CALIPSO  
98 Lidar 532 nm attenuated backscatter calibration using the NASA LaRC airborne High Spectral  
99 Resolution Lidar, *Atmos. Chem. Phys.*, 11, 1295-1311, doi:10.5194/acp-11-1295-2011, 2011.

00 Rosen, J., S. Young, J. Laby, N. Kjöme, and J. Gras, Springtime aerosol layers in the free  
01 troposphere over Australia: Mildura Aerosol Tropospheric Experiment (MATE 98), *J. Geophys.*  
02 *Res.*, 105(D14), 17833–17842, doi:10.1029/2000JD900208, 2000.

03 Rosenfeld, D. and Lensky, I. M., Satellite-based insights into precipitation formation processes in  
04 continental and maritime convective clouds, *B. Am. Meteorol. Soc.*, 79, 2457–2476, 1998.

05 Russell P. B. R., T. J. Swissler, and McCormick M. P., Methodology for error analysis and  
06 simulation of lidar aerosol measurements, *Appl. Optics.*, Vol. 18, Issue 22, pp. 3783-3797, 1979.

07 Santese, M., De Tomasi, F., and Perrone, M. R.: AERONET versus MODIS aerosol parameters at  
08 different spatial resolutions over southeast Italy, *J. Geophys. Res.*, 112, D10214,  
09 doi:10.1029/2006JD007742, 2007.

10 Sayer, Andrew M., et al., Extending “Deep Blue” aerosol retrieval coverage to cases of absorbing  
11 aerosols above clouds: Sensitivity analysis and first case studies, *J. Geophys. Res. Atmos.*, 121.9:  
12 4830-4854, 2016.

13 Schulz, M., Textor, C., Kinne, S., Balkanski, Y., Bauer, S., Bernsten, T., Berglen, T., Boucher, O.,  
14 Dentener, F., Guibert, S., Isaksen, I. S. A., Iversen, T., Koch, D., Kirkevåg, A., Liu, X., Montanaro,  
15 V., Myhre, G., Penner, J. E., Pitari, G., Reddy, S., Seland, Ø., Stier, P., and Takemura, T., Radiative  
16 forcing by aerosols as derived from the AeroCom present-day and pre-industrial simulations,  
17 *Atmos. Chem. Phys.*, 6, 5225-5246, doi:10.5194/acp-6-5225-2006, 2006.

18 ~~Schutgens, N. A. J., Nakata, M., and Nakajima, T.: Validation and empirical correction of MODIS  
19 AOT and AE over ocean, *Atmos. Meas. Tech.*, 6, 2455–2475, doi:10.5194/amt-6-2455-2013, 2013.~~

20 Shinozuka, Y. and Redemann, J.: Horizontal variability of aerosol optical depth observed during the  
21 ARCTAS airborne experiment, *Atmos. Chem. Phys.*, 11, 8489–8495, doi:10.5194/acp-11-8489-  
22 2011, 2011.

23 Stamnes, K., Tsay, S.-C., Wiscombe, W., and Jayaweera, K., Numerically stable algorithm for  
24 discrete-ordinate-method radiative transfer in multiple scattering and emitting layered media, *Appl.*  
25 *Opt.*, 27, 2502–2509, 1988.

26 Stein-Zweers D. and P. Veefkind, OMI/Aura Multi-wavelength Aerosol Optical Depth and Single  
27 Scattering Albedo 1-orbit L2 Swath 13x24 km V003, NASA Goddard Space Flight Center, Goddard  
28 Earth Sciences Data and Information Services Center (GES DISC), 10.5067/Aura/OMI/DATA2001  
29 <https://doi.org/10.5067/Aura/OMI/DATA2001>, 2012.

30 Thorsen, T. J., Q. Fu, and J. M. Comstock, Comparison of the CALIPSO satellite and ground-based  
31 observations of cirrus clouds at the ARM TWP sites, *J. Geophys. Res.*, **116**, D21203,  
32 doi:10.1029/2011JD015970, 2011.

**Deleted:** Schuster, Gregory L., et al. "Comparison of CALIPSO aerosol optical depth retrievals to AERONET measurements, and a climatology for the lidar ratio of dust." *Atmos. Chem. Phys.* 12.16: 7431-7452, 2012.\*

37 Thorsen, T. J., and Fu, Q.: CALIPSO-inferred aerosol direct radiative effects: bias estimates using  
38 ground-based Raman lidars, *J. Geophys. Res. Atmos.*, **120**, 12,209–12,220,  
39 doi:10.1002/2015JD024095, 2015.

40 Thorsen, T. J., R. A. Ferrare, C. A. Hostetler, M. A. Vaughan, and Q. Fu, The impact of lidar  
41 detection sensitivity on assessing aerosol direct radiative effects, *Geophys. Res. Lett.*, **44**, 9059–  
42 9067, doi:10.1002/2017GL074521, 2017.

43 Torres O., OMI/Aura Near UV Aerosol Optical Depth and Single Scattering Albedo 1-orbit L2  
44 Swath 13x24 km V003, Greenbelt, MD, USA, Goddard Earth Sciences Data and Information  
45 Services Center (GES DISC), 10.5067/Aura/OMI/DATA2004  
46 <https://doi.org/10.5067/Aura/OMI/DATA2004>, 2006.

47 Torres, O., J. Hiren, and P. K. Bhartia, Retrieval of aerosol optical depth above clouds from OMI  
48 observations: Sensitivity analysis and case studies. *J. Atmos. Sci.*, **69**, 1037–1053, 2012.

49 Toth, T. D., J. R. Campbell, J. S. Reid, J. L. Tackett, M. A. Vaughan, J. Zhang, and J. W. Marquis,  
50 2018: Minimum Aerosol Layer Detection Sensitivities and their Subsequent Impacts on Aerosol  
51 Optical Thickness Retrievals in CALIPSO Level 2 Data Products, *Atmos. Meas. Tech.*, **11**, 499–  
52 514, doi:10.5194/amt-11-499-2018.

53 Twomey, S., Influence of pollution on shortwave albedo of clouds, *J. Atmos. Sci.*, **34**(7), p1149–  
54 1152, doi:10.1175/1520-0469(1977)034<1149:TIOPOT>2.0.CO;2, 1977.

55 Várnai, T. and A. Marshak, MODIS observations of enhanced clear sky reflectance near clouds,  
56 *Geophys. Res. Lett.*, **36**, L06807, doi:10.1029/2008GL037089, 2009.

57 Vaughan, M., K. Powell, R. Kuehn, S. Young, D. Winker, C. Hostetler, W. Hunt, Z. Liu, M. McGill,  
58 and B. Getzewich, Fully automated detection of cloud and aerosol layers in the CALIPSO lidar  
59 measurements, *J. Atmos. Ocean. Tech.*, 26, 2034–2050, [oi:10.1175/2009JTECHA1228.1](https://doi.org/10.1175/2009JTECHA1228.1), 2009.

60 Vaughan, M. A., Z. Liu, M. J. McGill, Y. Hu, and M. D. Obland, On the spectral dependence of  
61 backscatter from cirrus clouds: Assessing CALIOP's 1064 nm calibration assumptions using cloud  
62 physics lidar measurements, *J. Geophys. Res.*, 115, D14206, [doi:10.1029/2009JD013086](https://doi.org/10.1029/2009JD013086), 2010.

63 Waquet F., J. Riedi, L. C. Labonnote, P. Goloub, B. Cairns, J-L. Deuzé, and D. Tanré, Aerosol  
64 Remote Sensing over Clouds Using A-Train Observations. *J. Atmos. Sci.*, **66**, 2468–2480, 2009.

65 Waquet, F., F. Peers, F. Ducos, P. Goloub, S. Platnick, J. Riedi, D. Tanré, and F. Thieuleux, Global  
66 analysis of aerosol properties above clouds, *Geophys. Res. Lett.*, 40, 5809–5814,  
67 [doi:10.1002/2013GL057482](https://doi.org/10.1002/2013GL057482), 2013a.

68 Waquet, F., et al., Retrieval of aerosol microphysical and optical properties above liquid clouds  
69 from POLDER/PARASOL polarization measurements, *Atmos. Meas. Tech.*, 6, 991–1016,  
70 [doi:10.5194/amt-6-991](https://doi.org/10.5194/amt-6-991), 2013b.

71 Watson-Parris, D., Schutgens, N., Winker, D., Burton, S. P., Ferrare, R. A., and Stier, P.: On the  
72 limits of CALIOP for constraining modelled free-tropospheric aerosol, *Geophys. Res. Lett.*, **45**,  
73 9260–9266, [doi:10.1029/2018GL078195](https://doi.org/10.1029/2018GL078195), 2018.

74 Wen, G., A. Marshak, R. F. Cahalan, L. A. Remer, and R. G. Kleidman, 3-D aerosol–cloud  
75 radiative interaction observed in collocated MODIS and ASTERg images of cumulus cloud fields, *J.*  
76 *Geophys. Res.*, 112, D13204, [doi:10.1029/2006JD008267](https://doi.org/10.1029/2006JD008267), 2007.

77 Wilcox, E. M., Direct and semi-direct radiative forcing of smoke aerosols over clouds, *Atmos.*  
78 *Chem. Phys.*, 12, 139-149, doi:10.5194/acp-12-139-2012, 2012.

79 Winker, D. M., M. A. Vaughan, A. Omar, Y. Hu, K. A. Powell, Z. Liu, W. H. Hunt, and S. A.  
80 Young, Overview of the CALIPSO mission and CALIOP data processing algorithms, *J. Atmos.*  
81 *Ocean. Tech.*, 26, 2310–2323, doi:10.1175/2009JTECHA1281.1, 2009.

82 Wittbom, C., Eriksson, A. C., Rissler, J., Carlsson, J. E., Roldin, P., Nordin, E. Z., Nilsson, P. T.,  
83 Swietlicki, E., Pagels, J. H., and Svenningsson, B., Cloud droplet activity changes of soot aerosol  
84 upon smog chamber ageing, *Atmos. Chem. Phys.*, 14, 9831-9854, doi:10.5194/acp-14-9831-2014,  
85 2014.

86 Xu, Hui, et al. "On the influence of the diurnal variations of aerosol content to estimate direct  
87 aerosol radiative forcing using MODIS data." *Atmos. Environ.*, 141: 186-196, 2016.

88 Yorks, J., D. Hlavka, M. Vaughan, M. McGill, W. Hart, S. Rodier, and R. Kuehn, Airborne  
89 Validation of Cirrus Cloud Properties Derived from CALIPSO Lidar Measurements: Spatial  
90 Properties, *J. Geophys. Res.*, **116**, D19207, doi:10.1029/2011JD015942, 2011.

91 Young, S. A., and M. A. Vaughan, The retrieval of profiles of particulate extinction from Cloud  
92 Aerosol Lidar Infrared Pathfinder Satellite Observations (CALIPSO) data: Algorithm description, *J.*  
93 *Atmos. Ocean. Tech.*, 26, 1105–1119, doi:10.1175/2008JTECHA1221.1, 2009.

94 Young, S. A., Vaughan, M. A., Garnier, A., Tackett, J. L., Lambeth, J. B., and Powell, K. A.:  
95 Extinction and Optical Depth Retrievals for CALIPSO's Version 4 Data Release, *Atmos. Meas.*  
96 *Tech. Discuss.*, doi:10.5194/amt-2018-182, accepted for publication, 2018.

97 Young, S. A., Vaughan, M. A., Garnier, A., Tackett, J. L., Lambeth, J. B., and Powell, K. A.:  
98 Extinction and Optical Depth Retrievals for CALIPSO's Version-4 Data Release: Supplementary  
99 Material, doi:10.5194/TBD, 2018.

00 Yu, H., et al. "A review of measurement-based assessments of the aerosol direct radiative effect and  
01 forcing." *Atmospheric Chemistry and Physics* 6.3: 613-666, 2006.

02 Yu, H., Y. Zhang, M. Chin, Z. Liu, A. Omar, L. A. Remer, Y. Yang, T. Yuan, and J. Zhang, An  
03 integrated analysis of aerosol above clouds from A-Train multi-sensor measurements, *Remote Sens.*  
04 *Environ.*, 121: 125–131, 2012.

05 Yu, H., and Z. Zhang, New directions: Emerging satellite observations of above-cloud aerosols and  
06 direct radiative forcing, *Atmos. Environ.*, 72, 36–40, doi:10.1016/j.atmosenv.2013.02.017, 2013.

07 Zarzycki, C. M., and T. C. Bond, How much can the vertical distribution of black carbon affect its  
08 global direct radiative forcing?, *Geophys. Res. Lett.*, 37, L20807, doi:10.1029/2010GL044555,  
09 2010.

10 Zelinka, M. D., Klein, S. A., and Hartmann, D. L., Computing and Partitioning Cloud Feedbacks  
11 Using Cloud Property Histograms. Part I: Cloud Radiative Kernels. *J. Climate*, 833 25:3715–3735,  
12 2012.

13 Zhang, J., J. S. Reid, and B. N. Holben, An analysis of potential cloud artifacts in MODIS over  
14 ocean aerosol optical thickness products, *Geophys. Res. Lett.*, 32, L15803, doi:  
15 10.1029/2005GL023254, 2005.

Formatted: references, Line spacing: Double

Formatted: Font color: Text 1

Deleted: ¶

17 Zhang Z, Platnick S. An assessment of differences between cloud effective particle radius retrievals  
18 for marine water clouds from three MODIS spectral bands. *J. Geophys. Res.*,; 116:D20215, 2011.

19 Zhang Z, Ackerman AS, Feingold G, Platnick S, Pincus R, Xue H. Effects of cloud horizontal  
20 inhomogeneity and drizzle on remote sensing of cloud droplet effective radius: case studies based  
21 on large-eddy simulations. *J. Geophys. Res.*; 117:D19208, 2012.

22 Zhang, Z., K. Meyer, S. Platnick, L. Oreopoulos, D. Lee, and H. Yu, A novel method for estimating  
23 shortwave direct radiative effect of above-cloud aerosols using CALIOP and MODIS data, *Atmos.*  
24 *Meas. Tech.*, 7(6), 1777–1789, doi:10.5194/amt-7-1777-2014, 2014.

25 Zhang, Z., Meyer, K., Yu, H., Platnick, S., Colarco, P., Liu, Z., Oreopoulos, L., Shortwave direct  
26 radiative effects of above-cloud aerosols over global oceans derived from 8 years of CALIOP and  
27 MODIS observations, *Atmos. Chem. Phys.*, 16.5: 2877-2900, 2016.

28 Zuidema, P., Redemann, J., Haywood, J., Wood, R., Piketh, S., Hipondoka, M., and Formenti, P.:  
29 Smoke and Clouds above the Southeast 25 Atlantic Upcoming Field Campaigns Probe Absorbing  
30 Aerosol's Impact on Climate, *Bulletin of the American Meteorological Society*, 97, 1131–1135,  
31 <https://doi.org/10.1175/BAMS-D-15-00082.1>, 2016,

32

Formatted: Indent: Left: 0", Space After: 0 pt

Formatted: references, Line spacing: Double

Formatted: Font color: Text 1

**Page 11: [1] Deleted**                      **Meloë Kacenenbogen**                      **3/6/19 10:02:00 AM**

**Page 34: [2] Deleted**                      **Meloë Kacenenbogen**                      **3/6/19 9:34:00 AM**

**Page 76: [3] Deleted**                      **Meloë Kacenenbogen**                      **3/6/19 10:00:00 AM**